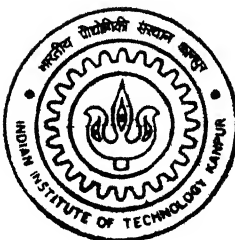


9910606

# HIGH TEMPERATURE OXIDATION AND HOT CORROSION BEHAVIOR OF CARBON-ALLOYED $\text{Fe}_3\text{Al}$ -BASED INTERMETALLIC ALLOYS

by  
DEBASHIS DAS

TH  
MME/2001/M  
D264

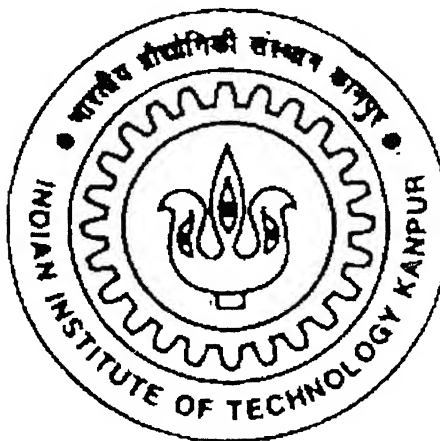


DEPARTMENT OF MATERIALS AND METALLURGICAL ENGINEERING  
INDIAN INSTITUTE OF TECHNOLOGY, KANPUR  
February, 2001

# **HIGH TEMPERATURE OXIDATION AND HOT CORROSION BEHAVIOR OF CARBON-ALLOYED Fe<sub>3</sub>Al-BASED INTERMETALLIC ALLOYS**

*by*

**DEBASHIS DAS**



**DEPARTMENT OF MATERIALS AND METALLURGICAL ENGINEERING**

**INDIAN INSTITUTE OF TECHNOLOGY, KANPUR**  
**FEBRUARY 2001**

१६/८/२००१/MME

क्रमांक

क्र.

पुस्तक

133723



A133723

# **HIGH TEMPERATURE OXIDATION AND HOT CORROSION BEHAVIOR OF CARBON-ALLOYED Fe<sub>3</sub>Al-BASED INTERMETALLIC ALLOYS**

*A Thesis Submitted  
in Partial Fulfillment of the Requirements  
for the Degree of*

**MASTER OF TECHNOLOGY**

*by*

**DEBASHIS DAS**



*to the*

**DEPARTMENT OF MATERIALS AND METALLURGICAL ENGINEERING**

**INDIAN INSTITUTE OF TECHNOLOGY, KANPUR**

**FEBRUARY 2001**

*Dedicated to my Parents: Dida, Baba, Ma and bon.*

**Without the love, blessings and encouragement of U all  
I couldn't have made this possible.**



# CERTIFICATE

This is to certify that the present work, entitled **HIGH TEMPERATURE OXIDATION AND HOT CORROSION BEHAVIOUR OF CARBON-ALLOYED Fe<sub>3</sub>Al-BASED INTERMETALLIC ALLOYS** has been carried out by Mr. Debasish Das under my supervision and to the best of my knowledge it has not been submitted elsewhere for a degree.

(Dr. R.BALASUBRAMANIAM)

Associate Professor

Department of Materials and Metallurgical Engineering

Indian Institute of Technology

Kanpur 208016, INDIA

Date: 7 Feb 2001

# Acknowledgement

I acknowledge with sincerity and deep sense of gratitude the expert guidance and continuous encouragement provided by my thesis supervisor Dr. R. Balasubramaniam throughout the course of this thesis

I wish to express my sincere appreciation of valuable help and suggestions obtained from Dr. M. N. Mungole Special thanks to him too for providing me with all possible helps regarding consumables, laboratory accessibility and technical know-how. Special thanks are also due to him for his timely help whenever it was needed without even asking a single question and at the oddest of hours.

I am also greatly thankful to Dr. A.V. Ramesh Kumar, Scientist, Defense Materials Stores Research and Development Establishment, Kanpur, for his timely help regarding FTIR analysis.

I am thankful to Mr. Umashankar Singh, Mr. R.S. Sharma, Mr. Bajpai, Mr. R.P. Singh, Mr. Sharma and Mr. Agnihotri for their help during some of my experiments

I am also thankful to my friends Shankar, Binod, Guru, Shantanu and Jain, who have helped me continuously during the entire course of my project work in one way or the other. They have all helped me a lot.

Thanks are due to all my friends from department and outside who have helped me in various capacities throughout my stay at Kanpur. Prominent amongst them are Sankha-da, Anjan-da, Neelanjan, Prabuddha, Sayan, Kushal, Arnab, Ambarish, ... The list goes on and is in no means exhaustive.

At the end I am thankful to all those who helped me directly or indirectly during my stay in IIT Kanpur.

Debashis Das.

# **Contents**

---

	<b>Page Number</b>
<b>Abstract</b>	i
<b>List of Figures</b>	iii
<b>List of Tables</b>	vi
 <b>Chapter 1 Introduction</b>	
1.1    Intermetallics	1
1.2    Iron Aluminides	2
1.3    Carbon-Alloyed Iron Aluminide	2
1.4    Objectives of the Present Study	3
1.5    Plan of Work	4
 <b>Chapter 2 Literature Review</b>	
2.1    Physical and Mechanical Properties of Aluminides	5
2.2    The Fe-Al binary system	8
2.3    Fundamentals of Oxidation of Metals and Alloys	11
2.3.1    Mechanisms of Oxidation	11
2.3.2    Rate Laws of Oxidation	13
2.4    Oxidation of Pure Metals	15
2.5    Oxidation of Alloys	16
2.5.1    Types of Oxidation	17
2.5.2    Factors Affecting Alloy Oxidation	18
2.6    Oxidation of Fe-Al systems	20
2.6.1    Scale morphology	22
2.6.2    Kinetics of High Temperature Oxidation of $\text{Fe}_3\text{Al}$	25
2.6.3    Significance of Aluminium content	25
2.7    Oxidation of Fe-Al-C systems	27

2.8	Hot Corrosion	29
-----	---------------	----

## Chapter 3 Experimental Procedure

3.1	Materials	34
3.2	Oxidation Studies	35
3.2.1	Sample Preparation	35
3.2.2	Apparatus for Isothermal Oxidation Experiments	37
3.2.3	Experimental Procedure	40
3.3	Hot Corrosion Study	41
3.4	Scale Characterization	42
3.4.1	Visual Observation of Scales	42
3.4.2	X-Ray Diffraction	43
3.4.3	Scanning Electron Microscopy	43
3.4.4	EPMA Study	44
3.4.5	Fourier Transform Infrared Spectroscopy	44
3.5	Electroless Nickel Plating	44

## Chapter 4 Results

4.1	Measurement Limitations	46
4.1.1	Temperature Measurement	46
4.1.2	Weight Gain Measurement	46
4.2	Evaluation of Rate Constant	47
4.2.1	Determination of Parabolic Rate Constant ( $k_p$ )	48
4.2.2	Determination of Rate Constant by Power Law Fitting	51
4.2.3	Variation of Parabolic Rate Constant ( $k_p$ ) with Temperature	52
4.3	Characterization of Scales	54
4.3.1	Visual Observation of the Scales	54
4.3.2	X-ray Diffraction	54
4.3.3	FTIR Spectroscopy	55
4.3.4	Scale Surface Morphology	58

4.3.4.1 Oxidation	58
4.3.4.2 Hot Corrosion	61

## **Chapter 5 Discussions**

5.1 Oxidation Behavior	65
5.1.1 Comparison of NC and 3C alloys	65
5.1.2 Transitional alumina formation	68
5.2 Hot Corrosion Behavior	70
5.2.1 Cross Sectional Analysis of 3C Alloy	71
5.2.2 Cross Sectional Analysis of NC Alloy	77
5.2.3 Mechanism of Hot Corrosion	82

## **Chapter 6 Summary and Conclusions** 87

## **References** 90

**APPENDIX A:** The raw weight gain vs. time data

**APPENDIX B:** XRD plots of all the experiments along with JCPDS files

**APPENDIX C:** FTIR plots for some of the experiments

# Abstract

The high temperature oxidation and hot corrosion behavior in pure oxygen of two Fe<sub>3</sub>Al-based iron aluminides was addressed in the study. The iron aluminides used in the present study were obtained from the Defense Metallurgical Research Laboratory, Hyderabad and they possessed the composition (in atom percent) Fe-25Al (referred as NC) and Fe-27.46Al-3.66C (referred as 3C).

The isothermal oxidation and hot corrosion behavior of both these alloys in pure oxygen have been studied at 1100K, 1225K and 1330K. Hot corrosion studies were conducted by coating the specimen surfaces with 2.5 mg/cm<sup>2</sup> of Na<sub>2</sub>SO<sub>4</sub> prior to the exposure in pure oxygen. The weight gain per unit surface area of sample ( $\Delta W/A$ ) as a function of time (t) in the oxidation and hot corrosion experiments constituted the basic experimental data. The experimental data was subjected to a variety of analysis. Parabolic rate constants ( $k_p$ ) were obtained from slopes of best-fit lines of  $(\Delta W/A)^2$  vs  $t$ . The rate of oxidation increased with increase in temperature for both the alloys. The data were also fitted according to the power law, and the analysis indicated that true parabolic behavior was not always obtained. In the oxidation of NC, the significant deviation of the entire data set from parabolic behavior at all the temperatures was attributed to the fact that two types of rate constants, one in the initial period and other in the latter period, could be determined. The different kinetics obtained during these periods has been correlated to the formation of two different types of alumina, namely  $\alpha$ - and  $\theta$ -alumina, during the process. In view of the wide acceptance and theoretical basis of the parabolic rate law,  $k_p$  was employed for further interpretation of kinetic data.

The kinetics of the oxidation of the 3C alloy was slower than that of the NC alloy. This has been related to the presence of carbides on the surface of the 3C alloy, which reduced the area exposed for oxidation. Microstructural observations indicated that the carbides were resistant to oxidation. In both the alloys, XRD characterization revealed that at the highest temperature of 1330K, only  $\alpha$ -Al<sub>2</sub>O<sub>3</sub> was present. At the intermediate

temperature of 1225K, a mixture of  $\alpha$ -Al<sub>2</sub>O<sub>3</sub> and  $\theta$ -Al<sub>2</sub>O<sub>3</sub> were identified and at the lowest temperature of 1100K, the scale consisted mostly of  $\theta$ -Al<sub>2</sub>O<sub>3</sub>.

The rate of hot corrosion was higher than the rate of oxidation, at all the temperatures, for both the alloys. There was a higher amount of scale spallation in both the alloys during hot corrosion experiments when compared to the oxidation experiments. The weight of the spalled scales were also used in collecting the experimental weight gain data. FTIR analysis of the spalled scales revealed the presence of  $\alpha$ -Al<sub>2</sub>O<sub>3</sub>,  $\alpha$ -Fe<sub>2</sub>O<sub>3</sub> and Na<sub>2</sub>SO<sub>4</sub>. XRD analysis of the scales present on the surface of the samples after hot corrosion indicated the presence of  $\alpha$ -Al<sub>2</sub>O<sub>3</sub> and  $\alpha$ -Fe<sub>2</sub>O<sub>3</sub>. At the lowest temperature used (i.e. 1100K), the salt did not melt and therefore, the rate of hot corrosion was not significant. The higher rates of attack at the elevated temperatures were related to the fluxing of Al<sub>2</sub>O<sub>3</sub>, which prevents the formation of a stable protective film on the surface of the alloy and resulted in oxidation of iron from the matrix in addition to aluminium. The propagation stage of hot corrosion has been understood by cross sectional analysis of the specimens. Sulphides were identified, by EPMA analysis and cross-sectional SEM, at the metal-scale interface and along the grain boundaries in the substrate material. The penetration of sulphur to the scale-metal interface, which aids the formation of sulphides. The relatively low oxygen partial pressure at this location is a contributory factor. The oxidation of sulphides results in higher oxidation kinetics, with the sulphur released penetrating the surface further to cause further sulphidation at the scale-metal interface as well as along the grain boundaries. The 3C alloy exhibited lower hot corrosion kinetics and this has been attributed to the presence of carbide particles along the grain boundaries (and also within the bulk of the material). These carbides lower the penetration rate of sulphides into the material.

# List of Figures

---

	Page Number
2.1 Calculated and experimental activity of aluminium in solid Ni-Al and Fe-Al alloys at 1000°C	8
2.2 The Fe-Al Binary Phase Diagram	9
2.3 The DO <sub>3</sub> and B2 ordered crystal structure of Iron-aluminides	10
2.4 Interfacial reaction and transport processes through oxide scale during high temperature oxidation	12
2.5 Schematic diagram showing possible features (exaggerated) that would be revealed if weight gain were recorded continuously.	15
2.6 Schematic of the oxidation of a noble metal, A, containing a reactive metal, B [14].	17
2.7 Development of $\theta$ -Al <sub>2</sub> O <sub>3</sub> whisker morphology on NiAl+Zr after 100hr oxidation [23]	23
2.8 Fully developed ridge structure in mature $\alpha$ -Al <sub>2</sub> O <sub>3</sub> scales formed on NiAl + Zr after 100hr oxidation [23]	23
2.9 SEM morphology on FeAl-Hf alloy [34] at 1173K and 1273K	24
2.10 Cells and ridge networks and radial transformation cracks on FeAl-Hf for oxidation at 1373K	24
2.11 Effect of aluminium content on isothermal oxidation of Fe-Al binary alloys exposed to air at 900°C	26
2.12 Weight changes of iron-aluminium alloys under cyclic oxidation conditions.	27
2.13 Effect of carbon concentration on the oxidation of Fe-5.5%Al-C alloys at 800°C in oxygen at 700 Torr.	28
2.14 Mass change versus time for IN-738 coated with 1mg cm <sup>-2</sup> Na <sub>2</sub> SO <sub>4</sub> in 1atm O <sub>2</sub> [29]	30
2.15 Solubility of NiO in fused Na <sub>2</sub> SO <sub>4</sub> at 1200K	32
3.1 Optical microstructure and SEM micrograph of the as-received 3C sample	36

3.2	Schematic Diagram of the experimental set-up for the Oxidation and Hot Corrosion Process	38
3.3	Experimental set-up employed for the Oxidation and Hot Corrosion Process	39
4.1	Comparison of $(\Delta W/A)^2$ vs. time plots for oxidation of 3C in pure oxygen with Babu [25]	47
4.2	$(\Delta W/A)^2$ vs. time plots for oxidation of NC in pure oxygen	49
4.3	$(\Delta W/A)^2$ vs. time plots for oxidation of 3C in pure oxygen	49
4.4	$(\Delta W/A)^2$ vs. time plots for hot corrosion of NC in pure oxygen	50
4.5	$(\Delta W/A)^2$ vs. time plots for hot corrosion of 3C in pure oxygen	50
4.6	Variation of $k_p$ with temperature for the oxidation and hot corrosion experiments for the NC and 3C alloys	53
4.7	SEM morphologies of the oxide scales of the alloy NC oxidized for 65hrs at different temperatures	59
4.8	SEM morphologies of the oxide scales of the alloy 3C oxidized for 65hrs at different temperatures	60
4.9	SEM morphologies of the alloy NC hot corroded for 65hrs at different temperatures	62
4.10	SEM morphologies of the alloy 3C hot corroded for 65hrs at different temperatures	63
4.11	SEM morphologies of the alloy NC hot corroded for 65hrs at 1330K with different morphologies	64
5.1	SEM morphologies of the cross-sectional features of the alloy 3C oxidized at 1330K for 65hrs	67
5.2	The literature data's for the two types of $\text{Al}_2\text{O}_3$ ( $\alpha$ and $\theta$ ) compared with the oxidation rate values for the alloy NC	69
5.3	SEM morphologies of the cross-sectional features of the alloy 3C hot corroded at 1330K for 65hrs.	72
5.4	SEM morphologies of the cross-sectional features of the alloy 3C hot corroded at 1330K for 65hrs.	73

5.5	EPMA analysis of the corrosion product from the pit corresponding to the SEM micrograph Figure 5.4(b) of the alloy 3C hot corroded at 1330K for 65hrs	74
5.6	EPMA analysis of the corrosion product from the pit corresponding to the SEM micrograph Figure 5.4(c) of the alloy 3C hot corroded at 1330K for 65hrs.	75
5.7	EPMA analysis of the external cross-sectional scale of the alloy 3C hot corroded at 1330K for 65hrs.	76
5.8	SEM morphologies of the cross-sectional features of the alloy NC hot corroded at 1330K for 65hrs.	78
5.9	EPMA analysis of the corrosion product zone from the location marked A, corresponding to the SEM micrograph Figure 5.7(b) of the alloy NC hot corroded at 1330K for 65hrs.	79
5.10	SEM morphologies of the cross-sectional features of the alloy NC hot corroded at 1330K for 65hrs.	80
5.11	EPMA analysis of the corrosion product from the pit marked A, corresponding to the SEM micrograph Figure 5.9(b) of the alloy NC hot corroded at 1330K for 65hrs.	81
5.12	Phase stability diagram of $\text{Al}_2\text{O}_3$ at 900°C in the stability region of $\text{Na}_2\text{SO}_4$ (l).	83
5.13	Measured oxide solubilities in fused $\text{Na}_2\text{SO}_4$ at 927°C and 1atm $\text{O}_2$ [40].	83

## List of Tables

---

	Page Number
2.1 Comparison of Properties of Some Important Aluminide Alloys [2]	6
2.2 Equilibrium partial pressure of some oxides [7]	7
2.3 Typical oxygen partial pressures of some high temperature processes [7]	7
2.4 Typical room temperature properties of iron aluminides	10
4.1 Summary of rate constants processed from the data of the thermogravimetric experiments	48
4.2 The parabolic rate constants for the first and second stages of oxidation of alloy NC in oxygen at the three temperatures	51
4.3 Effective activation energy ( $Q_{\text{eff}}$ ), in kJ/mol estimated from the LOG $k_p$ versus $1/T$ plots	52
4.4 Summary of nature of scales observed on NC and 3C after oxidation (OX) and hot corrosion (HC)	57
4.5 Scale characterization by FTIR study	57
5.1 The free-energy ( $\Delta G$ ) values for the probable corrosion products [47]	82

# **Chapter 1**

## **INTRODUCTION**

The topic of present study is high temperature degradation behavior of two  $\text{Fe}_3\text{Al}$ -based intermetallic alloys, one containing carbon and the other, a binary alloy without any carbon. This chapter introduces the subject of intermetallics, with emphasis on iron aluminides. The technical importance of these materials has motivated investigation into several aspects concerning these materials and towards better understanding of its properties. The chapter concludes with the objective of the present study and the plan of work.

### **1.1 Intermetallics**

Ordered intermetallics constitute a unique class of advanced materials that form long range-ordered crystal structure below a critical temperature termed as the critical ordering temperature ( $T_c$ ) [1]. These usually exist in relatively narrow or fixed compositional ranges around simple stoichiometric ratios (similar to inorganic compounds). The need to develop materials possessing high specific strength for structural applications at elevated temperatures has motivated research in the area of ordered intermetallics.

Intermetallic aluminides possess many interesting features that project them as candidate material for high temperature structural applications [2]. They contain enough aluminium to form, in oxidizing environments, a thin film of aluminium oxide that are often compact and protective. They are characterized by low densities, relatively high melting points and good mechanical properties at elevated temperatures. The aluminides that have attracted attention as potential candidates for high temperature applications include titanium, nickel and iron aluminides, and hence have undergone extensive development in the recent past, primarily for high temperature applications. Research on these materials are being conducted extensively for effecting modifications on the

existing systems (either by alloying or by the modifications in the processing steps) in order to optimize their properties.

## 1.2 Iron Aluminides

Important iron aluminides are ordered intermetallics centered around the composition  $\text{Fe}_3\text{Al}$  and  $\text{FeAl}$ . These iron aluminides possess attractive properties for application at elevated temperatures and severe environments over conventional structural materials like stainless steel and nickel-based super alloys. Specific advantages include, excellent sulphidation resistance, very good oxidation resistance, lower density ( $5400\text{-}6700 \text{ kg/m}^3$ ) which is 30% of that of the commercially available high temperature materials, good wear resistance, good cavitation erosion resistance, potentially lower cost and reduced consumption of strategic element such as chromium [3]. One of the essential factors in increasing the maximum use temperature is enhanced oxidation resistance. Once the desired crystal structure and subsequent mechanical properties have been achieved, then focus should be on high temperature oxidation resistance. Therefore, understanding the thermodynamics and kinetics of oxidation, in these materials, is of utmost importance.

## 1.3 Carbon-Alloyed Iron Aluminide

Though the iron aluminides exhibit poor room temperature ductility and low fracture toughness, significant improvement in these respects can be achieved by alloying addition and process control. Most of the literature is on iron aluminide compositions with very low (0.01 wt%) carbon contents because carbon is known to embrittle these alloys causing significant reduction in ductility. However, no reason has been ascribed to this loss in ductility. Recently Baligidad *et al* have reported that addition of carbon in the range of 0.14 to 0.50 wt. % significantly increases the room temperature strength of Fe-16 wt% (28 at%) Al alloys [4]. These alloys also exhibited good room temperature ductility, due to the entrapment of hydrogen by  $\text{Fe}_3\text{AlC}$  particles, which was proposed to lower hydrogen diffusivity in these alloys and reduce the susceptibility to environmental embrittlement [4]. The increase in room temperature yield strength was attributed to solid

solution strengthening by the interstitial carbon, as well as precipitation hardening due to the presence of  $\text{Fe}_3\text{AlC}$  precipitates [5].

These carbon alloyed iron aluminides were produced in DMRL, Hyderabad by a combination of air induction melting and electroslag remelting (ESR). The melting practice have been described in detail in next chapter. The ESR ingots were held at  $1000^{\circ}\text{C}$  for 1 hour and hot forged in one tonne press with die platens at room temperature. The ESR ingots exhibited columnar grains having an average grain diameter of  $1750 \mu\text{m}$  before forging. After forging, with reduction ratio of 70%, they exhibited recrystallized grains [4].

## 1.4 Objectives of the Present Study

The present study is specifically concerned with kinetics of high temperature oxidation and hot corrosion in pure oxygen of a binary iron aluminide and a carbon-alloyed iron aluminide. As the carbon-alloyed iron aluminide contains carbide precipitates, their effect on oxidation and hot corrosion are to be investigated. As far as high temperature isothermal oxidation and hot corrosion are concerned, the following aspects are to be investigated :

1. Comparison of kinetics of high temperature oxidation and hot corrosion of  $\text{Fe}_3\text{Al}$  and carbon-alloyed iron aluminide exposed to pure oxygen environment at three different high temperatures.
2. Assessment of reliability of processing of empirical data on the basis of parabolic law.
3. Understanding the role of alloying (carbon addition) on the oxidation and hot corrosion behavior of iron aluminides.
4. Characterize the type and nature of scale formed in order to understand the possible mechanism(s) involved.
5. Correlation of the experimentally observed kinetics with the nature of scales.

## **1.5 Plan of Work**

The work has been planned to proceed according to the following sequence

- (a) Procurement of Fe<sub>3</sub>Al and carbon-alloyed iron aluminide (Fe-27.46Al-3.66C) from DMRL, Hyderabad
- (b) Preparation of samples for high temperature oxidation and hot corrosion studies from these stock materials
- (c) Characterization of the as-received materials by microscopy and X-ray diffraction (XRD)
- (d) Thermogravimetric studies to measure oxidation rates.
- (e) Characterization of the scales from both oxidation and hot corrosion experiments by:
  - Visual observation of the scales.
  - X-ray diffraction studies.
  - Topological observations on SEM.
  - Cross-sectional analysis of structure and compositions using electron probe microanalyzer (EPMA) after electroless Ni coating of the oxidized surfaces.
  - Fourier transform infrared spectroscopy (FTIR) study of scales.
- (f) Corrosion rate determination from the weight gain data.
- (f) Analysis and interpretation of results.

In summary, the present investigation aims to understand the role of carbon on the oxidation behavior of the binary intermetallic and to assess the hot corrosion behavior of both the intermetallic alloys. Chapter 2 deals with the review of the literature. Experimental procedures are discussed in Chapter 3. Chapter 4 presents the results, while these results are discussed in Chapter 5. The conclusions and suggestions for further work are listed in Chapter 6.

# **Chapter 2**

## **LITERATURE REVIEW**

This chapter briefly addresses the various types of important intermetallics, followed by a description of general properties of iron aluminides. The later part concentrates on the literature review of the oxidation behaviour of iron aluminides, focussing attention on Fe<sub>3</sub>Al-based intermetallic alloys. The fundamentals of oxidation and hot corrosion have also been briefly reviewed. Emphasis has been stressed on the kinetics of oxidation with special reference to oxidation of iron aluminides. The kinetics of different kinds of alumina formation has been outlined. The available literature on the oxidation of iron aluminides has been reviewed, stressing the co-relation between oxidation kinetics and the characteristics of the oxide scales.

### **2.1 Physical and Mechanical Properties of Aluminides**

There are about 300 intermetallic compounds with high melting temperatures. Intermetallic compounds (like aluminides and silicides) fall between metal and ceramics when their nature is judged from the viewpoint of bonding character. The majority of aluminides, formed by two elements A and B, can be classified into three different stoichiometric combinations with compositions around A<sub>3</sub>B, A<sub>2</sub>B and AB. Within each stoichiometric group, the compounds may have different crystal structure.

At present, aluminides based on nickel, iron and titanium have either been developed to a stage or close to a stage ready for commercial application. Most of them contain sufficient amount of aluminium to form thin film of alumina (Al<sub>2</sub>O<sub>3</sub>) in oxidizing environments that are often compact and protective. These materials have low densities, relatively high melting points, and good high temperature mechanical properties such as strength retention, creep/stress rupture and fatigue resistance. By far, the greatest impediment in exploitation of these materials is their relative brittleness at room temperature. However, some remedial measures have been proposed, which offer the

possibility of engineering applications. Table 2.1 lists the properties of some important engineering aluminides [2].

**Table 2.1: Comparision of Properties of Some Important Aluminide Alloys [2]**

Alloys	Melting Point (°C)	Density (g/cm <sup>3</sup> )	Yield Strength (MPa)	Room Temp. Ductility	Creep Limit (°C)
Ti <sub>3</sub> Al	1600	4.20	700-990	2-10	760
TiAl	1460	3.91	400-650	1-4	1000
Ni <sub>3</sub> Al	1390	7.50	250-500	2-50	760
NiAl	1640	5.86	250-475	2	1200
Fe <sub>3</sub> Al	1540	6.72	385-392	2-12	700
FeAl	1250	5.56	360-380	2-17	827

Aluminides based on the intermetallic phases Ni<sub>3</sub>Al and Fe<sub>3</sub>Al are considered both as structural materials and as coatings for high temperature applications. Their excellent corrosion resistance is due to their forming a dense, protective alumina scale. Alumina, especially  $\alpha$ -Al<sub>2</sub>O<sub>3</sub>, exhibits low oxidation kinetics even at temperatures above 1000°C [6]. Unlike chromia, which is formed on conventional stainless steels and nickel base alloys, alumina does not evaporate above 1000°C and it is even stable in oxygen deficient atmospheres.

Table 2.2 shows the equilibrium oxygen partial pressure of several metal oxides, i.e. the minimum oxygen partial pressure required for oxide formation. A comparison with Table 2.3, in which typical oxygen partial pressures of industrial processes are listed, clearly demonstrates that stable oxide scales in coal gasification processes and petrochemical plants can only be expected on alumina formers. Chromia becomes unstable at the low oxygen partial pressures encountered in such processes.

**Table 2.2: Equilibrium partial pressure of several oxides [7]**

Oxide	P <sub>O<sub>2</sub></sub> /P° <sub>O<sub>2</sub></sub>
2/3 Al <sub>2</sub> O <sub>3</sub>	1.6 X 10 <sup>-34</sup>
2/3 Cr <sub>2</sub> O <sub>3</sub>	3.4 X 10 <sup>-22</sup>
2 NiO	9.0 X 10 <sup>-11</sup>
1/2Fe <sub>3</sub> O <sub>4</sub>	4.9 X 10 <sup>-15</sup>
2/3 Fe <sub>2</sub> O <sub>3</sub>	9.5 X 10 <sup>-14</sup>

**Table 2.3: Typical oxygen partial pressures of some high temperature processes [7]**

Process	Typical oxygen partial pressure in bar
Petrochemical plants	10 <sup>-25</sup> -10 <sup>-30</sup>
Gas cooled reactors	10 <sup>-25</sup> -10 <sup>-30</sup>
Fluidised bed combustion	10 <sup>0</sup> -10 <sup>-5</sup>
Coal gasification	~10 <sup>-25</sup>

There should be no significant difference between alumina scales formed on nickel aluminide and those formed on iron aluminide. Compared to Ni<sub>3</sub>Al, however, Fe<sub>3</sub>Al has some major advantages:

- (1) The metal (Al) activity of iron aluminides is about two orders of magnitude higher than that of nickel aluminide, as can be seen from Figure 2.1. The higher metal activity results in a higher thermodynamic stability of iron-aluminides.
- (2) The diffusion coefficient of aluminium in a ferritic iron-aluminium matrix is some orders of magnitude higher than in austenitic Ni<sub>3</sub>Al. Because of the low diffusion coefficient, diffusion in nickel aluminides is slow and aluminium depletion beneath the alumina scale and formation of non-protective nickel oxides has been observed in Ni<sub>3</sub>Al [8].
- (3) It is well known that nickel base alloys are susceptible to the formation of liquid Ni-Ni<sub>3</sub>S<sub>2</sub> eutectics (melting point: 635°C). If once formed, the liquid phases can cause rapid wastage of the material. Fe-S compounds, on the other hand, become liquid not below 985°C [6].

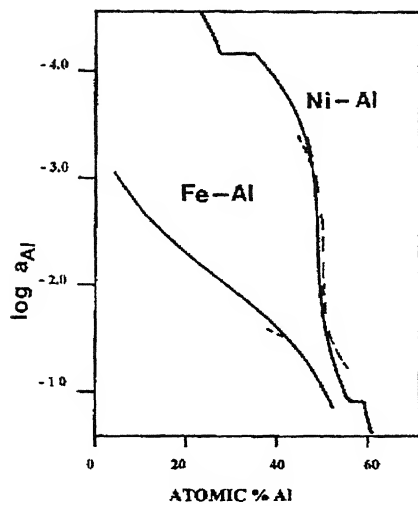


Figure 2.1 Calculated and experimental activity of aluminium in solid Ni-Al and Fe-Al alloys at 1000°C. The dashed lines indicate measured values [7].

Due to their excellent sulphidation resistance, iron aluminides are considered for application in coal gasification and other processes, where high concentrations of sulphur in combination with low oxygen partial pressures are encountered. It is generally found that the corrosion resistance increases with increasing aluminium concentrations. High aluminium concentrations, however, decrease the ductility of iron aluminium alloys and cause severe problems during casting, cold working and welding. This implies that it is of interest to keep the aluminium concentration as low as possible for the sake of ease of fabrication [9].

## 2.2 The Fe-Al binary system

Al is only slightly soluble in face-centered cubic Fe and dissolution of about 1.5% Al is sufficient to suppress the formation of the  $\gamma$  phase [10]. Al, however, is highly soluble in body-centered cubic Fe up to a solubility limit of approximately 34%. The solidus temperature of this solution ranges from 1538°C for pure Fe to approximately 1200°C at 34% Al. Within this phase field, several ordering reactions may take place; these arise from the large difference in size between the Fe and Al atoms and may lead to

the formation of intermetallic  $\text{Fe}_3\text{Al}$  or  $\text{FeAl}$ . These intermetallics may be magnetic or non-magnetic. They have ordered structures and their formation is affected by the rate of cooling. Rapid cooling or quenching is more likely to retain the random atomic distribution.

Ordered iron aluminides exist in relatively narrow compositional ranges around simple stoichiometric ratios. The phase diagram of Fe-Al system is shown in Figure 2.2.

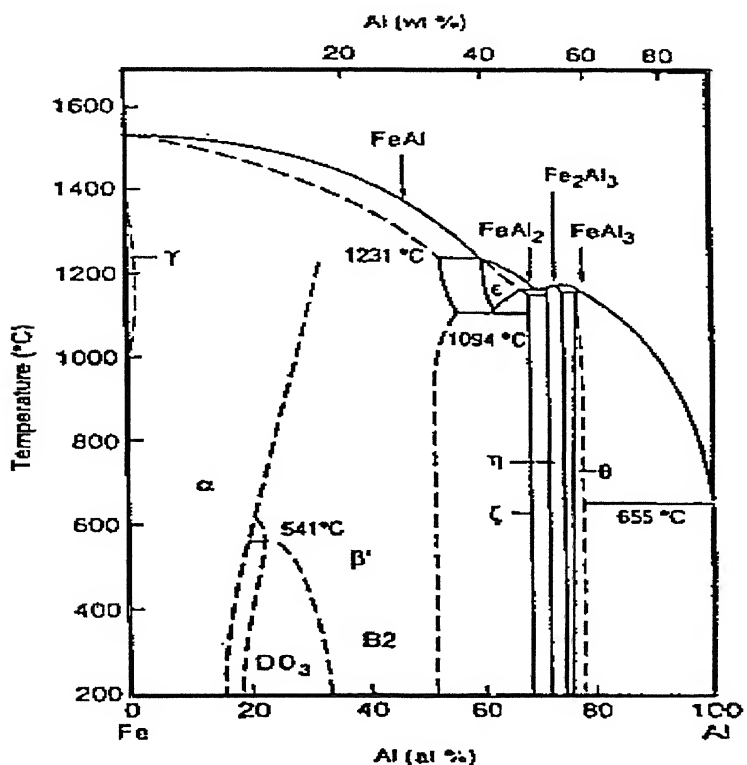


Figure 2.2 The Fe-Al Binary Phase Diagram

Iron aluminides based on  $\text{Fe}_3\text{Al}$  and  $\text{FeAl}$  can exist in two crystal allotropic modifications. These structures ( $\text{DO}_3$  and  $\text{B}2$ ) [11] are both ordered BCC structures and these are presented in Figure 2.3.  $\text{Fe}_3\text{Al}$  can exist as both  $\text{B}2$  and  $\text{DO}_3$  ordered structure (depending upon the temperature) while  $\text{FeAl}$  can exist only in the  $\text{B}2$  ordered form.

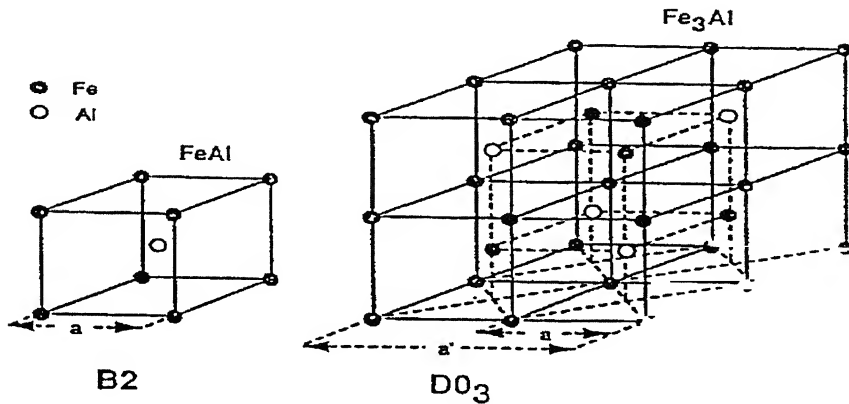


Figure 2.3 The  $\text{DO}_3$  and  $\text{B}2$  ordered crystal structure of Iron-aluminides

Table 2.4 presents some typical room temperature properties and critical ordering temperatures for different allotropic modifications of iron aluminides [3].

**Table 2.4: Typical room temperature properties of iron aluminides [3]**

Alloy	Crystal structure	Ordering temp.	Melting point	Density (gm/cc)	Y.S (MPa)	Elongation (%)
$\text{Fe}_3\text{Al}$	$\text{DO}_3$	540°C	1540°C	6.72	300	3.7
$\text{Fe}_3\text{Al}$	$\text{B}2$	760 °C	1540 °C	6.72	380	4.1
$\text{FeAl}$	$\text{B}2$	1250 °C	1250 °C	5.56	360	2.2

## **2.3 Fundamentals of Oxidation of Metals and Alloys**

In general, metals and alloys form stable oxides under exposure to air or oxygen at elevated temperatures. For some metals and alloys, the reactivity with atmospheric oxygen (i.e. oxidation) is a primary obstacle to their engineering applications, especially at high temperatures. Some important fundamental aspects of high temperature oxidation of metals and alloys are presented in this section [6, 12].

When a clean metal is exposed to reacting gases, the initial process is adsorption of gas on the metal surface [13]. This is followed by nucleation, and growth of nuclei of the reaction products. They grow laterally to cover the metal surface as a film. Thus, the metal and the gas are separated by reaction products. In order for the reaction to proceed further, one or both reactants must penetrate the scale. Therefore, the mechanism by which the reactants may penetrate the oxide layers is considered to be an important part of the mechanism of high temperature oxidation. Since all metal oxides are ionic in nature, transport of neutral metal or non-metal atoms through the oxide scale has been ruled out.

### **2.3.1 Mechanisms of Oxidation**

Various mechanisms are available to explain the migration of ions through ionic solids, which may be divided into stoichiometric crystals or non-stoichiometric crystals. Ionic mobility in stoichiometric crystals is explained by the existence of ionic vacancies and interstitials, and migration of electrons is neglected. Fig.2.4 is a simplified representation of mechanism of high temperature oxidation. The kinetic steps are:

- (a) Transport of  $O_2$  in gas to the oxide/gas interface.
- (b) Reaction at oxide/gas interface.
- (c) Transport of ions and electrons through the oxide scale
- (d) Reaction at the metal/oxide interface.
- (e) Diffusion of metal (in case of alloy oxidation) to metal/oxide interface.
- (f) Diffusion of oxygen into metal.

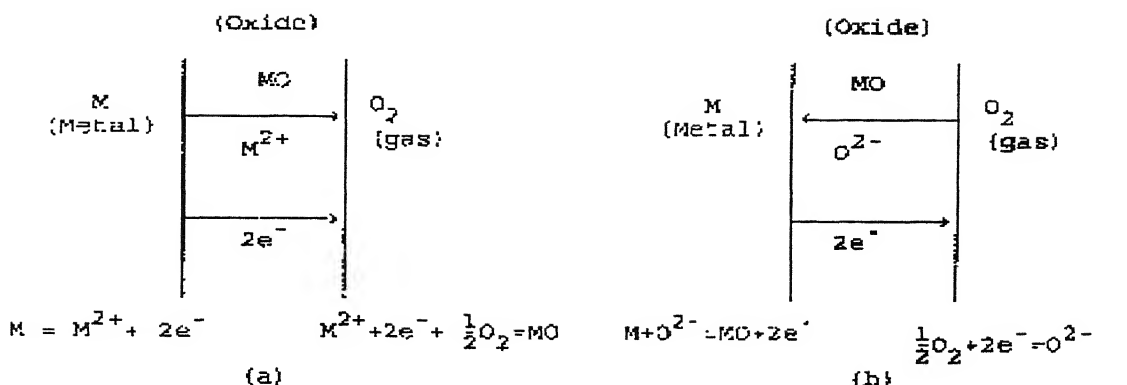


Figure 2.4 Interfacial reaction and transport processes through oxide scale during high temperature oxidation, (a) cation mobile, (b) anion mobile.

The above is valid for non-porous oxide scales. If the oxide is porous, then oxygen molecules can diffuse through pores. The cation migration leads to scale formation at the scale/gas interface whereas the anion migration results in the scale formation at the metal/scale interface. Mobilities of ions and electrons are primarily possible due to the presence of point defects in the oxide scale, either vacancies or interstitials. Cations can move only through cation vacancies and cation interstitials. Anions can move only through anion vacancies or anion interstitials. Larger is concentration of a particular type of defect; greater is the mobility of the corresponding ion through the scale. Hence the type of defect and nature of defect affect the oxidation process a lot. It can generally be said that a defective oxide results in increased mobilities of the ionic species in the oxide scale and consequently increased rate of oxidation. Defects can generally be classified into ionic and electronic defects. Ionic defects are Frenkel and Schottky defects. Deviations from stoichiometry and doping effects lead to creation of electronic defects (p-type or n-type, respectively depending on whether the electron or hole is the majority charge carrier.) As the mobilities of electrons and holes several times greater than that of the ions, presence of electronic defects leads to increased rate of oxidation. In general, a

defective oxide results in increased mobilities of the ionic species in the oxide scale and consequently increased rate of oxidation.

Simultaneous migration of electrons is possible since the oxides formed during oxidation have non-stoichiometry to different extents. Non-stoichiometric oxides are semiconductors, and exhibit either negative (i.e. n-type) or positive (i.e. p-type) conduction. In n-type oxides, the conduction electrons are mobile. It is a consequence of either excess of metal or deficit of non-metal in the lattice. Some of the n-type oxides are  $ZnO$ ,  $TiO_2$ ,  $Nb_2O_5$ , etc. In p-type oxides charge transfer is by electron hole conduction. It arises from either a deficit of metal or an excess of non-metal.  $NiO$ ,  $Al_2O_3$ ,  $Cr_2O_3$ ,  $FeO$  are some of the oxides which show p-type behaviour. Deviation of stoichiometry in the case of  $Cr_2O_3$  and  $Al_2O_3$  is very small.

### 2.3.2 Rate Laws of Oxidation

Assuming that the oxide scale is of uniform density, a plot of weight gain per unit surface area vs time will have the same nature as that of oxide thickness vs time plot. Furthermore, weight gain is easier to measure than the film thickness, especially if thickness is very small. The following rate laws in terms of weight gain per unit surface area ( $\Delta W/A$ ) and time of oxidation ( $t$ ) have been experimentally observed.

1. **Linear rate law :** Here rate of oxidation is independent of time. This is expected when kinetic step a and/or steps c and d are rate controlling. The linear relationship is

$$(\Delta W/A) = k_l t \quad (2.1)$$

where,  $k_l$  is linear rate constant. This law has been found to be obeyed when the scale is very thin such as at initial stages of oxidation.

2. **Parabolic rate law :** Here the rate of oxidation is inversely proportional to the square root of time. This is expected to be valid when the diffusion of the ions through the oxide layer is rate controlling. However such expectation is valid under idealized condition when the scale is uniform throughout in composition. Rate control by diffusion through oxide is likely when the scale has some thickness. The parabolic relationship is:

$$(\Delta W/A)^2 = k_p t \quad (2.2)$$

The straight line may not intersect the zero point of the co-ordinate axes since the parabolic law is not generally valid at the initial stage. Then the more general form of parabolic equation may be employed, viz.

$$(\Delta W/A)^2 = k_p t + C \quad (2.3)$$

where,  $k_p$  is parabolic rate constant and  $C$  is also a constant.

Parabolic rate law has been found to be obeyed approximately in many investigations of high temperature oxidation of metals and alloys and hence it has become a practice to interpret observed rates on the above basis. This parabolic rate constant is a significant factor, which has been related to various physico-chemical parameters like diffusivity of the oxygen ion in the oxide lattice, mobilities of cations and electrons etc.

The parabolic rate law has been arrived at based on the following assumptions:

- a. oxide is compact and perfectly adherent to the substrate
- b. migration of ions or electrons through the oxide layer is the rate-controlling step
- c. thermodynamic equilibrium exists at both the metal/oxide and oxide/gas interfaces
- d. local thermodynamic equilibrium is established throughout the scale
- e. scale is thick with small deviation from stoichiometry
- f. dissolution of oxygen in the metal may be neglected

Other rate laws such as logarithmic, inverse logarithmic rate laws are valid for very thin films at low temperatures. Under certain conditions, some systems might even show composite kinetics like paralinear behavior. These can be explained based on the nature of oxide film present on the surface.

An experimental thermogravimetric plot may sometimes indicate a sudden enhanced rate. This is an indication of cracking of the scale due to growth stresses. Spalling of the scale leads to sudden loss of weight consequently enhancing the rate. These can be detected if weight gain is continuously recorded as a function of time. These are schematically illustrated in Figure 2.5

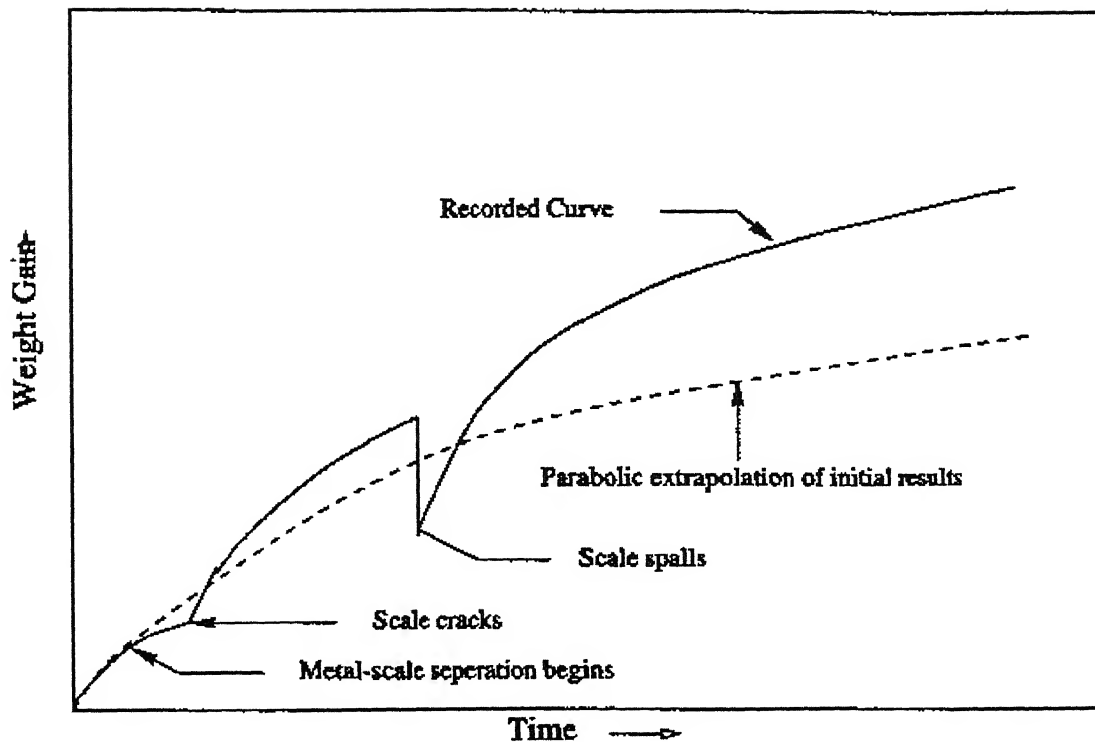


Fig.2.5 Schematic diagram showing possible features (exaggerated) that would be revealed if weight gain is recorded continuously.

## 2.4 Oxidation of Pure Metals

It is difficult to illustrate completely any single mode of rate control during oxidation process. For example, when a metal is exposed at high temperature to an oxidizing environment, the initial rate is expected to be very large since the oxide layer is very thin. Strictly speaking the parabolic law, if extrapolated to zero scale thickness predicts an infinite initial rate. This is not possible; so the initial stage of oxidation must be controlled by some process other than ionic transport, such as surface reaction step. Observation of the initial period is very difficult, since some oxide scale forms even during heating the sample to that temperature.

Once the oxidation of metal is controlled by ionic diffusion, the parabolic law has been found to be obeyed for a period whose duration depends on factors such as sample geometry and nature of scale. In metal oxidation there are systems (e.g. Ni) where scale forms as single layer ( $\text{NiO}$ ). Multiple scale layers also form in some systems e.g. Fe, Co, etc. Some metals form volatile oxides as well, e.g. oxidation of Cr results in  $\text{Cr}_2\text{O}_3$  formation, which under certain conditions evaporates and leads to scale thinning.

Some metals exhibit significant oxygen solubilities. For example, Ti forms a number of stable oxides, and has high oxygen solubilities. Oxidation of Ti in the temperature range of 873K to 1273K was found to obey parabolic law but the rate was a combination of two processes, oxide scale growth and oxygen dissolution into the metal. Linear oxidation is observed in some systems (e.g. Nb) after some time due to scale due to scale cracking under stress. This has been termed as “breakaway” linear oxidation.

## 2.5 Oxidation of Alloys

Alloy oxidation is more complex than oxidation of pure metal as a result of some, or all of the following:

- 1) The metals in the alloys will have different affinities for oxygen
- 2) There may be a degree of solid solubility between the oxides
- 3) Different mobilities of various metal ions in the oxide phases
- 4) Different diffusivities of metals in the alloy
- 5) Precipitation of subsurface oxides of one or more alloying elements (internal oxidation) may occur due to dissolution of oxygen into the alloy.

Alloy oxidation has been classified into two groups:

- (a) noble parent with base alloying elements and,
- (b) base parent metal with base alloying elements.

The efforts for development of oxidation resistance in alloy are based on the idea of addition of an element, which will get selectively oxidized and provide a protective scale. The requirement is that the oxide of alloying element be more stable than the oxide of the base metal. Another requirement is that the concentration of the alloying element for oxidation resistance must be sufficient for the formation of its oxide as an external scale rather than as an internal precipitate. Figure 2.6 illustrates schematically the two

possibilities for the simple case where the oxygen partial pressure is too low to oxidize the parent metal [14].

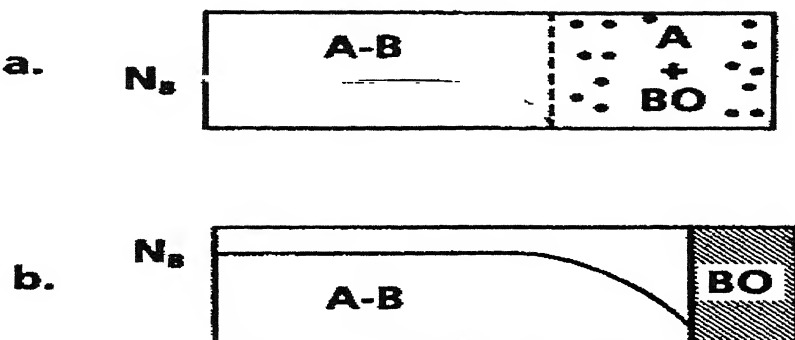


Figure 2.6 Schematic of the oxidation of a noble metal, A, containing a reactive metal, B.

(a) Dilute alloy showing internal oxidation of B, (b) Concentrated alloy forming an external layer of BO [14].

### 2.5.1 Types of Oxidation

The process of oxidation can be briefly classified into the following types [15]:

- (a) **Protective Oxidation** – formation of a continuous alumina or silica surface film with no internal oxidation and minimal penetration of oxygen into the substrate. The overall oxidation rate is determined by transport through this film.
- (b) **Accelerated Oxidation** – the alumina or silica is not continuous and significant amounts of the other component(s) of the intermetallic are present in the surface film. The overall oxidation rate is substantially faster than that for the growth of alumina or silica.
- (c) **Internal Oxidation** – precipitation of oxides rich in Al or Si within the intermetallic.
- (d) **Intergranular Oxidation** – special case of internal oxidation in which oxides form along grain boundaries within the intermetallic.

(e) **Pesting** – disintegration (fracture) of the intermetallic into smaller particles at the oxidation temperature.

The occurrence of protective oxidation precludes the other phenomena from occurring as long as the oxide is not damaged. However, in the absence of protective oxidation, any or all of the other phenomenon may occur together. In the case of NiAl this degradation occurs in the temperature range 700°C to 1000°C and can take the form of intergranular oxidation at reduced oxygen partial pressures in the range  $10^{-11}$  to  $10^{-7}$  atm. and internal oxidation in the oxygen pressure range  $10^{-2}$  to  $10^{-22}$  atm. A particularly complex form of degradation occurs when exposures are carried out in evacuated silica ampoules containing buffer mixtures, such as Cu/Cu<sub>2</sub>O. This attack is termed pocks. The oxidation morphology consists of an outer zone of silicides and silicates (Si is the result of SiO vapor transport from the capsule walls) over an internal oxidation zone of alumina in virtually pure Ni. A substantial Al-depleted zone, which has transformed to Ni<sub>3</sub>Al, is observed beneath the internal oxidation zone. The detailed mechanism for this process is not completely understood but is known to require conditions that prevent the formation of a protective alumina layer (temperatures which favor formation of transition aluminas and possibly contaminants such as S) and a process, which rapidly consumes Al (the internal oxidation). Pocks do not form when the buffer mixture is thoroughly dried prior to specimen exposure, when the NiAl is alloyed with Cr, or for aluminide coatings on Ni-base superalloys. These observations are possibly all the result of conditions which favor the rapid establishment of  $\alpha$ -alumina rather than transition aluminas. Similar studies have, apparently, not been performed for FeAl.

## 2.5.2 Factors Affecting Alloy Oxidation

In oxidation at high temperatures, stress generation in the oxide scale plays a very important role. The sources of stresses are:

- (a) *thermal stresses* due to differential thermal expansion/contraction between the scale and substrate as a result of thermal cycling.
- (b) *growth stresses* as a consequence of the following:
  - (i) volume differences between the oxide and the metal from which it is formed
  - (ii) formation of oxide at the scale-oxide interface

(iii) compositional change within the oxide or the alloy

(iv) epitaxial stresses

(v) stresses due to geometry and preparation of the specimen

Specific volume difference between the oxide and the metal is the principal source of growth stresses. The sign of the stress in the oxide is indicated by a simple parameter known as Pilling-Bedworth ratio (PBR). However, this mechanism would only seem to be feasible if the oxide forms at the scale-metal interface.

$$\text{PBR} = \frac{V(\text{per metal ion in oxide})}{V(\text{per metal atom in metal})}$$

For  $\text{PBR} < 1$ , oxide volume is insufficient resulting in porous and unprotective scale. For  $\text{PBR} > 2$ , large compressive stresses are likely, leading to buckling and flaking off scale. Oxide tends to be protective when PBR is equal to unity or slightly greater than unity.

The stresses developed during oxidation may be accommodated by a number of mechanisms. Some of these are:

(1) cracking of scale

(2) oxide spallation

(3) plastic deformation of the oxide

To achieve good resistance to oxidation, diffusion through the growing scale must be as low as possible. An ideal protective scale should:

a) form externally

b) be closely stoichiometric, so that diffusion through the oxide is slow

c) be free from cracks, pores and other defects

d) be resistant to spalling (this can be achieved by having a scale, which exhibits plastic deformation at high temperatures).

e) be chemically stable so that it does not react further with the environment leading to scale thinning.

f) not show any significant vapor species formation at the operating temperatures.

Considering the above conditions, it is seen that scales of chromia and alumina provide excellent oxidation resistance. High temperature alloys and coatings designed to resist oxidizing environments, therefore, rely on the formation of protective chromia

( $\text{Cr}_2\text{O}_3$ ) or alumina ( $\text{Al}_2\text{O}_3$ ) scales. However  $\text{Cr}_2\text{O}_3$  is not preferred for temperatures exceeding 1250 K, as there is significant evaporation of Cr as  $\text{CrO}_3$ .

## 2.6 Oxidation of Fe-Al systems

The advantage that aluminium imparts to the oxidation resistance of iron at elevated temperatures is well known and well documented. Generally, low-aluminium containing alloys, that is with less than about 1wt% Al, forms multilayer iron-oxide scales [16] composed of  $\text{Fe}_2\text{O}_3$  (externally) with inner layers of  $\text{Fe}_3\text{O}_4$  and  $\text{FeAl}_2\text{O}_4$  or  $\text{Al}_2\text{O}_3$  at the oxide-metal interface. Alloys containing 4 wt% aluminium, or greater formed external alumina scales but at alloy concentration of less than approximately 8-10 wt.% this is interspersed by iron oxide nodules. We are principally interested in iron-aluminide with sufficiently high amount of aluminium so that it forms a protective alumina scale.

Iron aluminides are known to be excellent alumina formers. Their oxide scale has been reported by various researchers to contain predominantly alumina with little iron. It is due to the thermodynamic stability of  $\text{Al}_2\text{O}_3$  relative to oxides of iron. The soundness and adherence of  $\text{Al}_2\text{O}_3$  scale to the underlying alloy determine the actual high temperature oxidation and corrosion resistance behaviour. From kinetics point of view, however, the selective oxidation of Al is found to occur only when the Al content in the alloy exceeds a critical value which according to Sykes and Bampfylde [17] is dependent on temperature, with 6% Al being sufficient at 900-1000°C; 9% is necessary at 1100°C and 11% at 1300°C. Iron aluminides have aluminum in sufficient quantities to form external alumina scale. Inspite of this fact, researchers often report the presence of small quantities of iron oxide in the scale. The following discussion therefore, emphasises on the thermodynamics and kinetics of  $\text{Al}_2\text{O}_3$  formation.

The aluminium levels present in  $\text{Fe}_3\text{Al}$  and their alloys are well in excess of the critical concentration and, as expected, alumina forms readily above approximately 500°C on exposure to oxidising conditions. The predominant surface product found on iron aluminides below 900°C is  $\gamma\text{-Al}_2\text{O}_3$ , while  $\alpha\text{-Al}_2\text{O}_3$  forms after oxidation at higher temperatures [18].

Alumina generally develops as either  $\alpha$ - $\text{Al}_2\text{O}_3$  or  $\gamma$ - $\text{Al}_2\text{O}_3$  during the oxidation of Fe-Al alloys [10].  $\alpha$ - $\text{Al}_2\text{O}_3$  forms at higher temperatures than  $\gamma$ - $\text{Al}_2\text{O}_3$ , is more desirable for conferring oxidation resistance and is highly stable. It belongs to the rhombohedral crystal system, with the oxygen ions being approximately hexagonally close packed and with trivalent cations occupying two-thirds of the octahedral interstices [19].  $\gamma$ - $\text{Al}_2\text{O}_3$  belongs to the cubic crystal system and may be thought of as a transition phase, which ultimately converts to  $\alpha$ - $\text{Al}_2\text{O}_3$  if the temperature is sufficiently high. Various other forms of  $\text{Al}_2\text{O}_3$  may exist as transition products. For example,  $\theta$ - $\text{Al}_2\text{O}_3$ ,  $\eta$ - $\text{Al}_2\text{O}_3$ ,  $\delta$ - $\text{Al}_2\text{O}_3$ ,  $\chi$ - $\text{Al}_2\text{O}_3$  or  $\kappa$ - $\text{Al}_2\text{O}_3$  may be produced by heating the alumina hydrates  $\text{Al}(\text{OH})_3$  or  $\text{AlOOH}$ ; the sequence of phases depends on the starting material, particle size, type of atmosphere, and impurities present. Such phases are unlikely to be encountered during high temperature Fe-Al alloy oxidation, with the exception of  $\theta$ - $\text{Al}_2\text{O}_3$ , which has been identified, chiefly during the early stages of oxide growth. Amorphous  $\text{Al}_2\text{O}_3$  has also been noted during the oxidation of Fe-Al alloys alongside  $\gamma$ - $\text{Al}_2\text{O}_3$  and iron oxides.

For Fe-28 (atom %) Al, at 800° and 900°C, the parabolic rate constants are reported to be essentially the same, implying that at higher temperatures, slower growing  $\alpha$ -phase of  $\text{Al}_2\text{O}_3$  replaces the  $\gamma$  and  $\theta$  forms of the oxide [20]. A similar behaviour has also been observed by Russian scientists, and they have attributed the effect to phase transformation in the oxide occurring at these temperatures range [21]. The extent of non-stoichiometry in  $\alpha$ - $\text{Al}_2\text{O}_3$  is small which also adds to the above factor leading to reduced rates of oxidation of iron aluminides at high temperature.

Boggs [22] has reported the appearance of  $\gamma$ - $\text{Al}_2\text{O}_3$  and  $\alpha$ - $\text{Al}_2\text{O}_3$  at temperatures above 600°C. The  $\gamma$ - $\text{Al}_2\text{O}_3$  forms as large crystals bearing an epitaxial relationship to the substrate. The  $\alpha$ - $\text{Al}_2\text{O}_3$  is observed as very small crystals in completely random orientations; the  $\alpha$ - $\text{Al}_2\text{O}_3$  appears to result from recrystallization of  $\gamma$ - $\text{Al}_2\text{O}_3$ . As temperatures are raised above 900°C, scales appear to contain more  $\alpha$ - $\text{Al}_2\text{O}_3$  and less  $\gamma$ - $\text{Al}_2\text{O}_3$ , although there seems to be no definite temperature at which the  $\gamma$ - $\text{Al}_2\text{O}_3$  disappears.

Babu [25] also found out the presence of transition aluminium oxides in the case of oxidation of Fe-25Al (at %) alloy in pure oxygen. At a temperature of 1225K and

1330K, he noted the presence of both  $\alpha$ -Al<sub>2</sub>O<sub>3</sub> and  $\theta$ -Al<sub>2</sub>O<sub>3</sub>, whereas at 1425K and 1530K he found that  $\alpha$ -Al<sub>2</sub>O<sub>3</sub> was the principal oxide. The iron aluminides oxidized at rates much lower than titanium aluminides.

### 2.6.1 Scale morphology

Rybicki and Smialek [23] oxidized NiAl + Zr (47.2 at % Al and 0.05 at % Zr) in dry air at temperatures of 1073K, 1173K, 1273K, 1373K and 1473K for a period of 100 hours. The surface morphologies of the  $\theta$ -Al<sub>2</sub>O<sub>3</sub> scales formed at 1073K and 1173K are shown in Figure 2.7(a) and 2.7(b), respectively. The scale at 1073K contained finely textured or nodular features aligned with polishing marks. At 1173K, whiskers were observed, which were probably representing outgrowths of the lower temperature nodules. According to Rybicki and Smialek [23], the  $\theta$  structure is a combination of nodules and whiskers as seen at the lower temperatures. At the higher temperatures, the nodules or whiskers were less apparent; instead, a network of oxide ridges or a lacy structure developed. The scale morphologies after oxidation at 1373K and 1473K are shown in Figure 2.8(a) and 2.8(b), respectively. The network often assumed a cellular appearance with radial spokes dividing the cells into wide segments.

Smialek and Doychak [34] observed a similar type of oxide morphology during the oxidation of Fe-40Al-1Hf (at %) in 1 atm air at 1173K, 1273K and 1373K. At 1173K the alloy formed a distinct, whisker morphology, which was associated with the fast-growing  $\theta$ -phase transition alumina. Oxidation at 1000°C produced spheroidization and coarsening of the residual whisker morphology and the appearance of concave cells. Further coarsening took place at 1100°C, as the cells were flattened and occupied the majority of the surface illustrated by Figure 2.9 and Figure 2.10. At the cell boundaries, a hint of ridge network and radial crack like patterns were also seen.

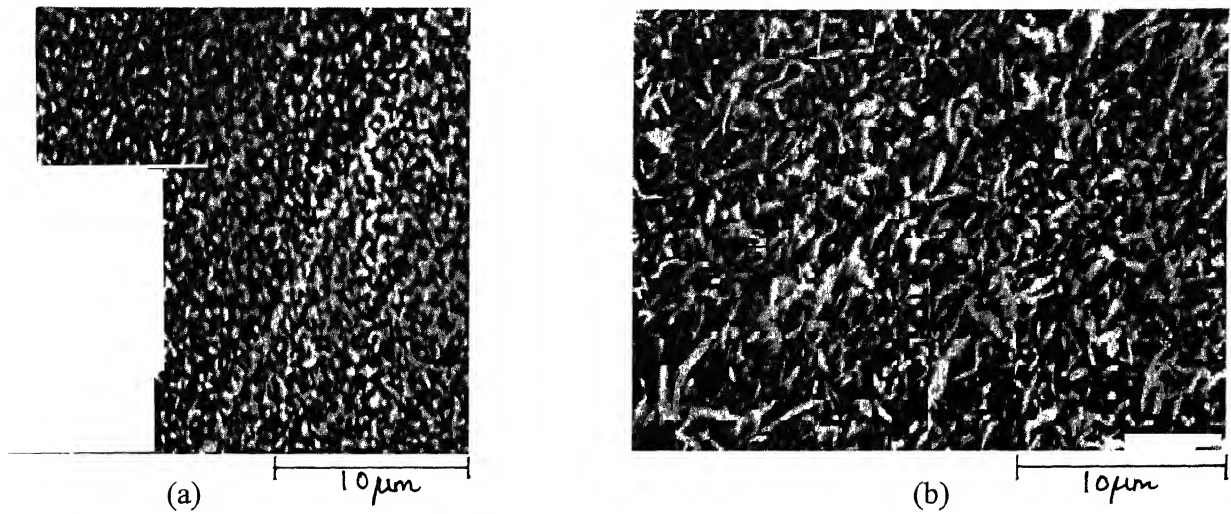


Figure 2.7 Development of  $\theta$ - $\text{Al}_2\text{O}_3$  whisker morphology on NiAl+Zr after 100hr oxidation [23] at (a) 1073K and (b) 1173K.

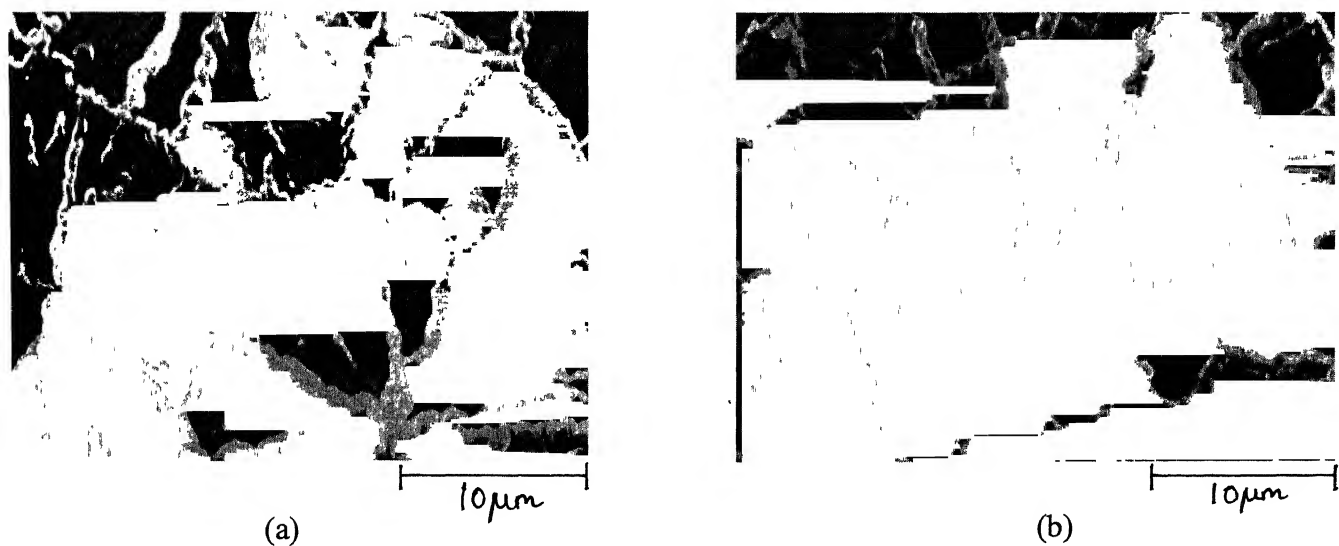
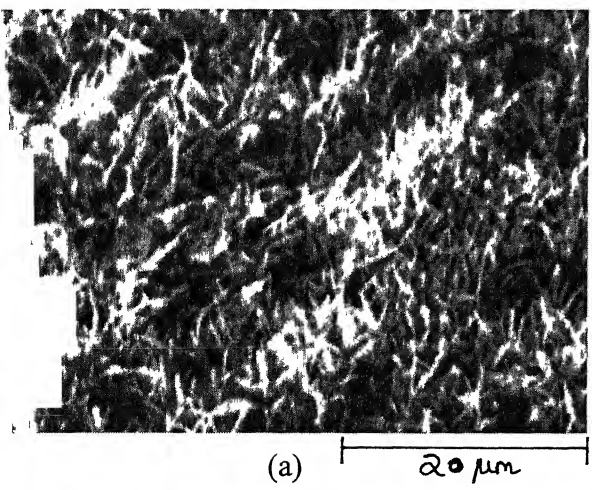
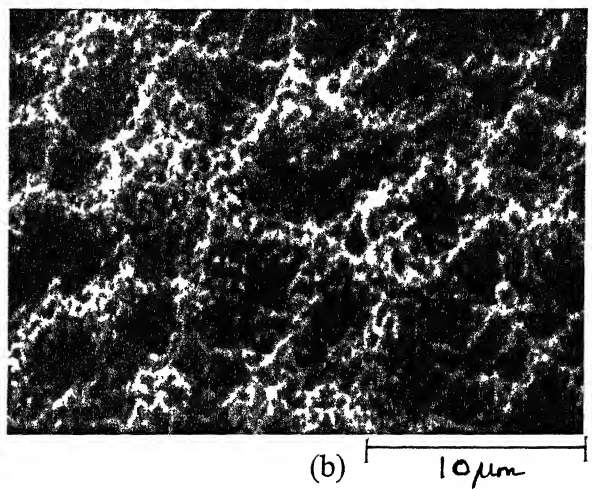


Figure 2.8 Fully developed ridge structure in mature  $\alpha$ - $\text{Al}_2\text{O}_3$  scales formed on NiAl + Zr after 100hr oxidation [23] at (a) 1373K and (b) 1473K

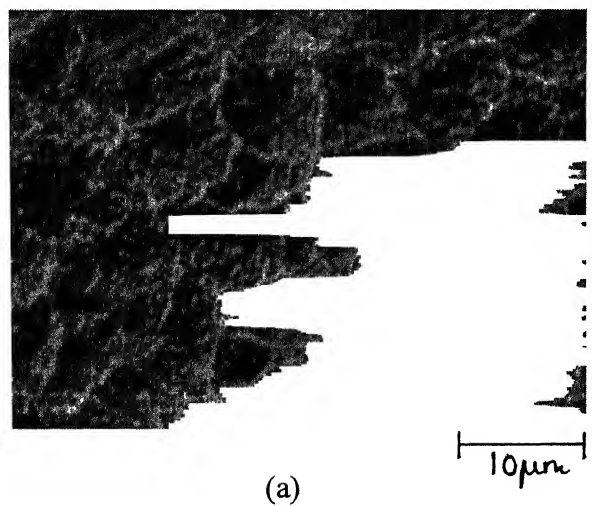


(a)  $20\mu\text{m}$

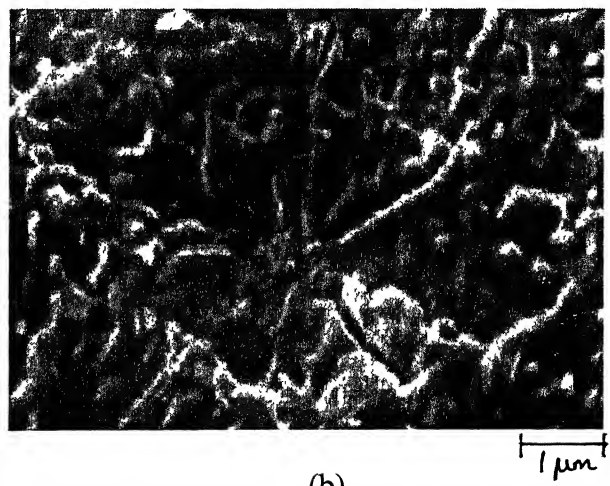


(b)  $10\mu\text{m}$

Figure 2.9 SEM morphology on FeAl-Hf alloy [34] showing (a) whisker formation at 1173K, and (b) cellular structure at 1273K.



(a)  $10\mu\text{m}$



(b)  $1\mu\text{m}$

Figure 2.10 (a) Cells and ridge networks formed on FeAl-Hf for oxidation at 1373K, (b) transformation cracks that are radial in nature could also be seen [34].

## 2.6.2 Kinetics of High Temperature Oxidation of Fe<sub>3</sub>Al

The oxidation kinetics at high temperatures, studied so far, are concerned with isothermal and cyclic oxidation behaviour. Thermogravimetry has been extensively used for this purpose. The high temperature oxidation behaviour of iron aluminides has been reported to be complex. Parabolic rate law has been considered in general as the basis for interpretation of experimental results in nearly all the previous studies [13, 25, 35]. However, as the oxidation behaviour of alloys can deviate to any extent from the quadratic parabola, other rate laws apart from the parabolic rate law has been observed by a few researchers. The following rate laws have been reported in the given temperature ranges [21]. The oxidation rates have been determined using ground alloys of various size fractions.

$$900\text{-}1000^\circ\text{C} : k / (\Delta W/A) = a - \log t, a = 8.45\text{min}$$

$$\text{Fe-25 atom\% Al } 1010\text{-}1060^\circ\text{C} : k / (\Delta W/A) = a - \log t, a = 7.37\text{min}$$

$$850^\circ\text{C} : (\Delta W/A) = k_1(1 - \exp(-k_2t))$$

where  $(\Delta W/A)$  is the weight gain per unit surface area. There are controversies as to whether outward diffusion of Al or inward grain-boundary diffusion of oxygen is rate controlling. There are equally good evidences in literature [6, 24] in support of both these mechanisms.

## 2.6.3 Significance of Aluminium content

For a pure binary Fe-Al alloy, Tomaszewicz and Wallwork [26] found that approximately 15% Al is needed to suppress internal oxidation and overgrowth of the alumina scale by iron oxides at 800°C. In contrast, titanium and niobium aluminides require much larger concentrations of aluminium (35-60%) to form protective alumina scales, even under the most favourable thermodynamic and environmental conditions. Recently, gravimetric studies showed that, under isothermal conditions, an abrupt transition to low oxidation rates occurred as the aluminium concentration of Fe-Al binary alloys was increased from 18 to 19.5% (Figure 2.11).

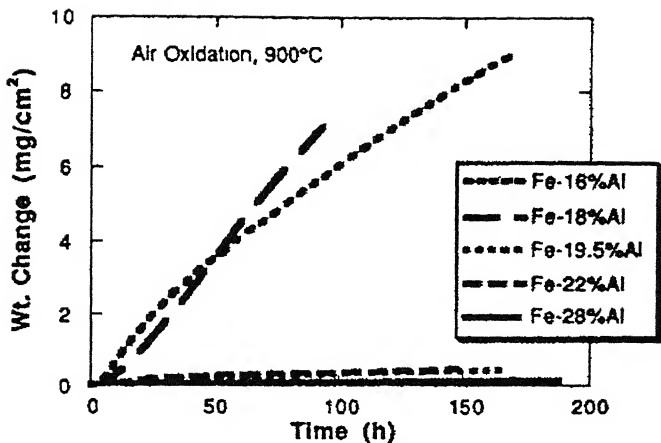


Figure 2.11 Effect of aluminium content on isothermal oxidation of Fe-Al binary alloys exposed to air at 900°C [18]

These are characterized by the sudden drop in the oxidation rate as the concentration of Al in the Fe-Al alloys is increased [18]. The aluminium content of the alloys and presence of other alloying elements have significant effects on the oxidation behaviour of these materials.

The formation of a protective alumina surface layer by selective oxidation acts to deplete the matrix of aluminium. If repeated spallation occurs, this depletion can be accelerated as the growth and loss of the scale more rapidly removes aluminium from the underlying alloy. When the concentration of this element falls below the critical value needed for protective scale (pure Al<sub>2</sub>O<sub>3</sub>) formation, much higher oxidation rates are recorded due to the growth of non-protective oxides on the surfaces. The high aluminium concentration of the iron aluminides assures that there is a substantial reservoir of this element to form new surface alumina for extended exposure periods and/or numerous cycles. Based on these considerations, the oxidative lifetime of iron aluminides should increase with increasing aluminium concentration and such has been observed experimentally as shown in Figure 2.12.

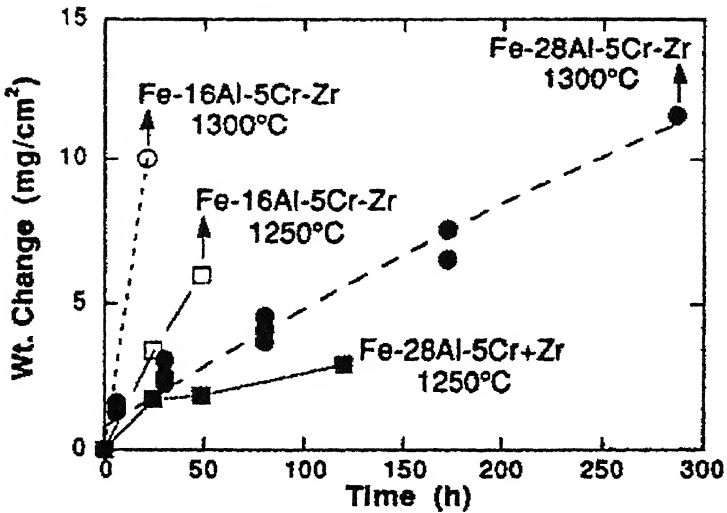


Figure 2.12 Weight changes of iron-aluminium alloys under cyclic oxidation conditions.

Arrows indicate very steep subsequent increases in weight due to formation of non-protective scales (iron oxides) that grow rapidly [18].

## 2.7 Oxidation of Fe-Al-C Alloys

Oxidation behavior of carbon-alloyed iron-aluminides has not yet been studied. Most researchers have done work on iron alloys containing about 5-10% Al and about 0.10%C. Boggs [22] studied the oxidation effects on Fe-Al-C alloys. The behaviour of Fe-5.5% Al alloys containing upto 0.10% carbon at 500°C in oxygen at 10 Torr was similar to that of the Fe-5%Al alloys. The oxidation rate of the Fe-5.99Al-0.10C alloy was intermediate between the low rate of the Fe-4.94Al alloy and the high rate of the Fe-0.11C alloy. The same three oxide phases,  $\text{Fe}_2\text{O}_3$ ,  $\text{Fe}_3\text{O}_4$  and  $\text{FeAl}_2\text{O}_4$  were formed both on Fe-4.94Al alloy and Fe-5.99Al-0.10C under these conditions. The oxides were nodular in nature. It was because of the localized oxidation of iron through the protective aluminium oxide film that forms at the high temperature that resulted in the growth of corn-like nodes of iron oxide.

Above about 700°C, the evolution of gas from the reactions between carbon and the iron oxides may interfere with the formation of a protective oxide film on iron-base alloys containing appreciable amount of carbon. The effect of carbon concentration on

the oxidation of the Fe-Al-C alloys at 800°C is shown in isometric projection in Figure 2.13.

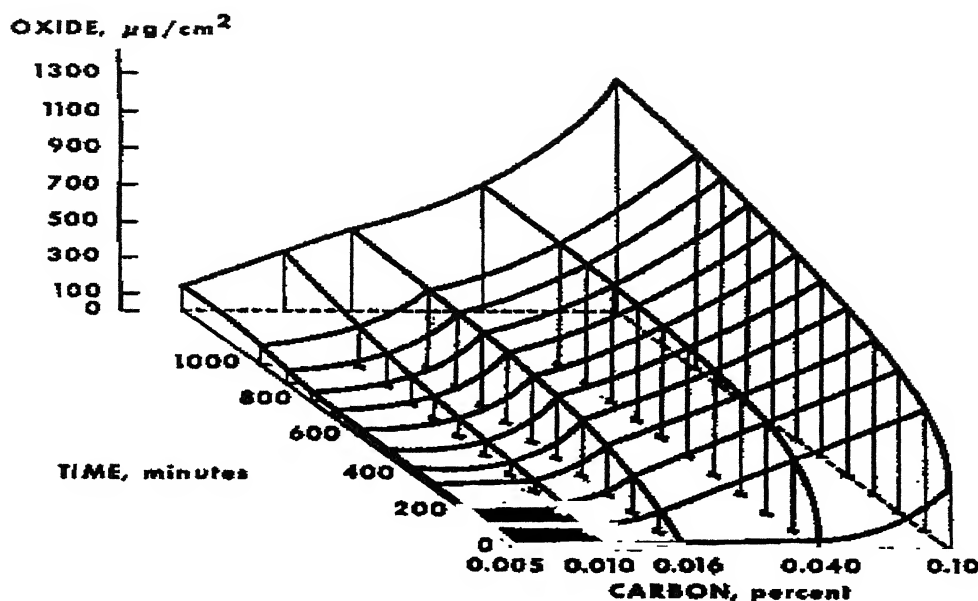


Figure 2.13 Effect of carbon concentration on the oxidation of Fe-5.5%Al-C alloys at 800°C in oxygen at 700 Torr [22].

A sharp increase in oxidation rate with increasing carbon content is clearly evident. Microscopic examination of oxidized specimens revealed that a thin passive alumina film covered most of the surface of the alloys but that the frequency with which iron oxide nodules disrupted this film increased with increasing carbon concentration. Most of the weight gain shown in the above figure reflects the growth of nodular oxide, not film.

There appears to be two ways in which carbon can interfere with the protective alumina and allow nodular iron oxide to nucleate. The direct oxidation of carbon at random sites in competition with iron and aluminium might leave holes in the film at which nodules might nucleate. Alternatively, carbon from the substrate can react with

iron oxides in the initial film to produce high-pressure CO pockets, which burst through the film and allow oxygen to reach the substrate, nucleating the nodular oxide.

Kao and Wan [27, 28], also noted that carbon in the alloy always increases the rate of oxidation of Fe-Al alloy. Their results on Fe-5.5Al-0.55C and Fe-7.5Al-0.65C alloy, demonstrated that the oxidation kinetics of the alloy followed a parabolic law, suggesting that the oxidation was controlled by a diffusion mechanism. They also observed three different kind of oxidation behaviour at different oxidation temperatures, which were essentially all parabolic in nature. After 600°C they could not observe a carbide-free layer (no decarburization) between the oxide scale and the matrix, suggesting that the outward diffusion of elemental carbon was not quick enough at that temperature. For 800° and 1000°C oxidation they observed clear decarburization regions between the oxide scale and the matrix. They were of the view that the carbide particles in the alloy decomposed at the higher temperature. This gave rise to carbon atoms, which diffused out and reacted with oxygen and finally evaporated. This made the carbide particles lose their stability and kept the decomposition continuously going, so that finally the carbide particles totally disappear from this region. They also observed oxide nodules on the surface of the specimen, like Boggs [22], which contained mainly FeO, Fe<sub>2</sub>O<sub>3</sub>, Fe<sub>3</sub>O<sub>4</sub>, FeAl<sub>2</sub>O<sub>4</sub> and some Al<sub>2</sub>O<sub>3</sub>.

## 2.8 Hot Corrosion

In addition to attack by reactive gases, alloys used in commercial environments, particularly those involving the combustion products of fossil fuels, undergo a mode of attack associated with the formation of a salt deposit, usually a sulphate, on the metal or oxide surface. This phenomenon is called Hot Corrosion. The severity of this type of attack, which can be catastrophic, has been shown to be sensitive to a number of variables including deposit composition, atmosphere, temperature and temperature cycling, erosion, alloy composition and alloy microstructure. The purpose of this would be to view the mechanism by which hot corrosion occurs. The examples used will be those associated with Na<sub>2</sub>SO<sub>4</sub> deposits, which are often encountered.

Once a deposit has formed on an alloy surface the extent to which it affects the corrosion resistance of the alloy will depend on whether or not the deposit melts, how

adherent it is, and the extent to which it wets the surface. A liquid deposit is generally necessary for severe hot corrosion to occur although some examples exist where dense, thick, solid deposits have apparently resulted in considerable corrosion.

Once the alloy surface has been partially or completely wet by the molten salt, conditions for severe corrosion may develop. The hot corrosion of virtually all susceptible alloys is observed to occur in two stages: an initiation stage during which the rate of corrosion is slow and a propagation stage in which rapid, often catastrophic, corrosion occurs. This is illustrated for the commercial alloy IN-738 [29] in Figure 2.14.

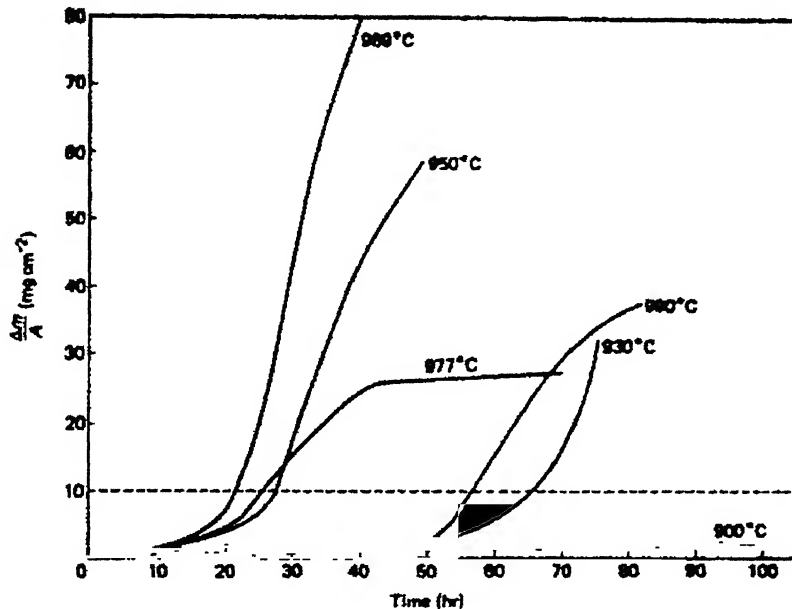


Figure 2.14 Mass change versus time for IN-738 coated with  $1\text{mgcm}^{-2}$   $\text{Na}_2\text{SO}_4$  in  $1\text{atm}$   $\text{O}_2$  [29].

During the initiation stage, the alloy is being altered to make it susceptible to rapid attack. This alteration may include depletion of the element responsible for forming the protective scale (usually Al or Cr), formation of sulphides in the alloy due to sulphur penetration through the scale, dissolution of oxides into the salt, and development of

growth stresses in the scale. This alteration can also result in shifts in salt composition towards more corrosive conditions. The length of the initiation stage varies from seconds to thousands of hours and depends on a large number of variables including alloy composition, alloy microstructure, salt composition, atmosphere, temperature, and extent of thermal cycling, salt thickness, specimen geometry and presence or absence of erosive conditions. In many cases, the end of the initiation stage follows the local penetration of the salt through the scale and subsequent spreading along the scale-alloy interface. This situation, in which the salt reaches sites of low oxygen activity and is in contact with an alloy depleted in Al or Cr, generally leads to the rapid propagation stage. The propagation stage can proceed by several modes depending on the alloy and exposure conditions.

One group of propagation mode includes the salt fluxing reactions. Sodium sulphate may be considered to be composed of a basic component  $\text{Na}_2\text{O}$  (or  $\text{O}^{2-}$  ions) and an acid component  $\text{SO}_3$ . The salt fluxing reactions include basic fluxing, in which the oxide scale reacts with  $\text{Na}_2\text{O}$  and dissolves in the salt as anionic species, and acid fluxing, in which the scale reacts with  $\text{SO}_3$  and dissolves as a cationic species. In a liquid sodium sulphate deposit, the sulphate ion decomposes according to



A sodium sulphate melt therefore has an oxygen ion, or  $\text{Na}_2\text{O}$ , activity of which is defined by the oxygen and sulphur dioxide potentials.

In *acid* fluxing, the oxygen ion concentration of the melt is low compared to the value required to maintain equilibrium in the dissociation reaction of the metal oxide according to



Correspondingly, with low oxygen ion concentrations in the sulphate melt, acid fluxing can occur when the metal oxide simply dissolves into the sulphate melt according to equation 2.5.

If the oxygen ion activity of the sulphate melt is high compared to that required to form complex anions according to equilibria such as



then complex ions can form and the metal oxide dissolves in the sulphate melt as a complex anion. This is known as *basic* fluxing. The two fluxing reactions are illustrated for NiO by the solubility plot shown in Figure 2.15.

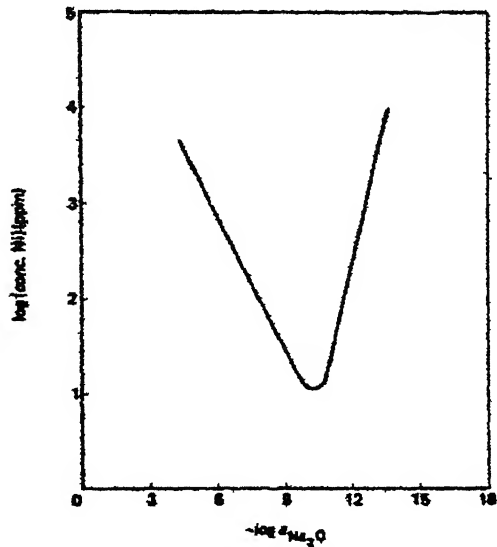
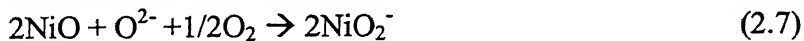


Figure 2.15 Solubility of NiO in fused  $\text{Na}_2\text{SO}_4$  at 1200K

There is a minimum solubility at an activity of  $\text{Na}_2\text{O}$  of  $10^{-10}$ . The solubility increases with increasing  $\text{Na}_2\text{O}$  activity (decreasing  $p_{\text{SO}_3}$ ) according to the reaction



which corresponds to basic fluxing and increases with decreasing  $\text{Na}_2\text{O}$  activity according to the reaction



which is acid fluxing. Similar solubility behaviour occurs for other oxides.

Of course the stabilities of the various complex anions vary and conditions, which may lead to the acid fluxing of one oxide, could equally cause basic fluxing of another oxide. The terms acid and basic are relative and refer to the reaction that occurs rather than to just the condition of the melt, i.e. for each oxide there is a relationship such as in Figure 2.15 for the condition of acid and basic fluxing. The curves for different oxides

are displaced to left or right of each other depending on the relative stabilities of the compounds involved.

There has not been much work reported in literature for the hot corrosion of Fe-Al systems using  $\text{Na}_2\text{SO}_4$  salt, but sulphidation, using  $\text{H}_2\text{S}$ , has been widely reported in literature for Fe-Al systems. According to Lee and Lin [30], the presence of molten alkali sulphate salts significantly increases the corrosion of iron aluminides in  $\text{SO}_2$ -containing mixed gases. A coating of  $\text{Na}_2\text{SO}_4 - \text{Li}_2\text{SO}_4$  salt on iron aluminides exposed in an oxidizing/sulphidizing gaseous environment (1%  $\text{SO}_2$  in air) at 605°C and 800°C led to corrosion rates that were at least a factor of ten higher than rates measured in the absence of the sulphate product. In contrast to the results discussed above, increased Cr concentrations (from 2 to 5%) somewhat mitigated the degradation by the molten sulphate, as did a higher Al level (36% versus 28%). The relative resistance of types 310 and 321 stainless steel was significantly better than that of iron aluminides [30].

In another study by Gesmundo et al [31], both  $\text{Fe}_3\text{Al}$  (27% Al-2.2% Cr-0.1% B) and  $\text{FeAl}$  (40% Al-0.05% Zr-0.06% B-0.085% C) were coated with  $\text{Na}_2\text{SO}_4$ -containing salts and exposed to a simulated combustion gas containing  $\text{O}_2$ , 0.5%  $\text{SO}_2$ , balance  $\text{N}_2$  (vol. %) at 600°C. Mass gains after 96 hours were 8 and 14  $\text{mg}/\text{cm}^2$ , respectively, for the  $\text{FeAl}$  and  $\text{Fe}_3\text{Al}$  alloys coated with  $\text{Na}_2\text{SO}_4 - 15$  wt%  $\text{V}_2\text{O}_5$  and between 4 and 5  $\text{mg}/\text{cm}^2$  for both alloys coated with pure  $\text{Na}_2\text{SO}_4$  or  $\text{Na}_2\text{SO}_4$ -10 wt%  $\text{NaCl}$ . The scales showed two main layers – an outer layer containing mainly iron oxides and an inner layer containing  $\text{Al}_2\text{O}_3$  and  $\text{Al}_2\text{S}_3$  with some Fe.

Recently Rodriguez et al [32] studied the hot corrosion of atomized Fe-40 at% Al, Fe-40Al + 0.1B and Fe-40Al + 0.1B+ 10 $\text{Al}_2\text{O}_3$ , using  $\text{NaVO}_3$  at 625°C and 700°C by polarization study. They also reported the occurrence of  $\text{Fe}_2\text{O}_3$  and  $\text{Al}_2\text{O}_3$  as the hot corrosion products.

All these studies indicate that the alumina scale is attacked by  $\text{Na}_2\text{SO}_4$  salts resulting in the oxidation of the other major element in the alloys, i.e. Fe. When  $\text{SO}_2$  is present in the atmosphere, the alumina is expected to be fluxed by the acidic mechanism (gas phase induced acid fluxing mechanism). As chromia is more resistant to this type of fluxing mechanism, it is not surprising to find that increasing the Cr content of the iron aluminide resulted in an increase in the hot corrosion resistance.

# **Chapter 3**

## **EXPERIMENTAL PROCEDURES**

This chapter describes the materials, test specimens; their preparation, experimental apparatus and the types of environments used for high temperature oxidation and hot corrosion studies. The experimental methods employed to characterize the materials and the scale products have also been described.

### **3.1 Materials**

The Fe-25 (atom %)Al (i.e.  $\text{Fe}_3\text{Al}$ ) intermetallic (which will be called NC) was obtained from the Defense Metallurgical Research Laboratory (DMRL), Hyderabad, in the form of a pancake of diameter 120 mm and thickness 15mm. This pancake was processed via the ingot metallurgy route. In order to minimize segregation, this pancake was homogenized at 1000°C for 4 hours. Thin strips were sectioned from the pancake. The base iron aluminide thin strips were rolled at 1000°C (in the disordered  $\alpha$ -phase field) and 80% deformation was imparted to each of them. The materials were soaked in a furnace for 1 hour before rolling. All the strips had a thin brown layer of oxide formed after rolling.

The composition of the base intermetallic was analyzed in a JEOL electron probe microanalyser (JXA-8600MX). The analysis was performed on many points at each specimen surface and the average value along with the standard deviation obtained was  $74.6 \pm 0.25$  Fe and  $25.4 \pm 0.25$  Al [33,36].

The carbon alloyed iron aluminide was obtained from DMRL, Hyderabad. Its composition (in atom %) was Fe-27.46Al-3.66C (which will be called 3C) [38]. In terms of wt %, the composition was Fe-16.0%Al-0.9%C. This material was obtained from DMRL, Hyderabad, in the form of metal strips of dimensions 110mm × 95mm × 2.97mm. The processing technique utilized to obtain these strips was as follows [37]. The iron aluminide ingots containing 15.55wt% Al (28 at%) were prepared by air induction melting (AIM) and chill cast into cast iron molds. Commercial purity aluminium and

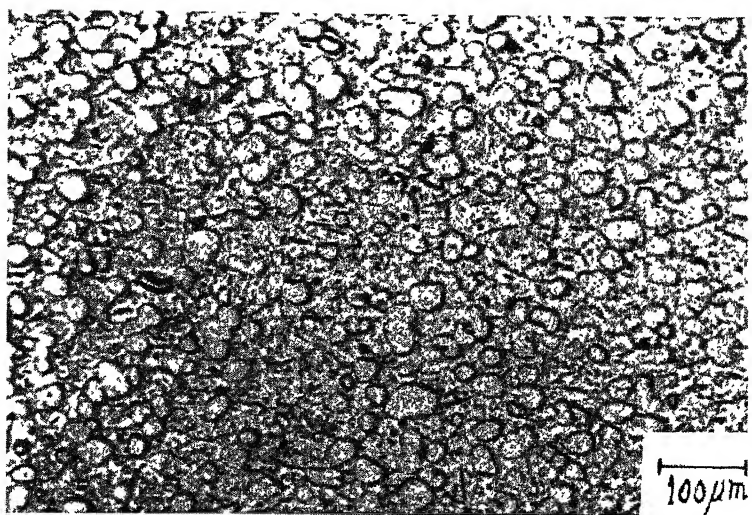
mild steel scrap were used as raw materials. The surfaces of the iron charge were cleaned by grinding. After melting, the slag product was skimmed off. Aluminium pieces were then added to the molten iron bath. The melt was held at 1620°C for a very short time (2 minutes) to prevent aluminium losses. The ingots were tested for their soundness in a radiography unit. These AIM ingots (55mm in diameter and 360mm long) were machined to 50mm diameter for refining in an electroslag remelting (ESR) furnace of 350 KVA capacity. A commercial prefused flux based on CaF<sub>2</sub> was used. The flux was preheated and held at 850°C for 2 hours before use to remove moisture. The iron aluminide electrode was remelted under flux cover and cast into 76mm ingot in a water-cooled steel mould. At the end of the process, the power supply was gradually reduced to impose a condition of hot topping. To check their soundness, the ESR ingots were also radiographed. The ingots were now forged to a reduction ratio of 70% and after forging they exhibited recrystallized grains [37].

Figure 3.1(a) shows the optical microstructure of the as-received 3C sample, and (b) shows the SEM micrograph of the same.

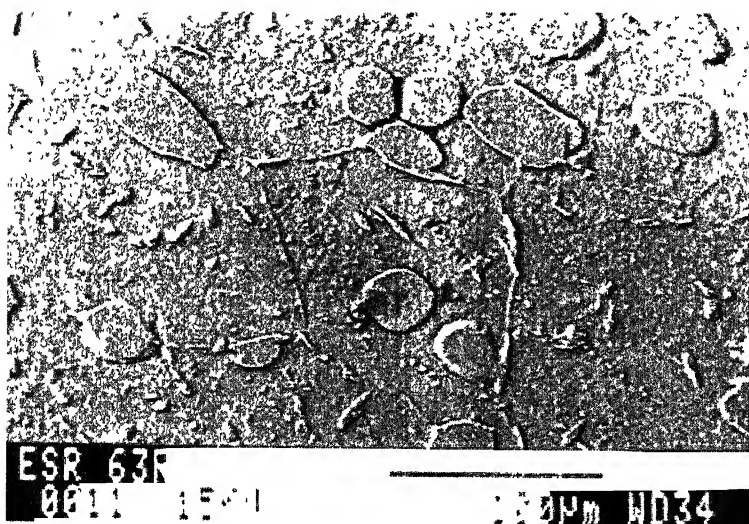
## 3.2 Oxidation Studies

### 3.2.1 Sample Preparation

Rectangular specimens were cut from the bulk alloy samples (both 3C and NC) by using a diamond cutter (Buehler-ISOMET). The specimen size could not be maintained to a standard uniform size due to the brittleness of the materials and also due to the limited amount of available specimen. The specimen lengths varied from 0.5 to 1.5 cm while their breadth varied from 0.4 to 1.0 cm. The thickness of the specimens varied from 0.08 to 0.4 cm. The specimens, after cutting, were mechanically polished to a 600-grit finish and degreased using acetone and alcohol before being used for each experiment.



(a)



(b)

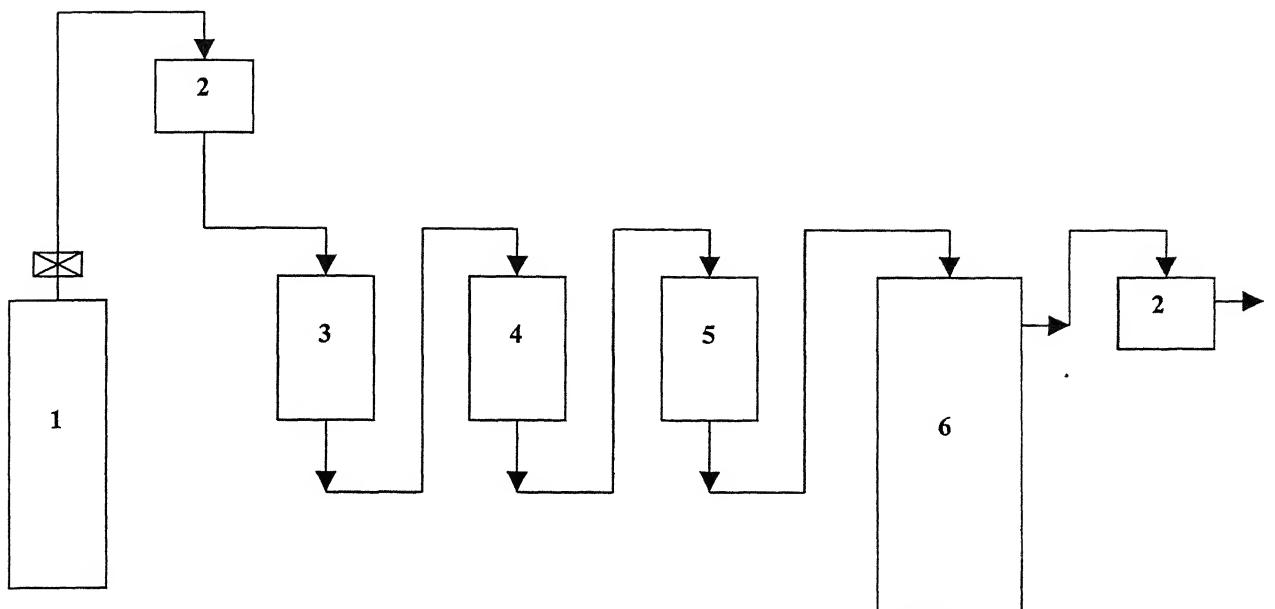
Figure 3.1 (a) shows the optical microstructure of the as-received 3C sample, and (b) shows the SEM micrograph of the same.

### **3.2.2 Apparatus for Isothermal Oxidation Experiments**

The thermogravimetric technique was employed for kinetic measurements. The apparatus consisted of a vertical furnace, a METTLER (Type-H16) single pan analytical balance, and gas train. These are described in details below. Figure 3.2 shows the schematic of the experimental set-up employed for the present investigation (both oxidation and hot corrosion studies) and Figure 3.3 shows the actual experimental set-up employed for the present experimental investigations.

#### **Furnace with Accessories**

A vertical furnace of 250mm length was employed to carry out the oxidation and hot corrosion tests. The temperature of the furnace was controlled within  $\pm 2\text{K}$  by an ON-OFF type temperature controller (Toshniwal Instrument Pvt. Ltd., India), actuated by a Pt/Pt-10%Rh thermocouple. The thermocouple emf was measured by a four-digit millivolt-meter (SONIT, Type SE-402-4). A mullite tube (45mm inner diameter and 460 mm length) acted as the reaction chamber. The mullite tube was fitted with silicone rubber stopper at the top to provide airtight fitting covers. Gas inlet tube and outlet tubes were inserted through the top of this reaction chamber through the silicone rubber stopper. All these tubes were glass fitted with rubber tubing and sealed with a sealant. Teflon tapes were tightly wound on the locations where the glass tube was fit with the rubber tube to avoid the leakage of gas from the connections. Temperature profiling of the furnace showed that a constant temperature zone of about 25 to 30 mm was obtained at the centre of the furnace. The specimen was placed inside a quartz crucible (or bucket, made especially for the purpose of this experimental set-up) with three holes at the bottom of the crucible to allow the easy passage of gas. The buckets were of 15mm in diameter and 20mm in length. The quartz crucible was then hung from the top of the furnace using a platinum wire into the reaction zone of the reaction chamber. The oxidation specimens were placed in the quartz crucible.



1. Gas Cylinder

2. Gas Bubbler

3. Ascarite Column

4. Anhydrous  $\text{CaCl}_2$  Column

5. Drierite Column

6. Furnace

Figure 3.2 Schematic Diagram of the experimental set-up for the Oxidation and Hot Corrosion Process

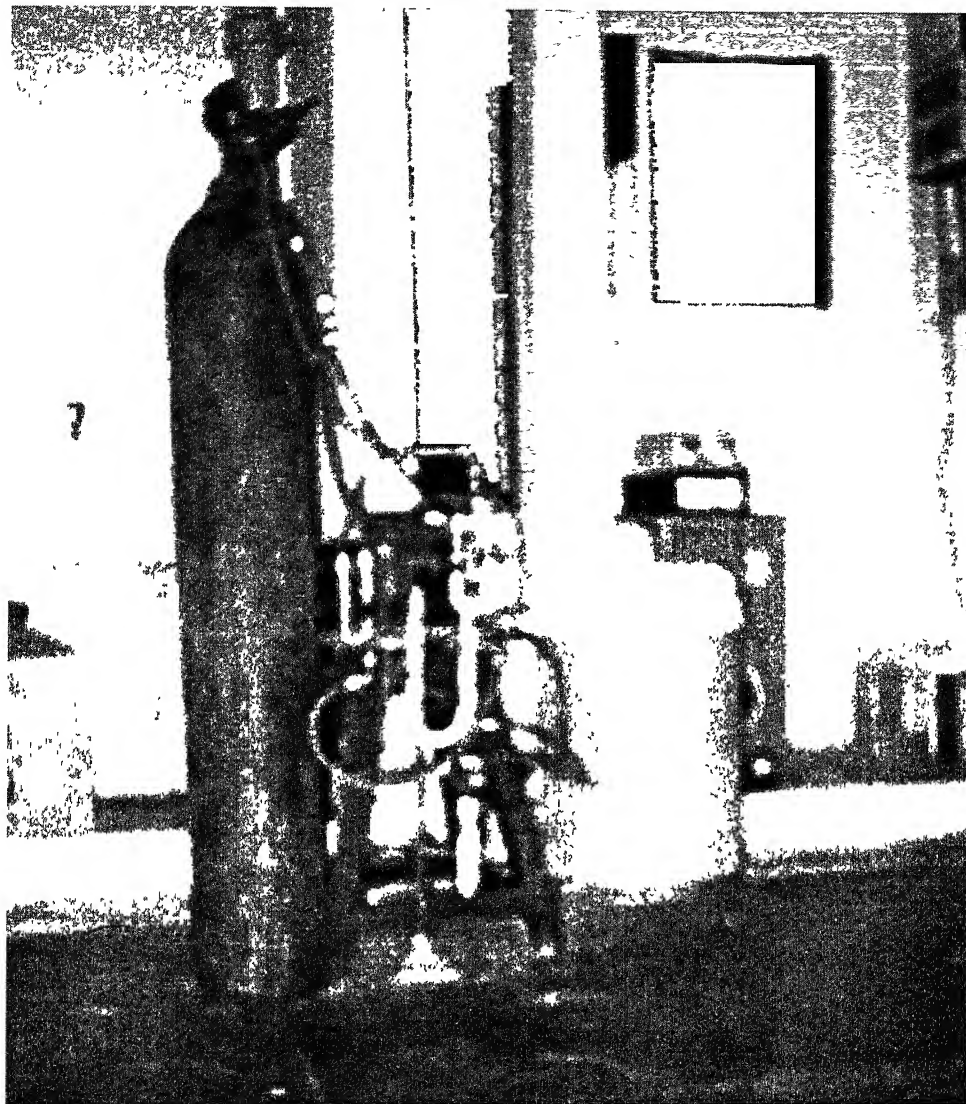


Figure 3.3 Experimental set-up employed for the oxidation and hot corrosion process

## Gas Train

The purpose of the gas train was to monitor the flow of the gas and purify it from impurities. Pure oxygen gas was passed through a bubbler and capillary flow meter. The gas was then passed through Ascarite column to remove carbon dioxide. Next, it was passed through anhydrous Calcium chloride and Drierite ( $\text{CaSO}_4$ ) columns successively before introduction into the reaction chamber. Drierite has a low equilibrium residual water vapour pressure and therefore, it was used after the anhydrous calcium chloride column in the gas train for efficient removal of moisture. The outlet gas was also passed through a bubbler to ensure that the flow of gas was being maintained through the system.

### 3.2.3 Experimental Procedure

The above-mentioned apparatus was used to study the isothermal oxidation and hot corrosion kinetics of the iron aluminide intermetallics at different temperatures. Initially, a few trial runs were carried out to fine tune the experimental apparatus. These trial runs helped in the following ways, besides familiarization with the handling of balance and accessories.

- (i) The possible weight gain values that could be anticipated.
- (ii) Sample introduction and removal times were standardized.
- (iii) Gas flow rate was also standardized.

Oxidation experiments were carried out isothermally in oxygen gas. The oxidation experiments on both the types of specimens were carried out at temperatures of 1100 K, 1225 K and 1330 K. Once the furnace attained the test temperature, sufficient time (10 to 15 minutes) was allowed for temperature to stabilize. The furnace was then flushed with oxygen to remove all entrapped air and to maintain the test environment condition inside the furnace before introduction of the sample.

The oxidation sample with freshly prepared surfaces was weighed outside in the analytical balance, and then placed inside the quartz crucible, which was hung from a platinum wire into the reaction chamber (i.e. introduced inside the furnace). The gas flow rate was constantly maintained at  $0.2 \text{ cm}^3/\text{s}$  (STP). The whole system was made gas tight (in order to prevent the entry of the atmospheric air) by tightening the silicone rubber

stopper on the top of the reaction chamber (mullite tube). The sample and furnace temperatures were equalized by allowing a short time (2 to 3 minutes) before the timing of the experiment was begun.

The quartz crucible was taken out from the furnace after fixed intervals of time: 0.5, 1, 2, 4, 8, 16, 24, 32 and 65 h. The weight of the sample was recorded using a single pan analytical balance. The readings in the balance could be taken upto 6 places of decimal (in grams). The weight variation is of the order of some milligrams for these types of aluminides on high temperature oxidation. Before the sample was taken out from the quartz crucible for every weight-change reading, it was cooled in the topmost portion of the furnace in the gas train for a maximum of 5 minutes to help lower the stresses due to thermal gradient which might affect the sample and induce spalling. After the end of the oxidation experiment (which for every experiment was fixed for 65 hours), the flow of oxygen gas was stopped. The crucible was taken out from the furnace and the sample was taken out from the crucible, cooled to room temperature, weighed in the balance and kept in a plastic vial, before being wrapped with tissue paper for further studies. In cases where some scale spallation occurred (upon cooling during removal from the furnace as well as outside the furnace), the spalled mass was collected and weighed together wherever possible.

### 3.3 Hot Corrosion Study

The kinetics and mechanism of salt-induced attack (called as hot corrosion) at the several different temperatures were studied by accelerated oxidation testing. In this type of testing, the alloy specimen was initially coated with a thin film of salt ( $\text{Na}_2\text{SO}_4$ ) and then exposed at the desired temperature in a slowly flowing, controlled gaseous environment [39]. The kinetics of the hot corrosion reaction at high temperatures was monitored by measuring the weight changes as a function of time, in a fashion similar to that of the oxidation experiments. The hot corrosion tests were carried out on the two alloys: Fe-25Al (NC-sample) and Fe-27.46Al-3.66C (3C-sample). Specimens of both these two alloys were cut by a diamond cutter (Buehler-ISOMET) from the bulk material. The alloy specimen surfaces were then polished to 600-grit finish and degreased with acetone and alcohol before every experiment. The salt deposit was applied to a warm

(~150°C) specimen by using a brush, to give a uniform coat of the aqueous solution of the desired salt ( $\text{Na}_2\text{SO}_4$ ) on the surface of the specimen. In all tests, a surface coverage of  $2.5 \pm 0.2 \text{ mg/cm}^2$  of salt was used.

The furnace and the accessories used were the same as that used for oxidation studies. The gas used for hot corrosion studies was pure oxygen, which was purified by being passed through columns for removal of moisture and  $\text{CO}_2$ . This procedure was again similar to that used in the oxidation experiments.

To start a test, the coated (by  $\text{Na}_2\text{SO}_4$ ) samples were placed inside the crucible, which was then lowered inside the reaction chamber by the help of platinum wire as before. The remaining experimental procedure for conducting the hot corrosion experiment was same as that for the oxidation experiments. There was noticeable scale spallation all throughout the hot corrosion experiments, but mostly at the two higher temperatures. The spalled scales were collected and weighed whenever they occurred and kept carefully along with the sample for further characterization and studies.

## 3.4 Scale Characterization

It is important to understand the nature of scale (like morphology, composition, etc.) to understand the kinetics of oxidation as well as to obtain insights on the mechanisms involved. Therefore, characterization of the scales (obtained after the high temperature oxidation studies) constituted an important component of the present study. The techniques adopted for characterizing the corrosion products of the oxidation experiments (oxides, etc.) are discussed below.

### 3.4.1 Visual Observation of Scales

In the present study, the alloys were exposed to oxygen gas at high temperatures. The resulting scales were observed by unaided eye or by low magnification microscope after the sample was taken out of furnace. This type of examination is important because subsequent microscopic examination could be carried out only at specific locations on a section. Visual observation provides the important information about variation over a macroscopic scale on the specimen surface. Observations regarding scale colour, scale adherence (or spalling characteristics) and uniformity were recorded.

### **3.4.2 X-Ray Diffraction**

All the oxidized and hot corroded samples were selected for X-ray diffraction (XRD) studies to identify the scales formed. An ISO Debyeflex 2002D diffractometer with monochromator (Rich-Seifert and Co., Germany) was employed. The surfaces of the oxidized samples analyzed directly using X-rays. In most of the cases, the scale thickness was relatively low, and therefore, preparation of powder sample from the very thin scale was unnecessary. Therefore, these XRD studies addressed the scales that were present actually on the surface and in several cases, diffraction peaks from the substrate was also obtained. A special holder was used for gripping the samples in such a way that the x-ray radiation was incident primarily on the surface, throughout the range of scan.

In some cases, the surface scale had peeled off from the substrate on cooling. These samples were preserved and were used for X-ray diffraction studies. The scales were fixed on a glass side using an acrylic solution and the XRD pattern was taken with the x-ray incident on the sample. Most of the specimens were scanned at a low speed with a low count rate.

The settings of the X-ray diffractometer were as follows:

- (i) Radiation :CuK<sub>α</sub> ( $\lambda = 1.54184\text{Å}$ )
- (ii) Scan speed (2θ) :3 degrees/min
- (iii) Counts per minute :5K
- (iv) Time constant :10 sec
- (v) Current :20mA
- (vi) Voltage :30kV

### **3.4.3 Scanning Electron Microscopy**

A scanning electron microscope (SEM) (JEOL-JSM 840A) was employed for topological observation of the surfaces of the specimens, which had earlier been subjected to XRD studies. Various aspects of the morphology like the topological features, distribution, porosity, etc. of external scale were recorded. The morphologies of scales after spalling were also recorded. The surface scales were mostly poor electrical conductors. Therefore, in order to prevent building of space charge during SEM observation, a very thin Au-Pd alloy coating was provided on the outer surface by

sputtering in order to make the surface electrically conducting. The coating does not interfere with the microscopic features. Morphological observations were made at various locations and photographs were taken at various magnifications.

#### **3.4.4 EPMA Study**

A JEOL electron probe micro-analyser (JXA-8600MX) was used to obtain qualitative analysis of some phases present in the system. The qualitative analyses were mainly done during cross-sectional study of the 3C and NC alloy subjected to hot corrosion experiments at the two high temperatures. Analysis was also performed from the surface scale of the specimen in one case. This was done mainly to get an insight into the type of product formed during the hot corrosion experiments.

#### **3.4.5 Fourier Transform Infrared Spectroscopy**

The oxidation and hot corrosion products from some selected experiments were analysed using fourier transform infrared spectroscopy (FTIR). The oxides and other phases present can be identified based on the characteristic absorption in the IR range (vibrational spectra). The fourier transform infrared (FTIR) spectra were recorded at room temperature using a Nicolet Magna 750 Series 2, USA, FTIR system (at DMSRDE, Kanpur). The scales were removed from the surface and were pressed in discs using spectroscopically pure KBr.

### **3.5 Electroless Nickel Plating**

Electroless nickel plating was provided on the samples (both oxidised and hot corroded) to give a uniform coat of metallic Ni on the surface of the sample so that the cross-section of the samples (along the thickness direction) can be studied after mounting it on epoxy. Bare samples without any Ni coating would not give proper result when observed transversely in SEM as it was difficult to distinguish the scale from the mount material.

The solution used for electroless nickel plating consisted of [40]: nickel chloride ( $\text{NiCl}_2 \cdot 6\text{H}_2\text{O}$ ) – 30gm/litre, sodium hypophosphite ( $\text{NaH}_2\text{PO}_2 \cdot \text{H}_2\text{O}$ ) – 10gm/litre, sodium citrate ( $\text{Na}_3\text{C}_6\text{H}_5\text{O}_7 \cdot 2\text{H}_2\text{O}$ ) - 100gm/litre, ammonium chloride ( $\text{NH}_4\text{Cl}$ ) – 50gm/litre. The

solution, stirred with a magnetic stirrer, was maintained at the desired pH (preferably between pH 8 to 9) by adding ammonia solution and temperature was maintained within  $85\pm1^{\circ}\text{C}$  using a thermostat bath. The time for coating was fixed for 60-75 minutes.

The samples were suspended with the help of a cotton thread into the coating solution. After coating for the requisite amount of time, the samples were taken out and washed in distilled water, followed by drying in a blower. Then they were taken for mounting in epoxy on a mounting press SIMPLIMET-2 (BUEHLER). The transversely mounted specimens were prepared as before by grinding till 600-grit finish for observation under SEM along the thickness direction.

# **Chapter 4**

## **RESULTS**

The results of the oxidation and hot corrosion experiments conducted on Fe-25Al (henceforth called NC) and Fe-27.46Al-3.66C (henceforth called 3C) alloys would be discussed. The experiments have been carried out at temperatures of 1100K, 1225K and 1330K. The time of exposure in pure oxygen environment was 65 hours for all the experiments.

### **4.1 Measurement Limitations**

#### **4.1.1. Temperature Measurement**

A Pt/Pt-10% Rh thermocouple, placed inside the reaction chamber, allowed furnace temperature control within  $\pm 2\text{K}$  at the constant temperature zone. The measurement thermocouple was placed within 10-15 mm below the sample in the constant temperature zone. Axial temperature profiling in and around hot zone showed that the sample temperatures were likely to differ from control temperature by about  $\pm 2\text{K}$ . Furthermore, the thermocouples were calibrated against a standard thermocouple. Thus, considering all sources of error in temperature measurement, the overall temperature measurement error may be taken as  $\pm 3\text{K}$ .

#### **4.1.2. Weight Gain Measurement**

The single pan analytical balance was sensitive to weight changes of the order of  $10\mu\text{g}$ . Precautions were taken for damping the vibrations of the sample hanging assembly, in order to attain such sensitivity in measurement. The weight gain after each time interval was taken with utmost precaution to prevent scale spallation (due to mechanical shock during handling of the specimen), while being taken out and being placed inside the furnace.

Babu [25] performed oxidation of the NC (Fe-25 at % Al) alloy in a Cahn 1000 electrobalance continuously (thermogravimetrically) for 24 hours and his results are

compared with the present results in Figure 4.1, which shows the  $(\Delta W/A)^2$  vs.  $t$  plot for the NC alloy at the two temperatures of 1225K and 1330K. Difference is noted in the nature of the oxidation rates obtained by Babu and in the present investigation. Higher rates were observed when the experiments were conducted non-continuously because higher weight gains are usually observed on cyclic oxidation. These conditions were applicable in the present investigation as the samples were taken in and out of the furnace during the weight gain measurement after some definite time intervals. On the other hand, Babu [25] obtained weight gain continuously using a Cahn electrobalance.

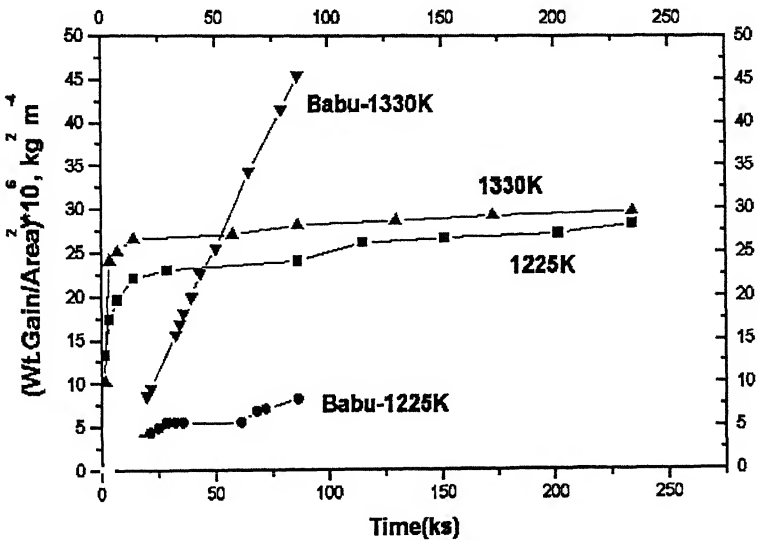


Figure 4.1 Comparison of  $(\Delta W/A)^2$  vs. time plots for oxidation of 3C in pure oxygen with Babu [25]. The lines joining the data points are for visual aid only.

## 4.2 Evaluation of Rate Constant

As stated in Chapter 2, the kinetics of high temperature oxidation can be analyzed by rate laws (like parabolic, linear, paralinear, etc). Literature review showed that most of the investigators employed parabolic rate law as the basis of interpretation of the weight gain vs. time data [35, 27, 28]. Therefore, parabolic rate law was first considered as the basis of data processing and interpretation of results in this investigation as well. However, determination of rate constants was carried out by two other methods. These

methods as well as their comparisions and relative evaluations have been presented in this section.

#### 4.2.1 Determination of Parabolic Rate Constant ( $k_p$ )

The raw ( $\Delta W/A$ ) versus  $t$  data for all the experiments is presented in Appendix A. The parabolic rate constant ( $k_p$ ) is related to ( $\Delta W/A$ ) (weight gain per unit surface area of specimen) and exposure time ( $t$ ) as in eq. 2.3. The rate constant  $k_p$  was obtained from the slope of the linear regression fitted line of  $(\Delta W/A)^2$  vs.  $t$  plot. The parabolic rate constants for all the experiments conducted in the study are presented in Table 4.1. Figures 4.2 through 4.5 show the nature of fit of parabolic rate law for the oxidation and hot corrosion experiments for the alloys NC and 3C. It may be noticed that the obedience to parabolic rate law was only approximate.

In the case of oxidation of NC alloy, the nature of the plot (Figure 4.2) indicated two regions where different parabolic rate constants applied; one encompassing the initial stages of oxidation (up to 2 hours approximately) and the other, the later stage. These two values of  $k_p$ , i.e.  $k_{pI}$  and  $k_{pII}$ , were determined and these are shown in Table 4.2 for NC alloy.

**Table 4.1 Summary of rate constants processed from the data of the thermogravimetric experiments**

Matl.	Temp. (K)	OXIDATION			HOT CORROSION		
		$k_p \times 10^9$ ( $\text{kg}^2 \text{m}^{-4} \text{s}^{-1}$ )	$k_m$	$m$	$k_p \times 10^9$ ( $\text{kg}^2 \text{m}^{-4} \text{s}^{-1}$ )	$k_m$	$m$
NC	1100	0.0071	$1.28 \times 10^{-31}$	9.47	0.5461	$3.20 \times 10^{-26}$	11.22
	1225	0.0465	$1.05 \times 10^{-41}$	15.67	9.8	$4.38 \times 10^{-9}$	2.69
	1330	0.0411	$6.50 \times 10^{-39}$	14.62	226.6	$0.26 \times 10^{-6}$	2.34
3C	1100	0.0553	$3.18 \times 10^{-14}$	3.35	0.01702	$3.96 \times 10^{-11}$	1.90
	1225	0.0422	$1.80 \times 10^{-18}$	5.23	3.4	$1.21 \times 10^{-9}$	2.37
	1330	0.0629	$2.98 \times 10^{-15}$	3.76	26.8	$3.48 \times 10^{-9}$	3.28

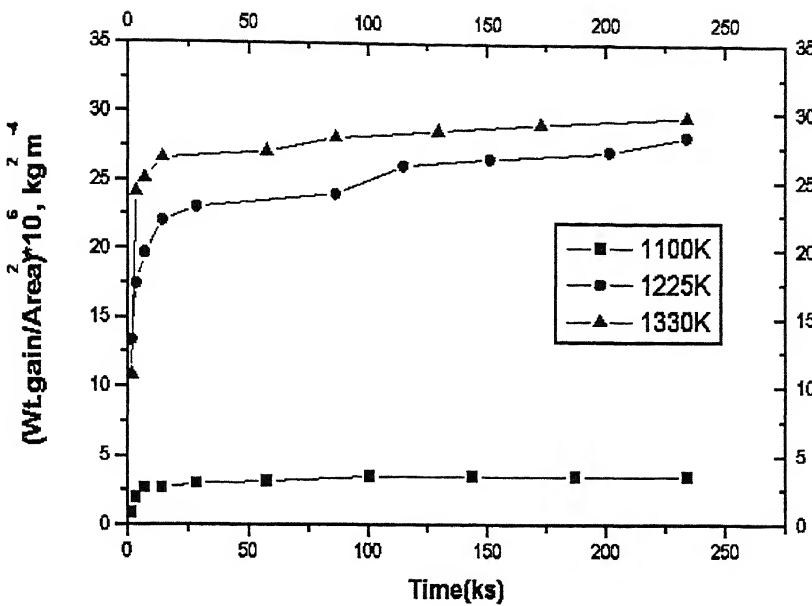


Figure 4.2  $(\Delta W/A)^2$  vs. time plots for oxidation of NC in pure oxygen. The lines joining the data points are for visual aid only.

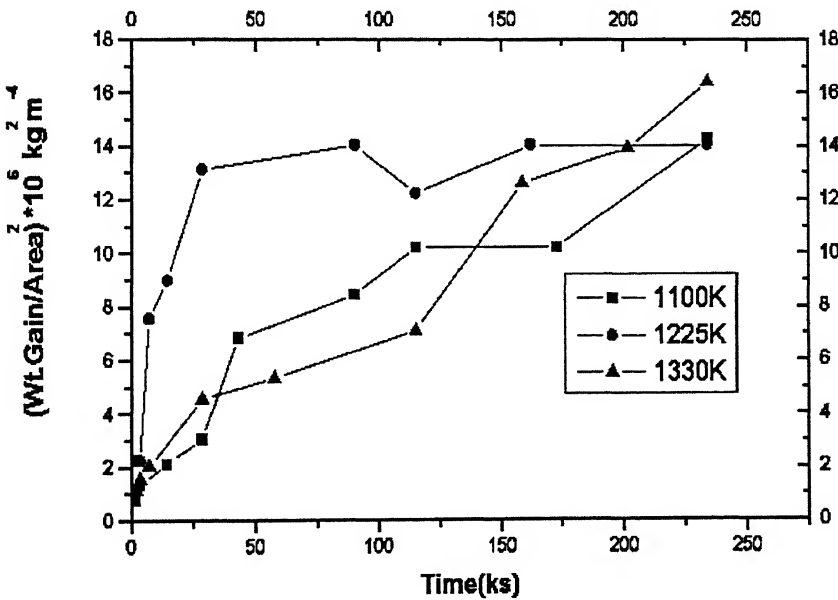


Figure 4.3  $(\Delta W/A)^2$  vs. time plots for oxidation of 3C in pure oxygen. The lines joining the data points are for visual aid only.

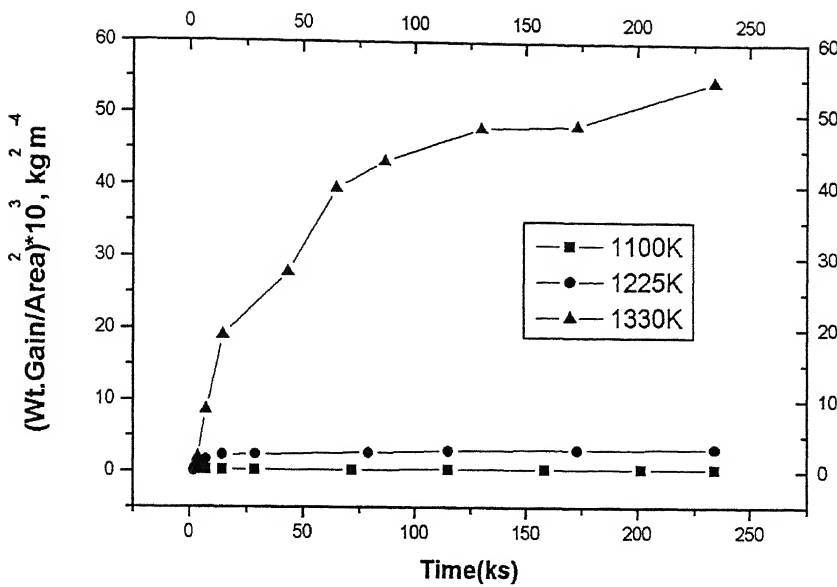


Figure 4.4  $(\Delta W/A)^2$  vs. time plots for hot corrosion of NC in pure oxygen. The lines joining the data points are for visual aid only.

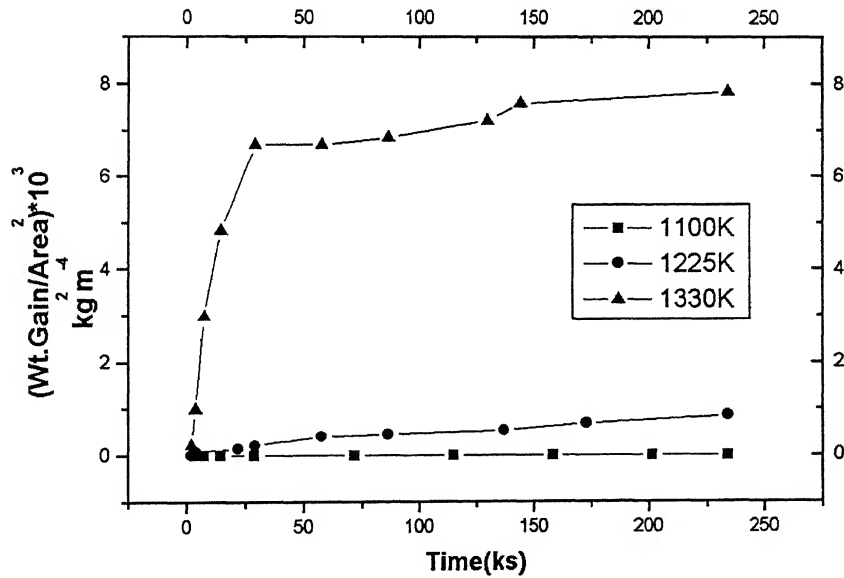


Figure 4.5  $(\Delta W/A)^2$  vs. time plots for hot corrosion of 3C in pure oxygen. The lines joining the data points are for visual aid only.

**Table 4.2 The parabolic rate constants for the first and second stages of oxidation of alloy NC in oxygen at the three temperatures**

$k_p \times 10^9$ ( $\text{kg}^2\text{m}^{-4}\text{s}^{-1}$ )	TEMPERATURE		
	1100K	1225K	1330K
$k_{pI}$	0.3135	1.0916	2.3011
$k_{pII}$	0.0037	0.0274	0.0147

#### 4.2.2 Determination of Rate Constant by Power Law Fitting

In view of the observed deviation from parabolic behavior in some cases, it was decided to also process the experimental data by assuming a power law as follows:

$$(\Delta W/A)^m = k_m t \quad (4.1)$$

$$\text{or, } \log (\Delta W/A) = (1/m) \log k_m + (1/m) \log t \quad (4.2)$$

The rate constant  $k_m$  and  $m$  were estimated from linear regression fitting of  $\log (\Delta W/A)$  vs.  $\log t$  data for each experiment. The inverse of slope will give the value of  $m$  and  $k_m$  can be obtained from the intercept of the best-fit line. The parabolic law corresponds to value of  $m = 2$ , and linear rate law corresponds to value of  $m = 1$ . The above procedure is a purely empirical method of data fitting, which provide insights into the possible nature of oxidation. Table 4.1 also includes the values of  $m$  and  $k_m$  for all the experiments conducted. In the case of oxidation of NC the values of  $m$  deviated significantly from 2 and the possible reasons for the same will be addressed in the following sections. The different  $m$  values observed may very well be caused by change of scale characteristics with time thus changing the diffusivities of ionic/molecular species across the scale with progress of reaction. In that case, even though oxidation rate may be controlled by diffusion through the oxide scale, the value of  $m$  may significantly differ from 2. For the purpose of analysis and comparison, the parabolic rate constant  $k_p$ , obtained based on parabolic law is more preferable, since the parabolic rate constant  $k_p$  has a theoretical

basis and the earlier investigators have employed it for comparison with literature. It was, therefore, decided to employ  $k_p$  as a measure of rate constant for further discussions.

#### 4.2.3 Variation of Parabolic Rate Constant ( $k_p$ ) with Temperature

It has been the normal practice to correlate the overall parabolic rate constant ( $k_p$ ) and temperature through a Arrhenius-type equation:

$$k_p = k_o \exp(-Q_{eff}/RT) \quad (4.3)$$

where R is the universal gas constant,  $k_o$  the pre-exponential factor, T the temperature in K, and  $Q_{eff}$  the effective activation energy. However this relation is valid if only one of the kinetic steps controls the rate. Parabolic law assumes that the rate of oxidation is controlled by diffusion through the oxide scale. Deviations from the parabolic were observed, as discussed earlier. Moreover, the nature of the scales on these alloys changed with temperature. This would be addressed in details while discussing the morphological observations of the scales. As the properties of the medium of diffusion vary with temperature, the effect of this variation will get incorporated in the variation of rate with temperature, and consequently on  $Q_{eff}$ . Therefore,  $Q_{eff}$  is merely a temperature coefficient and not true activation energy. Figure 4.6 shows the variation of the experimentally determined values of  $k_p$  with temperature for the oxidation and hot corrosion experiments. The slopes of the linear best-fit lines of data points provided the values of  $Q_{eff}$ , which are tabulated in Table 4.3.

**Table 4.3 Effective activation energy ( $Q_{eff}$ ), in kJ/mol estimated from the LOG  $k_p$  versus 1/T plots**

Material	Condition	Oxidation	Hot Corrosion
3C	$k_p$	4.65	395.39
NC	$k_p$	98.19	314.64
NC	$k_{pI}$	105.88	-
NC	$k_{pII}$	80.44	-

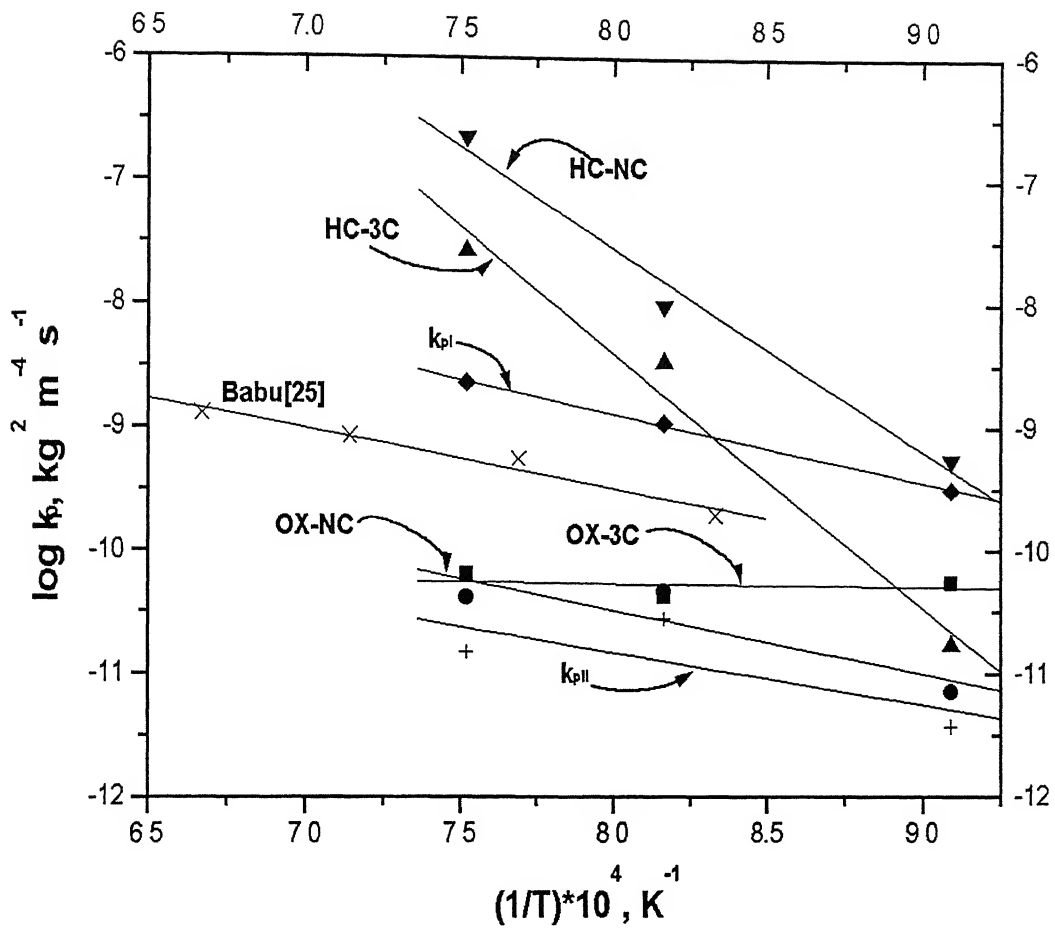


Figure 4.6 Variation of  $k_p$  with temperature for the oxidation and hot corrosion experiments for the NC and 3C alloys. In the case of oxidation of NC, the  $k_{pI}$  and  $k_{pII}$  have also been presented as a function of temperature. OX denotes oxidation and HC denotes hot corrosion experiments. The oxidation kinetics of  $\text{Fe}_3\text{Al}$  determined by continuous weight gain measurements by Babu [25] has also been indicated.

## 4.3 Characterization of Scales

As mentioned in Chapter 3, the scales on the surface of the specimens were visually observed initially. The surfaces of the samples were also analyzed by X-ray diffraction to determine the nature of the phases present in the scale. Some surface scales were also analyzed by FTIR spectroscopy. Finally, the scale topological morphologies will be discussed in this section.

### 4.3.1 Visual Observation of the Scales

The results of the scale characterization by unaided eye, XRD and FTIR are summarized in Table 4.4. The color of scales on all oxidized NC specimens were mostly creamish white, except the one at 1100K for which case the colour was dull white. The scales in all the above cases (except the one at 1100K) spalled as loose powdery form. The scales on the oxidized 3C specimens were mostly greyish in colour with some bright specks distributed throughout the sample surface. In this case also the scale spalling occurred in the form of loose fine powder, which were mostly of whitish colour.

Severe scale spalling was noted for the hot corroded samples, mainly at the two higher temperatures (1330K and 1225K). It is to be noted that  $\text{Na}_2\text{SO}_4$  is molten at those temperatures. The melting point of  $\text{Na}_2\text{SO}_4$  is 884°C [30]. At the lower temperature of hot corrosion, i.e. at 1100K, the salt remains solid and came out as a loose dry mass. In this case the surface of the samples turned dull brownish, the intensity of which gradually deepened with time for both the 3C and NC samples. At the higher temperatures of 1225K and 1330K there was severe scale spallation, which was observed from the initial stages of the experiment. The color of the spalled scale was mostly deep brown. The sample surface (from where the scale has spalled off) was in all cases covered by a white layer of loose scales.

### 4.3.2 X-ray Diffraction

The original XRD patterns obtained from the oxidized and hot corroded surfaces are presented in Appendix B. The diffraction patterns were analyzed utilizing standard JCPDS files [41]. The phases identified by XRD are tabulated in Table 4.4. The JCPDS files of the identified phases are also attached at the end of Appendix B. It is to be noted

that the phases whose diffraction intensities were significant were termed as the major phase and the phases from which the diffraction intensities were not significant were termed as the minor phases. This is reasonable as XRD intensities reflect the weighted average of the phases present, especially from multi-grained substances.

Analysis of the diffraction patterns of all the specimens after oxidation revealed  $\theta\text{-Al}_2\text{O}_3$  formed on the surface at the lowest temperature of oxidation. At the intermediate temperature  $\alpha\text{-Al}_2\text{O}_3$  was present in addition to  $\theta\text{-Al}_2\text{O}_3$ , with the former being the major phase. At the highest temperature the only constituent of the scale was  $\alpha\text{-Al}_2\text{O}_3$ . In addition to the peaks from the oxide, matrix peaks were also observed in some cases. This indicates that the scale was relatively thin as X-ray was able to penetrate the oxide layer.

In case of hot corrosion specimens the alumina phases appeared similar to that observed for the oxidation experiments. Interestingly, peaks corresponding to  $\alpha\text{-Fe}_2\text{O}_3$  were identifiable at the higher temperatures of 1225K and 1330K in the case of hot corrosion samples for both the alloys.

It is also interesting to note that the nature of scales observed were similar in both the alloys indicating that quite similar mechanisms operated in both. This indicates that the carbides in the carbon-alloyed iron aluminides did not significantly alter the surface sensitive properties like oxidation. Both the alloys contained Al in excess of that required for complete external oxidation and therefore the oxide covering the surface of both the alloys was primarily  $\text{Al}_2\text{O}_3$  in the case of oxidation, which appears to have been modified during hot corrosion. Therefore the role of carbides in lowering the rates of oxidation and hot corrosion (Table 4.1) must be related to features not directly concerning the nature of the surface layer. No other oxides could be resolved from the patterns. This implies that, if any other oxides were present, they may be present in trace amounts or in the amorphous form or both.

#### 4.3.3 FTIR Spectroscopy

The analysis of the spalled scales in the case of hot corrosion experiments was performed by FTIR. Some oxidized specimens were subjected to FTIR study to observe the nature of peaks formed after oxidation. The scales that were observed in by FTIR

spectroscopy were spalled in the initial stages of hot corrosion. In the four hot corrosion specimens (NC and 3C hot corroded at 1225K and 1330K) for which FTIR spectra were obtained, the features were quite similar. The broad peak between  $1050\text{ cm}^{-1}$  and  $1150\text{ cm}^{-1}$  results obtained from some sulphate phase, as most of the sulphate phases provide peaks in this range. In some cases, two distinct peaks (doublet) could be determined ( $1135\text{-}30\text{ cm}^{-1}$  and  $1116\text{-}1095\text{ cm}^{-1}$ ) which characterize  $\text{Na}_2\text{SO}_4$ . Therefore, it is reasonable to conclude that  $\text{Na}_2\text{SO}_4$  constituted one of the major constituents of the scale that spalled off during the initial stages of oxidation. Apart from this, the presence of  $\alpha\text{-Fe}_2\text{O}_3$  was indicated by the presence of peak at  $550\text{ cm}^{-1}$  and the presence of  $\alpha\text{-Al}_2\text{O}_3$  was indicated by the presence of peak between  $600\text{-}575\text{ cm}^{-1}$ . The FTIR spectra from the oxidation specimens indicated that only  $\text{Al}_2\text{O}_3$  was present, as found out earlier by Babu [25]. The details of the peak identified from FTIR study is illustrated in Table 4.5 for the different experiments. The original FTIR plots are provided in Appendix C. Interestingly, the phase  $\gamma\text{-FeOOH}$  was identified from the surface of the oxidized specimens and this is not a high temperature oxidation product, but rather a room temperature aqueous corrosion product. The specimen for the FTIR spectrum was taken nearly 3 months after the completion of the oxidation experiments and it is likely that some exposed portion of the surface has been corroded in the atmosphere during handling and storage.

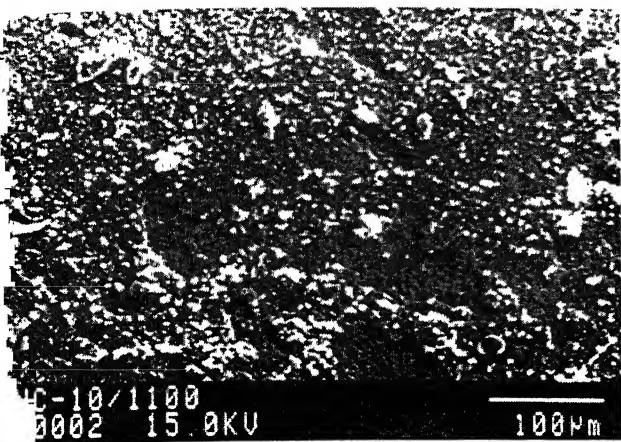
## 4.3.4 Scale Surface Morphology

### 4.3.4.1 Oxidation

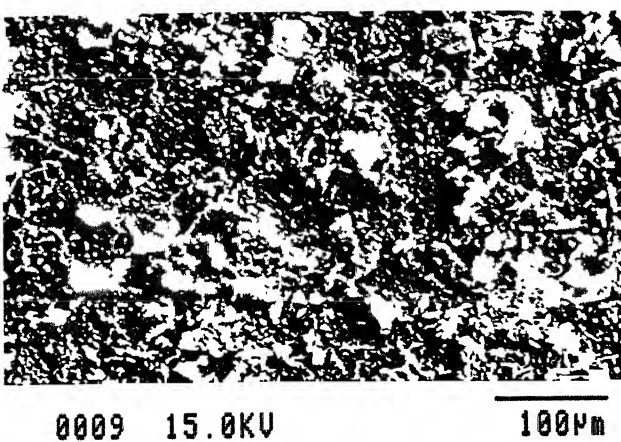
The surface scale morphologies observed at the end of the experiment are presented below. First, the oxidation specimens would be discussed and later, the hot corrosion specimens. Although the topological observations were conducted at several different magnifications, the SEM micrographs taken at 200X and 500X would be presented for all the cases, so that comparisons can be easily made.

In the case of oxidation, the morphologies for NC alloy are presented in Figure 4.7 while that for 3C in Figure 4.8. It can be seen from the SEM photographs, that for the alloy NC at the lower temperature i.e. 1100K, the surface is sparsely distributed with the oxides, which are of mainly triangular in shape. In comparison the oxide formed at the next higher temperature possesses a ridge-like morphology. At the highest temperature the surface is covered with ridges indicative of the familiar structure of  $\alpha\text{-Al}_2\text{O}_3$ . It can be also seen in case of the oxidized sample at 1100K that there, a part of the oxide has spalled off due to cracking. The cracks are also visible. In addition, the layered nature of the scale must also be noted.

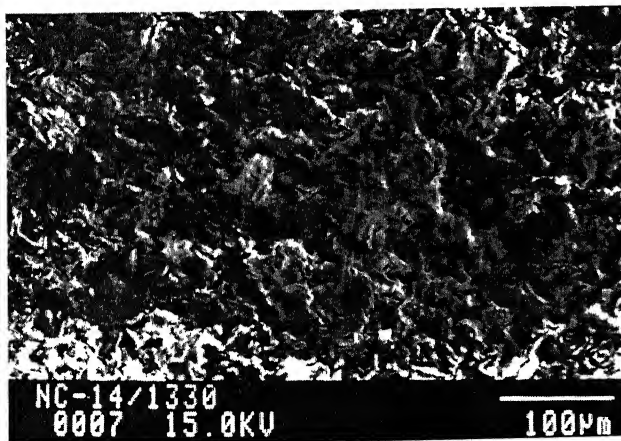
For the oxidation of the alloy 3C, it is seen from the SEM features that there is no particular morphology, at the lowest temperature. At the higher temperatures of 1225K and 1330K, however the development of ridge-like morphology may be discerned. Generally the surface oxide covered the surface completely in the case of the NC alloy as compared to the 3C alloy. On closer observation, it was determined that these regions not covered with oxides, in the 3C alloy, contained the carbide precipitates in those regions. One such carbide precipitate that is not covered with oxide is marked in Figure 4.8(b) as A. On the other hand, the oxide covers the entire surface in the case of alloy NC (Figure 4.7). The rhombohedral symmetry of the alumina that forms is reflected in the surface morphologies of the scale (triangular appearing oxides).



(a)



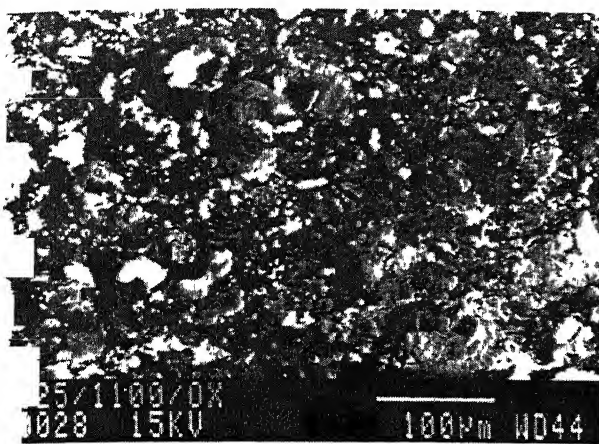
(b)



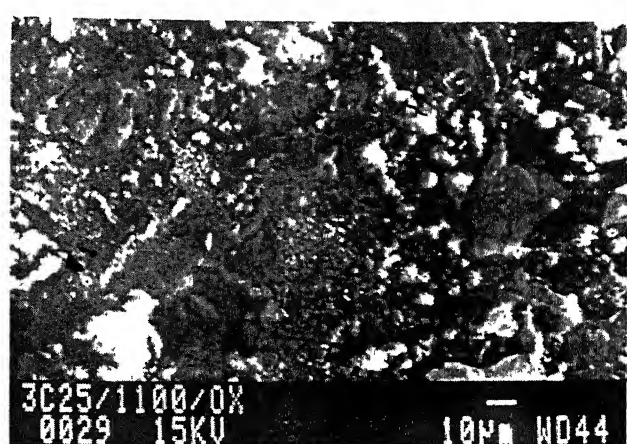
(c)



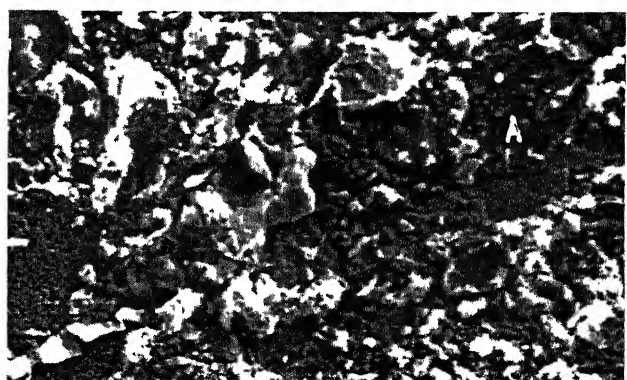
Figure 4.7 SEM morphologies of the oxide scales of the alloy NC oxidized for 65hrs at  
(a) 1100K, (b) 1225 and (c) 1330K.



(a)



(b)



(c)

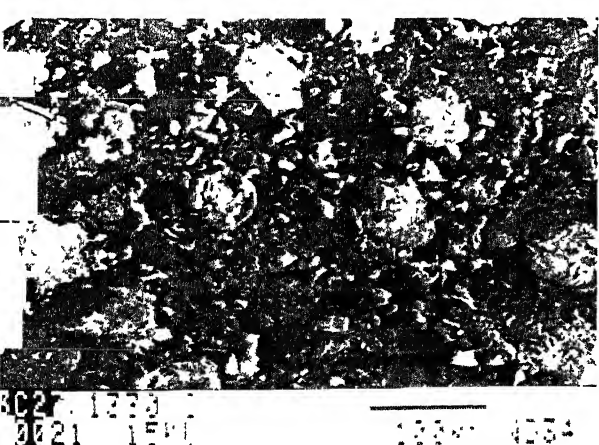


Figure 4.8 SEM morphologies of the oxide scales of the alloy 3C oxidized for 65hrs at (a) 1100K, (b) 1225 and (c) 1330K.

#### 4.3.4.2 Hot Corrosion

In the case of the hot corroded samples, the surfaces appeared brownish compared to the oxidized specimens, thereby indicating the possible change in the nature of the scale. SEM morphological observations revealed the scale topology to be different in the case of the hot corroded samples, with the difference most evident after higher temperature hot corrosion. Generally, the NC specimens exhibited a much more uniform coverage of the surface with scales compared to the 3C samples. The SEM morphologies are presented in Figure 4.9 for NC after hot corrosion and in Figure 4.10 for 3C after hot corrosion.

In the case of the NC specimen, the surface morphology of the scales were nodular at 1100K (Figure 4.9a), while the ridge-like morphology could be discerned after 1225K hot corrosion (Figure 4.9b). However, after hot corrosion at 1330K, the surface exhibited large nodule-like features while the space in between were covered with fine whisker-like morphology. The fine whisker-like morphology is again indicative of  $\alpha$ -Al<sub>2</sub>O<sub>3</sub> and the magnified view is shown in Figure 4.11 (a) (high magnified view of whisker). It is to be noted that the feature inside the nodule (Figure 4.11b) is different from the whisker morphology seen on the periphery of the nodules. EPMA analysis of the whisker-like region confirmed Al<sub>2</sub>O<sub>3</sub>. Therefore, the morphology of  $\alpha$ -Al<sub>2</sub>O<sub>3</sub> formed in the hot corrosion specimen after 1330K is quite different from that after simple oxidation at 1330K (comparing Figure 4.7c and 4.9c). This must be related to the process by which hot corrosion had occurred and further discussions would be taken up later.

In the case of the 3C samples it is seen from Figure 4.10 that most of the surface scales have spalled off at the higher temperatures. Distinct changes in the morphology could not be discerned. However, the surface was not completely covered with the oxide/layer. Some of these areas could be related to the presence of carbides.

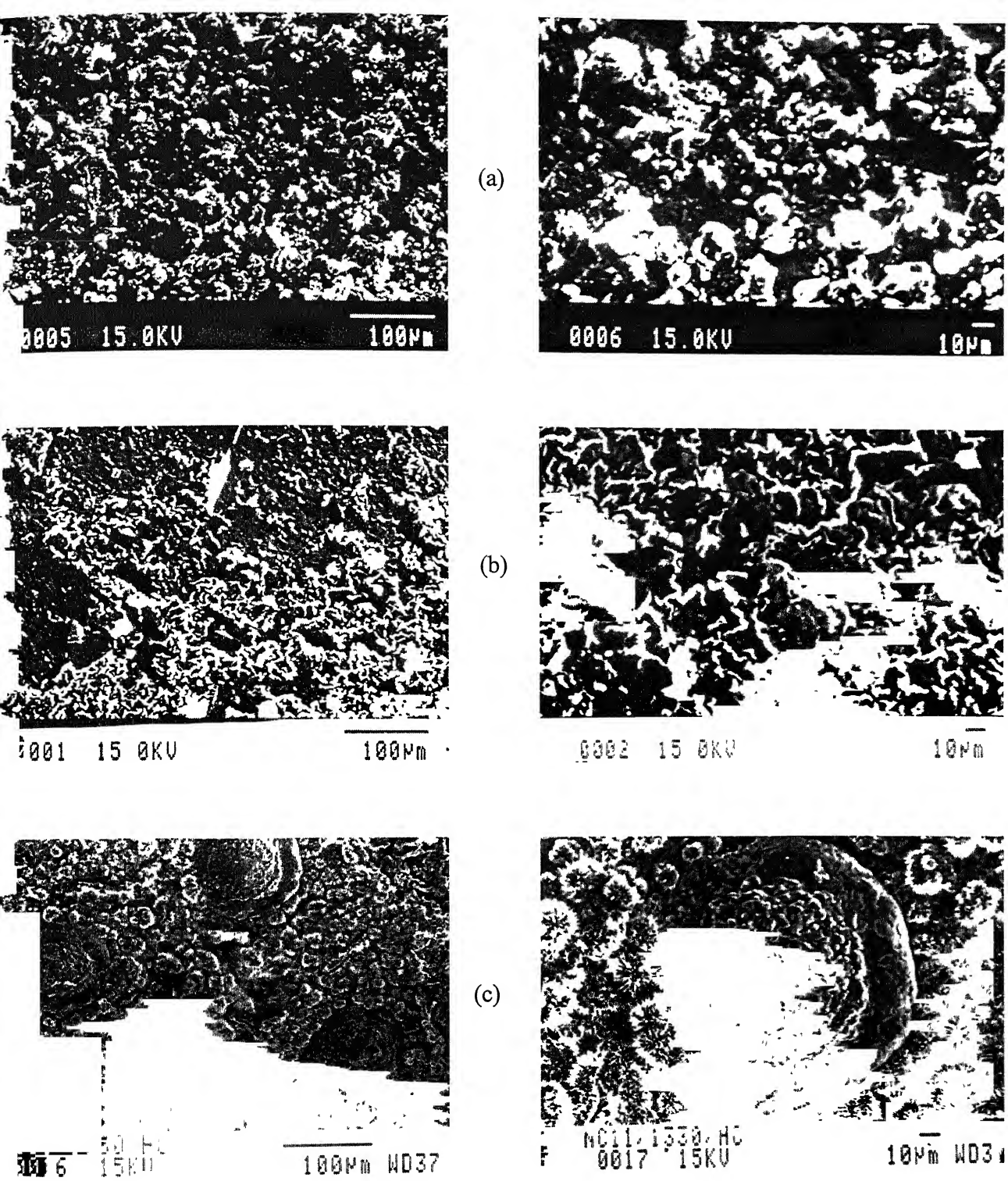
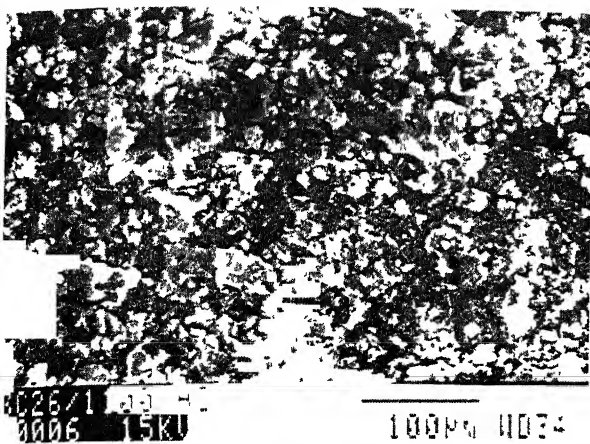
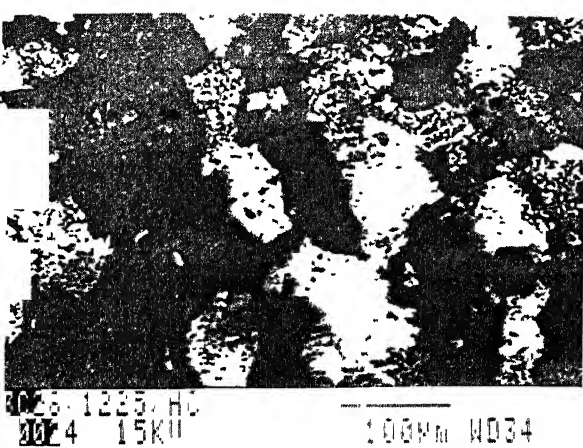
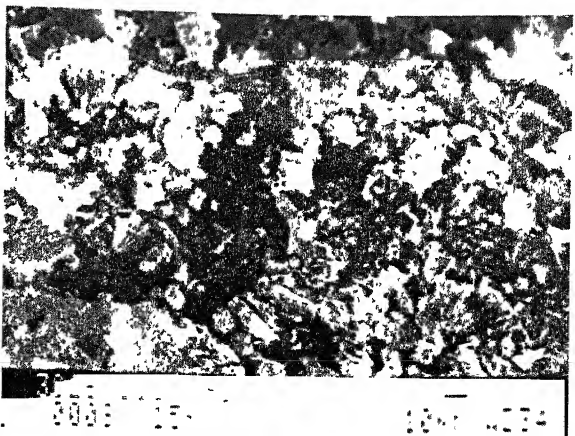


Figure 4.9 SEM morphologies of the alloy NC hot corroded for 65hrs at (a) 1100K, (b) 1225 and (c) 1330K.



(a)



(b)



(c)

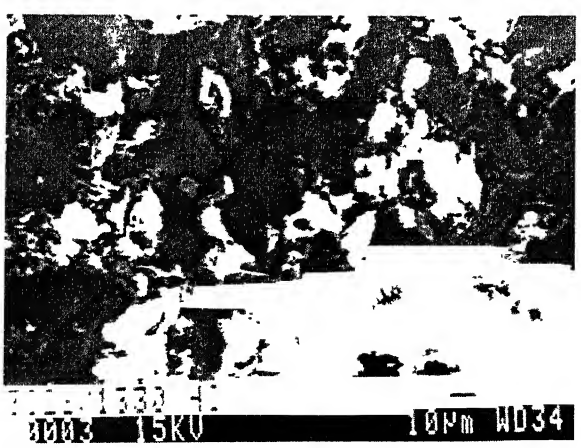
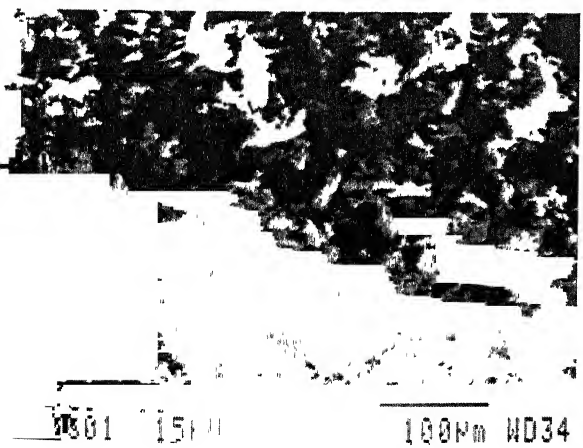
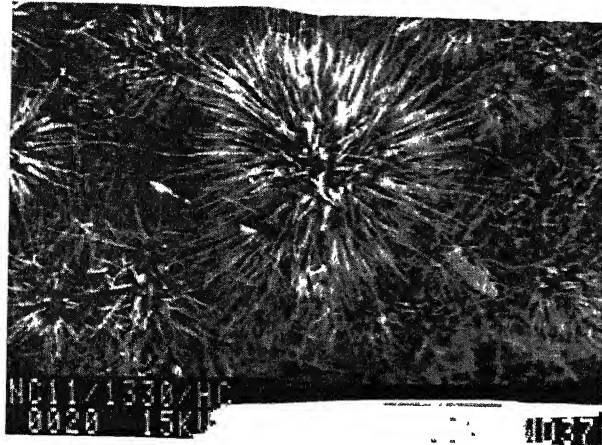
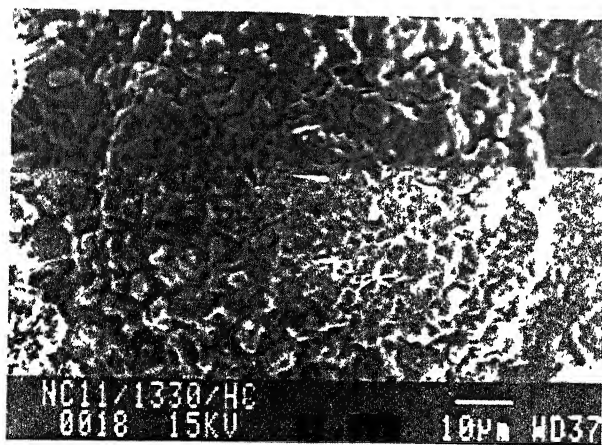


Figure 4.10 SEM morphologies of the alloy 3C hot corroded for 65hrs at (a) 1100K, (b) 1225 and (c) 1330K.



(a)



(b)

Figure 4.11 SEM morphologies of the alloy NC hot corroded for 65hrs at 1330K. (a) Depicts the whisker-like morphology of the oxide at the periphery, and (b) shows the nodular nature of the oxide at the centre.

# **Chapter 5**

## **DISCUSSIONS**

In the present chapter, the results obtained in the study would be discussed in detail. The kinetics of oxidation and hot corrosion would be co-related with the structural observations. Explanations for understanding the observed behaviour would be sought from earlier published literature on oxidation of iron aluminides as well as literature on oxidation and hot corrosion.

### **5.1 Oxidation Behavior**

The oxidation experiments revealed two interesting results. First, the oxidation rate of NC was greater than the 3C alloy. Secondly, the analysis of the oxidation data indicated that the NC alloy exhibited two kinds of parabolic behaviour, one in the earlier stages of oxidation and the other in the later stages of oxidation. The probable reasons for these observations would be addressed in greater detail below.

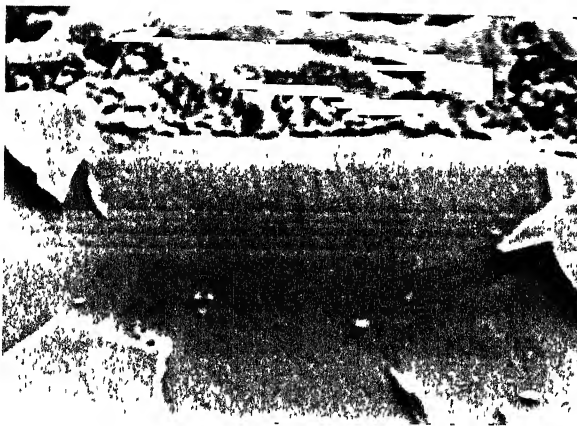
#### **5.1.1 Comparison of NC and 3C alloys**

Both the NC and 3C alloys contain sufficient Al for formation of a complete external layer of  $\text{Al}_2\text{O}_3$ . Therefore, the scales forming on the surfaces of these intermetallics are of alumina. There would not be any formation of iron oxides under the oxidation conditions utilized in this study, i.e. oxygen at 1 atm. pressure, because alumina is much more stable than iron oxides [42]. This has also been confirmed by scale characterization using XRD in the present study (Table 4.4). This is also in conformity with published literature on oxidation of iron aluminides [10, 17, 26]. Only alumina was identified on the surfaces of both the intermetallics during high temperature oxidation in pure oxygen environment. Slower oxidation kinetics was observed for the 3C alloy, at all the three temperatures, compared to the NC alloy. The slower kinetics implies a smaller weight gain and a lower amount of alumina covering the surface in the case of the 3C alloy. Topological observations of the scales using the SEM revealed that the surface

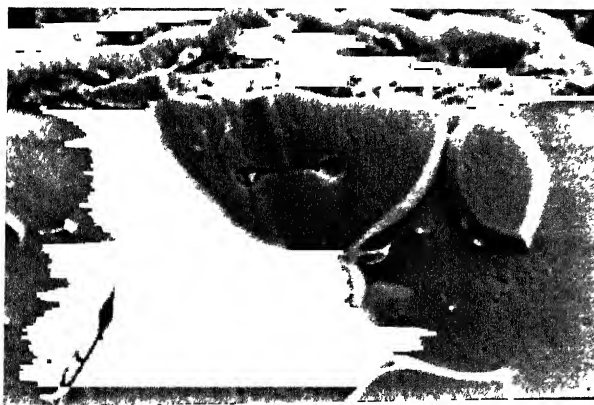
oxide covered the surface more completely in the case of the NC alloy whereas in the case of the 3C alloy, there were several locations where the oxide did not cover the surface. In these locations, the presence of the carbides could be discerned (Figure 4.7). The presence of carbides in the carbon-alloyed iron aluminides has resulted in a lower amount of alumina forming on the surface, which must be related to the relative area of carbides exposed to the environment on the surface.

The lower rate of oxidation of the carbon-alloyed intermetallic indicates that the carbide is stable at the temperatures of oxidation. Further, the nature of weight gain changes reveals, that the carbide should oxidize at a lower rate than the base iron aluminide because, otherwise, the rate of oxidation would have been higher for the carbon-alloyed iron aluminides. There is no literature on the oxidation behaviour of the carbides that are present in the carbon-alloyed intermetallic, namely  $\text{Fe}_3\text{AlC}_{0.5}$ . Interestingly, the behavior of the carbon-alloyed iron aluminides appears to be different when compared to the effect of carbides on the oxidation of Fe-Al-C alloys [22, 27, 28]. In the Fe-Al-C alloys investigated, the aluminium contents were much lower (5-8%) and complete alumina formation was not observed. The preferential oxidation of Fe in these Fe-Al-C alloys provided higher oxidation rates compared to the Fe-Al alloys without C. In order to check the stability of the carbides in the carbon-alloyed intermetallic and also to determine if the carbide preferentially oxidized with respect to the matrix, the 3C specimen oxidized at 1330K (i.e. the 3C specimen that exhibited the highest weight gain) was provided a electroless Ni coating and the sample was mounted on the cross section. The cross section of the sample was metallographically prepared and observed in the EPMA. A typical cross-sectional micrograph is provided in Figure 5.1(a), where the Ni coating can be seen on top of the oxide layer. The oxide layer was analyzed and it was composed of only alumina. It is interesting to note the effect of oxidation on the nature of the carbide. It can be seen that there is no preferential attack along the carbide-matrix interfaces. Moreover, the carbides appear to be more resistant to oxidation compared to the matrix as the carbide in the top left corner of the Figure 5.1(a) appeared to be oxidized to a lower extent compared to the matrix, i.e. the carbide can be seen projecting into the oxide. The stable nature of the carbide was also revealed in observations at

several other oxide-substrate locations in the same sample and another such example is shown in Figure 5.1 (b).



(a)



(b)

Figure 5.1 SEM morphologies of the cross-sectional features of the alloy 3C oxidized at 1330K for 65hrs

Cross sectional microscopy coupled with the surface topological observations, therefore revealed that the oxidation of the carbide was not detrimental to the oxidation resistance of the carbon-alloyed iron aluminide. The lower rate of the oxidation in the carbon-alloyed intermetallic could result due to the carbides acting like blocking sites for the oxidation process. On the other hand, the base iron aluminide oxidized uniformly throughout the surface.

### 5.1.2 Transitional Alumina Formation

The second interesting observation in the oxidation experiments was that the oxidation kinetics of the NC alloy could be analyzed with two distinct parabolic behaviors. The parabolic rate constant in the initial stages of oxidation was higher than in the later stages of oxidation. The two regions were well distinguished on the parabolic plots of the weight gain data (Figure 4.1). It was earlier pointed by Grabke *et al* [35] that the kinetics of oxidation of iron aluminides could be analyzed as consisting of two regions of parabolic behavior, with the two regions corresponding to the formation of different kinds of aluminas. For example, the faster initial oxidation kinetics was related by Grabke *et al* to transition  $\theta\text{-Al}_2\text{O}_3$  formation while the lower oxidation kinetics in the later stages was related to  $\alpha\text{-Al}_2\text{O}_3$  formation. In order to gain further insights into the possible relationship of the kinetics with the nature of alumina formed, the kinetics of the two stages are compared to  $\alpha$  and  $\theta\text{-Al}_2\text{O}_3$  formation kinetics. The data for these kinetics have been reported for the case NiAl by Rybicki *et al* [23] and for FeAl by Smialek *et al* [34] and Grabke *et al* [35], and all these have been provided in Figure 5.2. All the available literature on the kinetics of  $\theta\text{-Al}_2\text{O}_3$  and  $\alpha\text{-Al}_2\text{O}_3$  formation has been presented in this figure.

It can be noticed from this figure that the initial rate observed in this investigation could be related to  $\theta\text{-Al}_2\text{O}_3$  formation kinetics while the rate from the later stages of oxidation can be related to  $\alpha\text{-Al}_2\text{O}_3$  formation kinetics. It is also interesting to note that the slopes of these lines for the initial and final stages of oxidation is similar to the overall rate and similar to the slope of the oxidation kinetics determined by Babu for Fe-25Al over a range of temperatures [25]. The data for Babu were obtained by continuous

weight gain measurements in a Cahn balance, while the present measurements were obtained by intermittent methods.

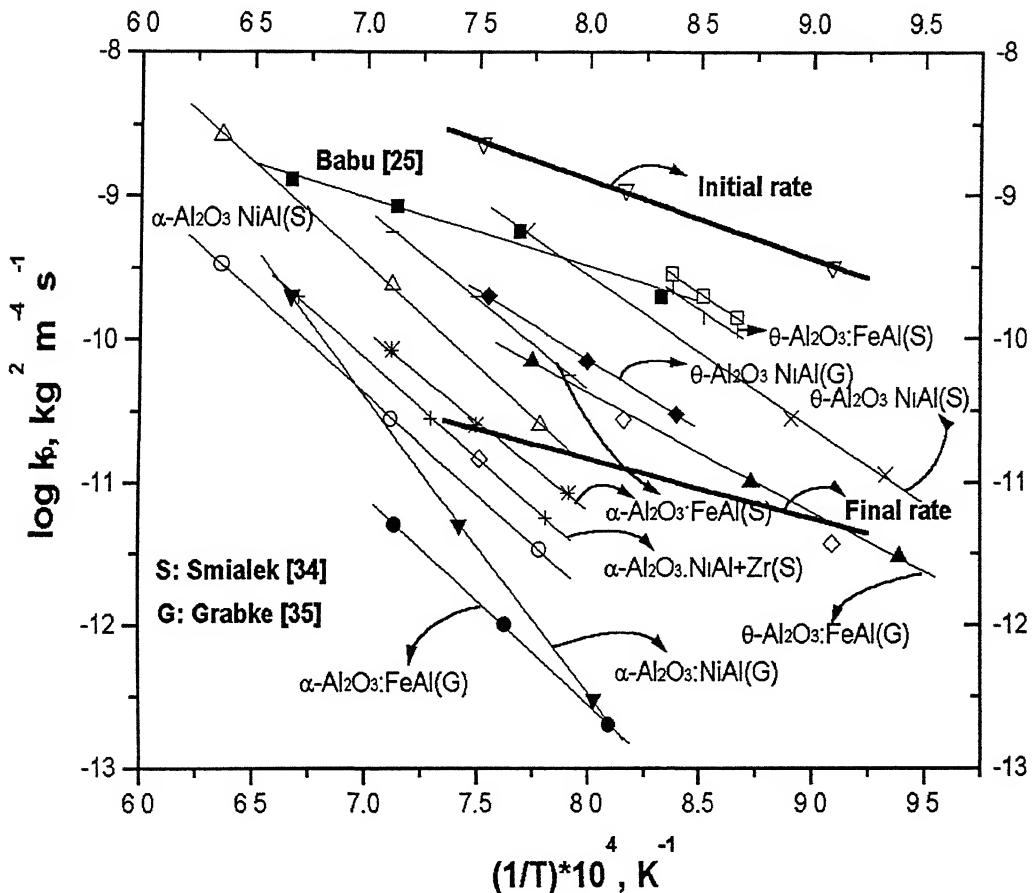


Figure 5.2 Literature data for kinetics of  $\alpha$ - and  $\theta\text{-Al}_2\text{O}_3$  formation. The oxidation rate in the initial and final periods for the alloy NC has been provided.

The analysis of the weight gain data obtained by grouping them into two regions is justified in the present case because XRD results clearly revealed that two types of alumina form in the oxidation. The scale nature was determined using XRD based on the remaining oxide on the surface. It must be pointed out that the variation in oxide

formation as a function of oxidation time was not determined, due to scale spallation. The scale nature identified at the end of the experiments need not match the scale nature throughout the course of the experiment. While the major alumina phase identified at the lowest temperature was  $\theta\text{-Al}_2\text{O}_3$ , the major alumina phase determined by XRD was  $\alpha\text{-Al}_2\text{O}_3$  at higher temperatures. It was earlier reviewed in the literature review section that the transitional alumina ( $\theta\text{-Al}_2\text{O}_3$ ) forms first and later transforms to  $\alpha\text{-Al}_2\text{O}_3$  and this occurs more readily at higher temperatures [18, 20]. Therefore, the presence of  $\theta\text{-Al}_2\text{O}_3$  on the surface after long oxidation times is more likely at lower oxidation temperatures.

There is a great degree of correlation with morphological observations in the present case and that of literature. It has been seen before [23, 34] that the morphology of the alumina formed at a lower temperature is whisker-like, which is typical of  $\theta\text{-Al}_2\text{O}_3$ , while the alumina formed at a higher temperature has a ridge-like morphology, which is associated with  $\alpha\text{-Al}_2\text{O}_3$ . There is a close similarity of the observed morphology with that observed in the literature for the different types of aluminas.

## 5.2 Hot Corrosion Behavior

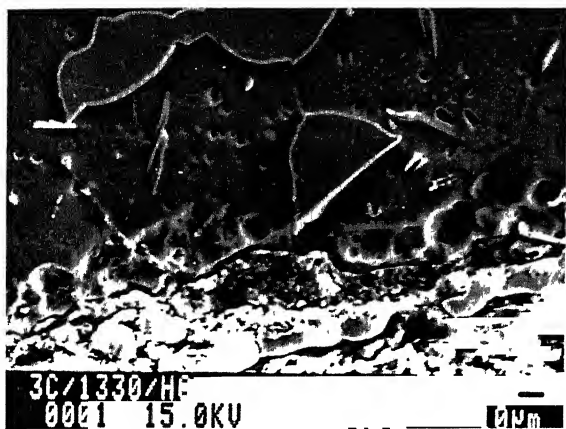
The present study is one of the few studies on the hot corrosion of binary iron aluminides at high temperatures using  $\text{Na}_2\text{SO}_4$  melts in pure oxygen. Therefore, there is no established yardstick that can be used for comparison. It is with this in mind that the results obtained in the hot corrosion studies would be discussed.

The kinetic data indicated that the rate of hot corrosion was higher than oxidation for both the alloys. Moreover, the rate of hot corrosion of the alloy without carbon, namely NC, was higher than the carbon-alloyed intermetallic. The lower rate of hot corrosion in the case of the 3C alloy could be for the same reason as that noted for oxidation. The presence of carbides in the carbon-alloyed intermetallic would result in a lower amount of surface area of the base iron aluminide being exposed and therefore, the kinetics of attack should be lower. This assumes that the carbides present in the 3C alloy are not degraded to a greater extent than the base matrix. Topological observation of the surface scales after hot corrosion of these alloys indicated that a fairly thick scale covered the surface in the case of the NC alloy compared to the scales on the surface of the 3C

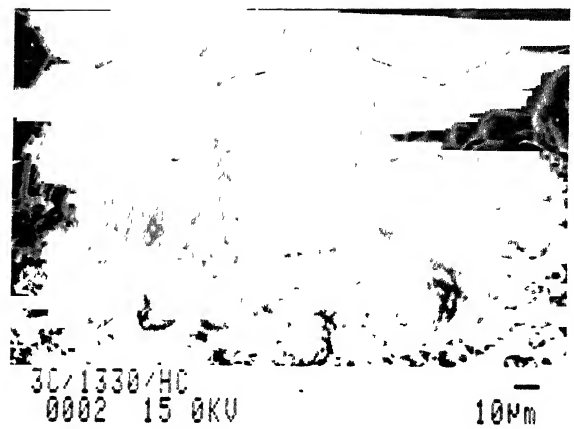
alloy. In order to gain further insights into the nature of material attack in the case of hot corrosion, cross sectional analysis of the alloys (after hot corrosion experiments at 1330K) was performed. The surface scales were initially coated with electroless Ni plating before mounting the samples. The cross sectional microstructure of the samples that were subjected to hot corrosion revealed several interesting features.

### 5.2.1 Cross Sectional Analysis of 3C Alloy

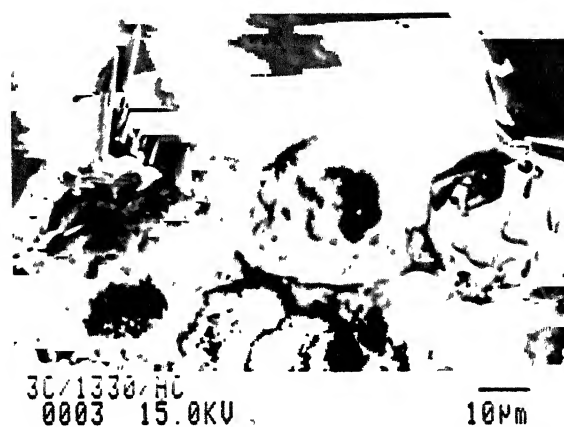
The thickness of the surface scale was much higher compared to the thickness of the scale in the case of only oxidation (comparing Figure 5.3 and Figure 5.1). Cross sectional microscopy of the 3C sample after hot corrosion at 1330K (Figure 5.3) revealed that the base metal was degraded in a characteristic fashion, especially at the scale-metal interface where deep pits could be observed at the interface. Observation of Figure 5.3(a) revealed further interesting details. The carbide particles in Figure 5.3(a) do not seem to be preferentially attacked. Some grain boundaries in Figure 5.3(b) have been penetrated by a white-appearing phase at the metal-scale interface. Corrosion products could be identified in the pits at the metal-scale interface Figure 5.3(c). A higher magnification view of these pit-like features of Figure 5.3(a) is provided in Figure 5.3(c), from which it can be noticed that there are remnants of reaction products within the pits. These features are also revealed in Figure 5.4(a). The corrosion product in one of the pits in Figure 5.4(b) was analyzed and the EPMA result is provided in Figure 5.5. The corrosion product contained Fe, Al, O and S. The EPMA result from another pit in Figure 5.4(c) is provided in Figure 5.6 from where it can be seen that it primarily contains more Fe, Al and O and a little amount of S. The EPMA results obtained from the scale in the same sample did not reveal S but composed of Al, Fe and O. A typical EPMA result from the external scale is provided in Figure 5.7. It is noticed that S is practically absent in the EPMA result of Figure 5.7. When viewed along with the XRD results, it can be concluded that the external scales must be  $\alpha\text{-Fe}_2\text{O}_3$  and  $\alpha\text{-Al}_2\text{O}_3$ . The corrosion products within the pits could be sulphates, sulphides or oxides or mixtures of these. It was interesting that S was identified in the reaction product at scale-metal interface as this indicates that sulphur-bearing compounds are found deeper within the scale than above.



(a)

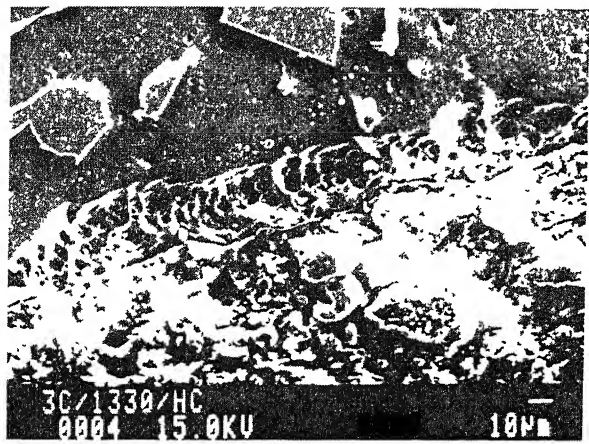


(b)

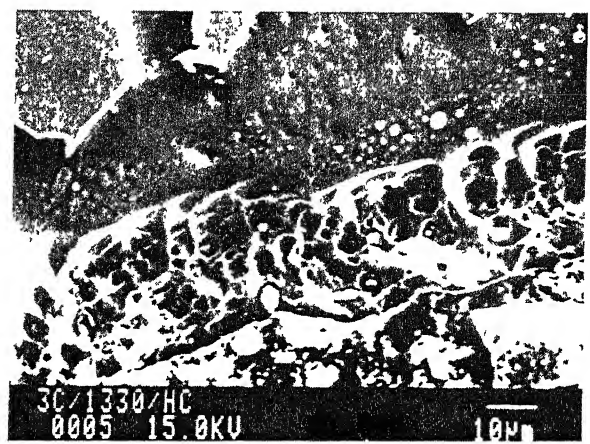


(c)

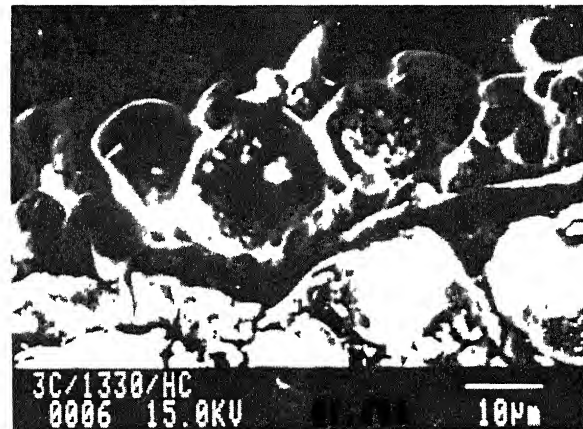
Figure 5.3 SEM morphologies of the cross-sectional features of the alloy 3C hot corroded at 1330K for 65hrs.



(a)



(b)



(c)

Figure 5.4 SEM morphologies of the cross-sectional features of the alloy 3C hot corroded at 1330K for 65hrs.

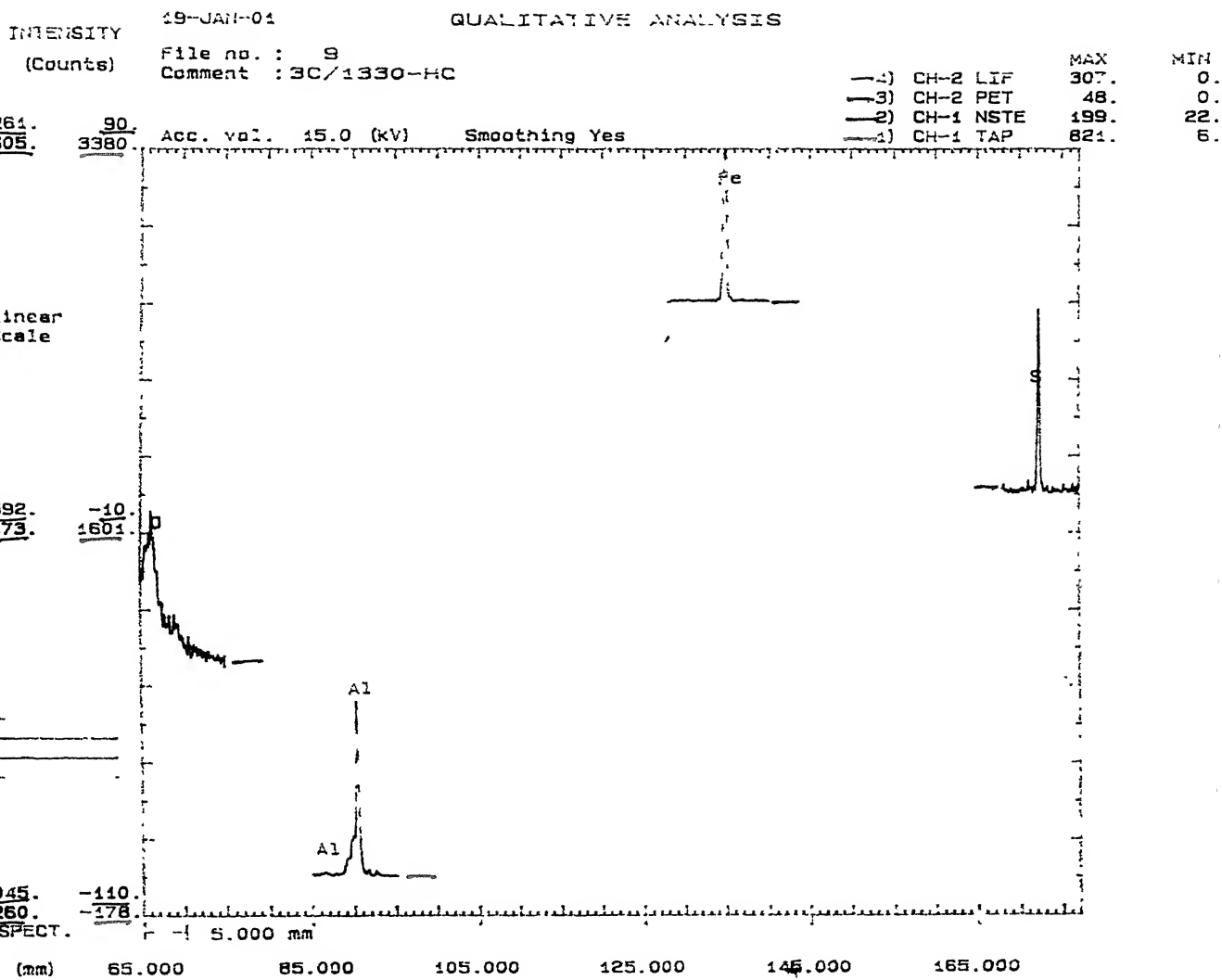


Figure 5.5 EPMA analysis of the corrosion product from the pit corresponding to the SEM micrograph Figure 5.4(b) of the alloy 3C hot corroded at 1330K for 65hrs.

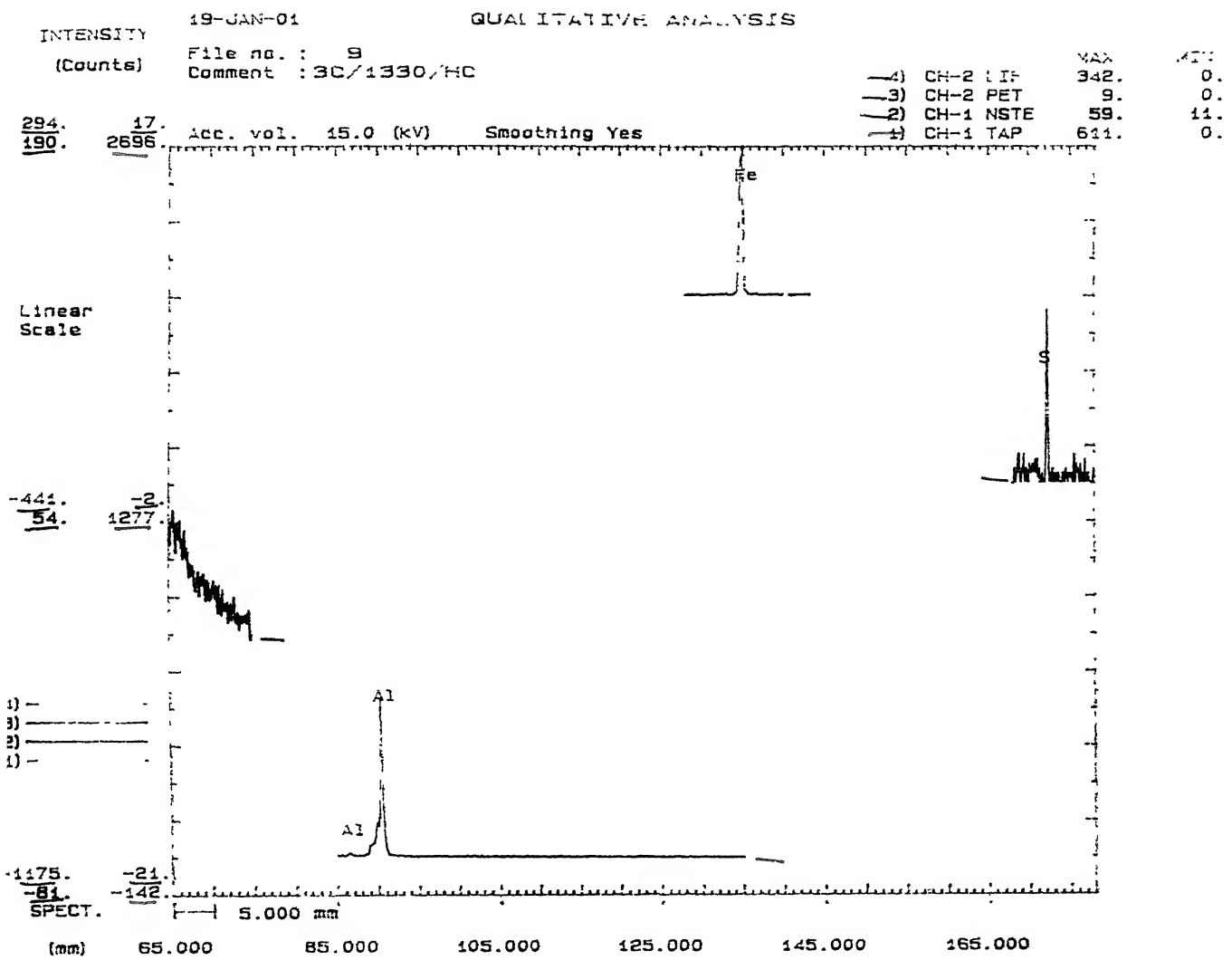


Figure 5.6 EPMA analysis of the corrosion product from the pit corresponding to the SEM micrograph Figure 5.4(c) of the alloy 3C hot corroded at 1330K for 65hrs.

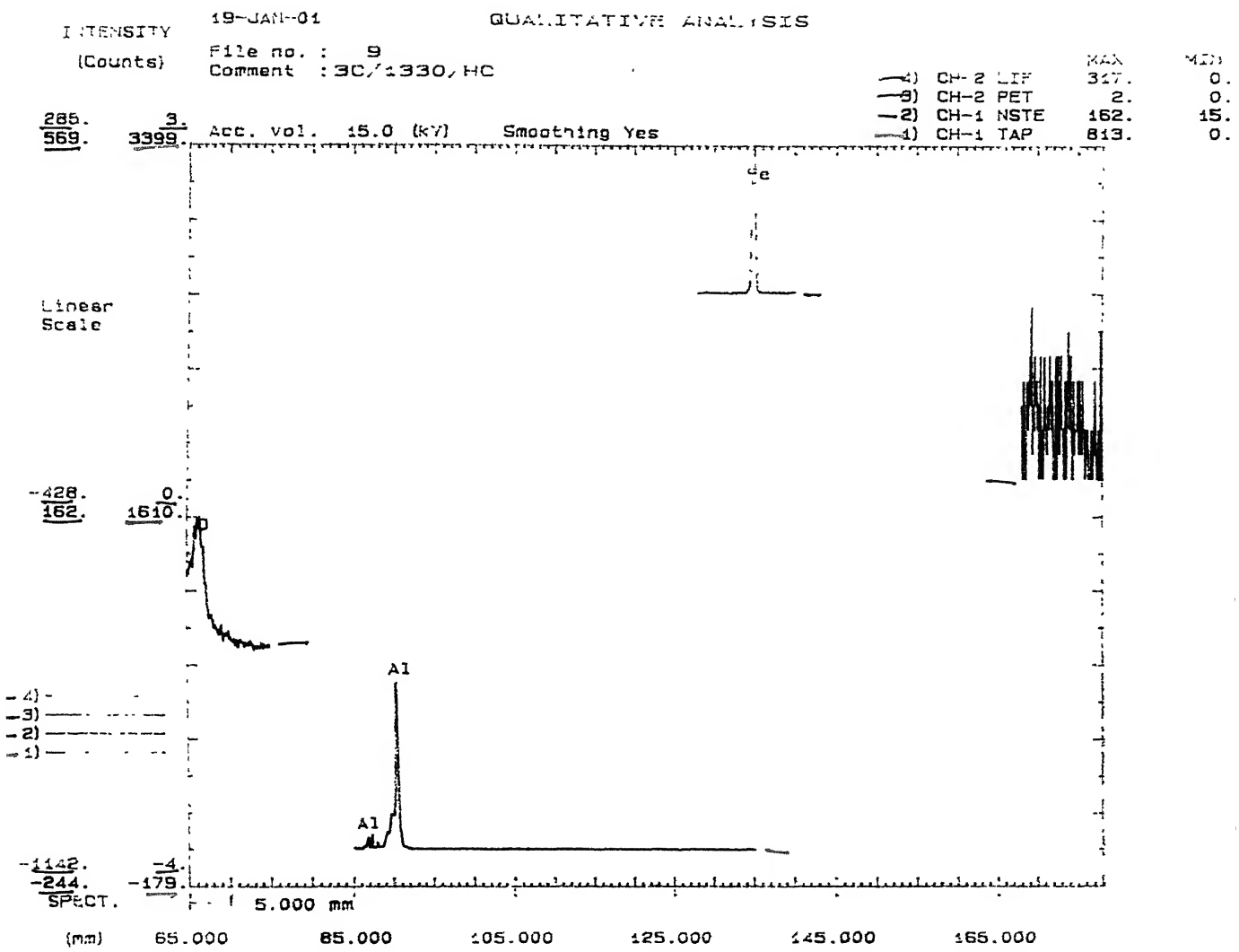
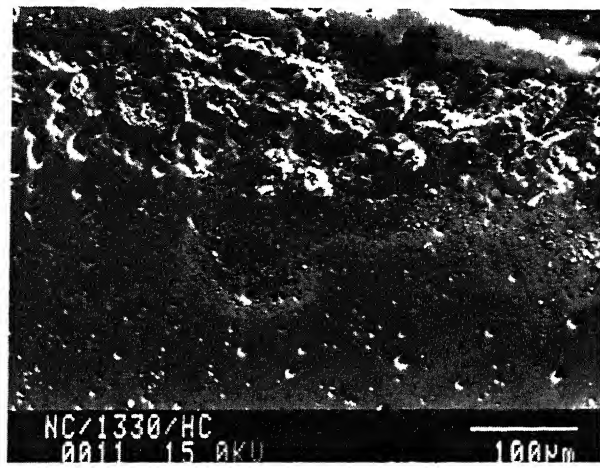


Figure 5.7 EPMA analysis of the external cross-sectional scale of the alloy 3C hot corroded at 1330K for 65hrs.

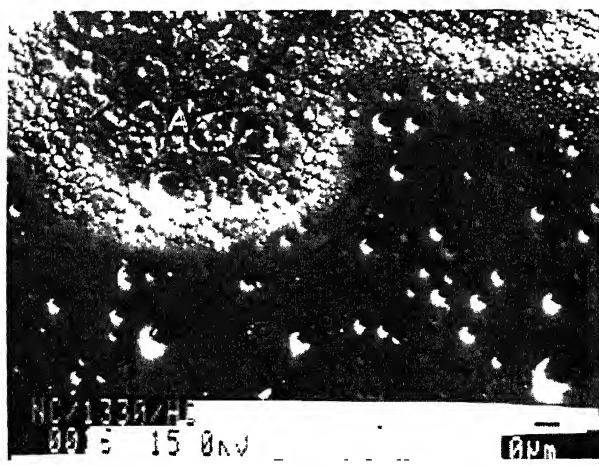
### 5.2.2 Cross Sectional Analysis of NC Alloy

As the kinetics of hot corrosion was faster in the case of the NC alloy compared to the 3C alloy, the cross section of the NC alloy after hot corrosion at 1330K was analyzed in the EPMA. Initially, the surface features observed in the topological picture of Figure 4.9(c) was analyzed. Qualitative EPMA analysis from the center of the nodules seen in Figure 4.9(c) provided that Al, Fe and O were present here, while the needle-like growth on the periphery of the nodules were analyzed as alumina. Therefore, there appeared to be different compositions based on the nature of the scale structure. The possible composition of the nodular-like structures could not be determined with any certainty, but it can be reasonably stated that the possible phases could be  $\text{Fe}_2\text{O}_3$  and  $\text{Al}_2\text{O}_3$ , on coupling with the XRD results. Relatively thick scales were observed in this alloy (Figure 5.8). As observed in Figure 5.8(a) a corrosion zone had penetrated the alloy in this location, a high magnification view of which is provided in Figure 5.8(b). The EPMA analysis from the corrosion product zone in Figure 5.8(b) at the location marked A is provided in Figure 5.9, and it is seen that the product consisted of essentially  $\text{Fe}_2\text{O}_3$  and  $\text{Al}_2\text{O}_3$ . The penetrating corrosion product zone was not consistently observed on all surfaces. On the other hand, the interface region between the metal and scale was pitted, quite similar to that observed for the 3C alloy. The nature of the pitted region can be gleaned from Figure 5.10(a) and (b). In Figure 5.10(a) the scale has spalled and the Ni coating is visible. Pits are present regularly along the surface. The most interesting aspect was that there were several grain boundaries where the pits were identifiable. A higher magnification view of the pits along grain boundary is provided in Figure 5.10(b). Most of the pits (even deep within the matrix) contained corrosion products. The corrosion product in the pit marked A in Figure 5.10(b) was analyzed by EPMA and the EPMA result is presented in Figure 5.11. The intensity of the Al and S peaks are much greater than the Fe and O peaks, indicating that the product in the pit is the sulphide  $\text{Al}_2\text{S}_3$ .

In order to understand the formation of this phase, the relatively thermodynamic stabilities of the possible reaction products are compared in Table 5.1. It can be seen that the formation of  $\text{Al}_2\text{S}_3$  is more likely than  $\text{FeS}$  based on thermodynamic considerations.



(a)



(b)

Figure 5.8 SEM morphologies of the cross-sectional features of the alloy NC hot corroded at 1330K for 65hrs.

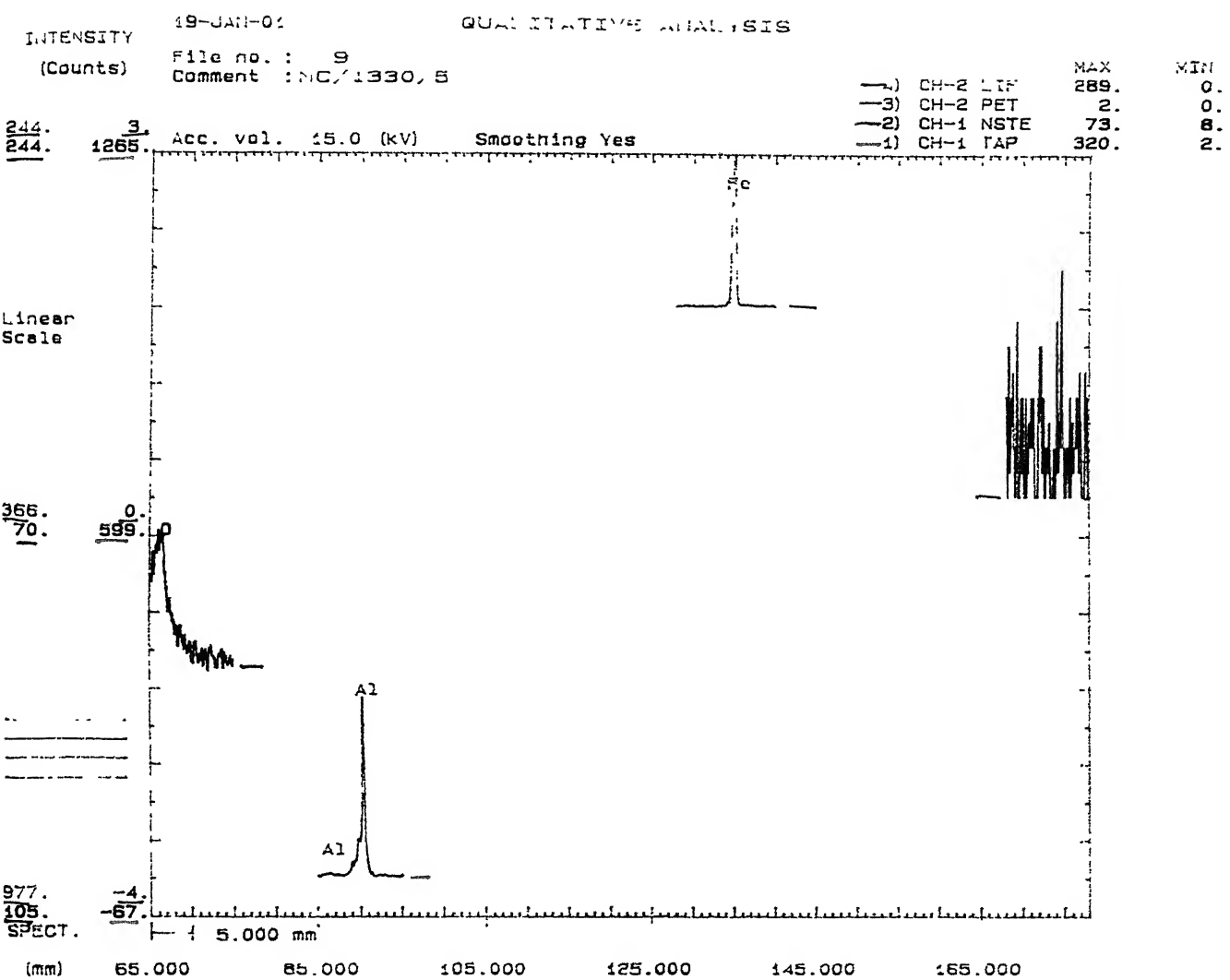
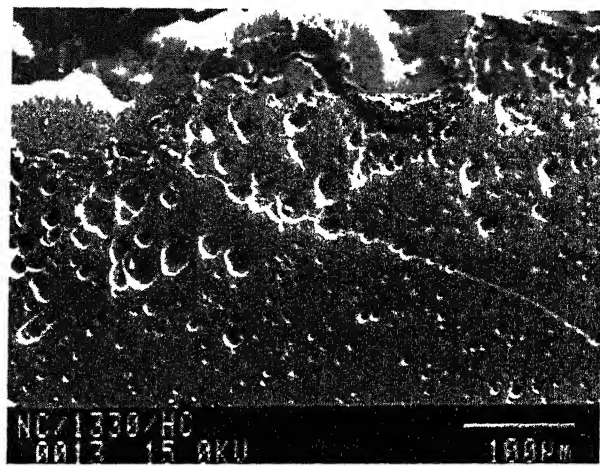
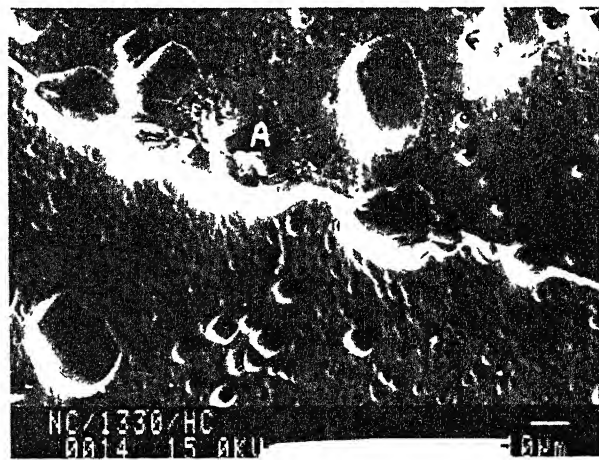


Figure 5.9 EPMA analysis of the corrosion product zone from the location marked A, corresponding to the SEM micrograph Figure 5.8(b) of the alloy NC hot corroded at 1330K for 65hrs.



(a)



(b)

Figure 5.10 SEM morphologies of the cross-sectional features of the alloy NC hot corroded at 1330K for 65hrs.

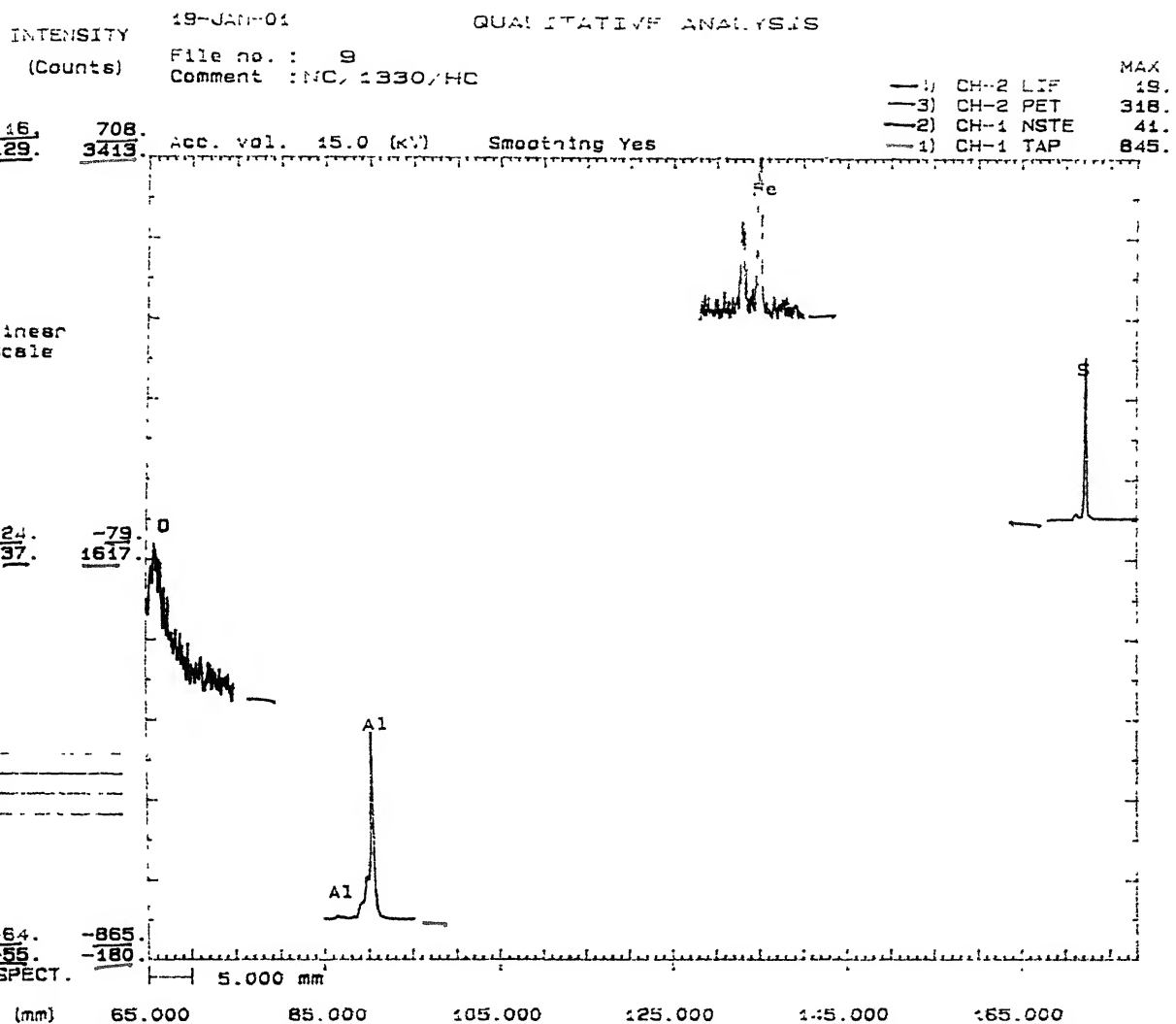


Figure 5.11 EPMA analysis of the corrosion product from the pit marked A, corresponding to the SEM micrograph Figure 5.10(b) of the alloy NC hot corroded at 1330K for 65hrs.

**Table 5.1 The free-energy ( $\Delta G$ ) values for the probable corrosion products [47]**

Compound	( $\Delta G$ ), (kcal/mol)	Compound	( $\Delta G$ ), (kcal/mol)
$\text{Al}_2\text{O}_3$	-111.83	$\text{Fe}_2\text{O}_3$	-1.74
$\text{Al}_2\text{S}_3$	-8.52	$\text{FeS}$	-2.35
$\text{Al}_2(\text{SO}_4)_3$	-42.10	$\text{FeSO}_4$	-5.15

### 5.2.3 Mechanism of Hot Corrosion

Based on the microstructural and compositional characterization of the 3C and NC alloy, the likely process of hot corrosion can be understood. One mechanism of hot corrosion in both the alloys appears to be similar based on the microstructural characterization of attack. However, before explaining the mechanism, it would be of interest to understand the hot corrosion process-taking place, using isothermal thermodynamic stability diagrams. Thermodynamic stability diagrams are useful for understanding the effects of deposit compositional changes. The stability diagrams along with microstructural analyses can be used to understand mechanisms of hot corrosion. These diagrams provide the regions of stable phases in the presence of more than one reaction non-metal species. In the present case, we have two reactive non-metallic component, S and O. As the main oxide former in the case of both the intermetallics is alumina, it is reasonable to address the stability diagram of the Al-O-S system. The isothermal stability diagram of Al-O-S at 900°C is provided in Figure 5.12. Only the region where  $\text{Na}_2\text{SO}_4$  is molten is addressed in the diagram. Therefore, the isothermal stability diagram provides insight into the reaction of the oxide layer with the molten  $\text{Na}_2\text{SO}_4$ .

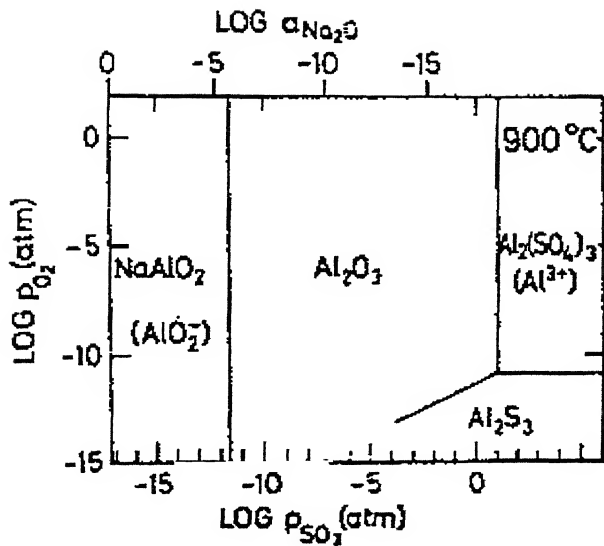


Figure 5.12 Phase stability diagram of  $\text{Al}_2\text{O}_3$  at 900°C in the stability region of  $\text{Na}_2\text{SO}_4$  (l).

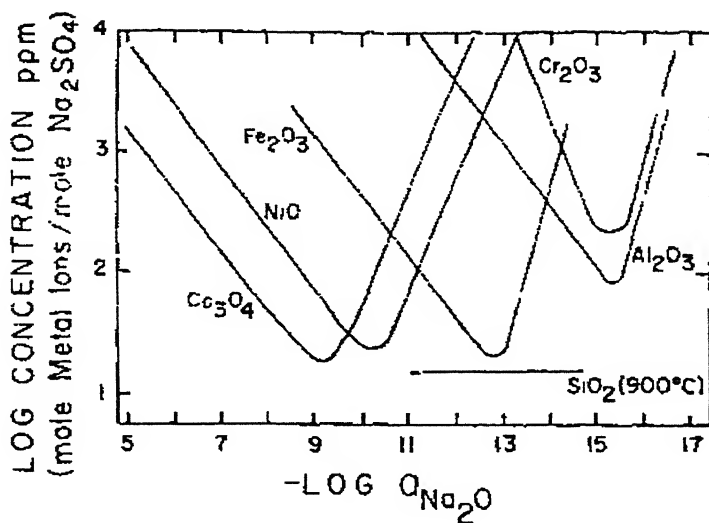
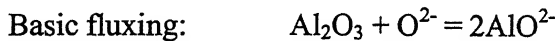
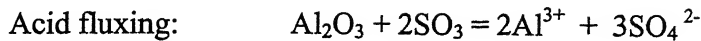


Figure 5.13 Measured oxide solubilities in fused  $\text{Na}_2\text{SO}_4$  at 927°C and 1atm  $\text{O}_2$  [43].

The solubility curves for a number of oxides in  $\text{Na}_2\text{SO}_4$  as a function of  $\text{SO}_3$  pressures is provided in Figure 5.13 [43]. Alumina, is amphoteric and this can be fluxed both in acidic and basic melts. The  $\text{Na}_2\text{SO}_4$  can be thought to compose of two

components acidic ( $\text{SO}_3$ ) and basic ( $\text{Na}_2\text{O}$ ) components. The alumina can react and dissolve in the melt according to:



In the case of  $\alpha\text{-Al}_2\text{O}_3$  at 1atm  $\text{O}_2$ , Jose *et al* [44] found the minimum in the solubility at  $\log a_{\text{Na}_2\text{O}} = -15.4$ . (At this value the  $\log p_{\text{SO}_3}$  is about  $-3$  atm). Therefore, alumina (like chromia) can suffer degradation due to both mechanisms of hot corrosion. It is difficult to firmly establish whether alumina is fluxed by the acid or basic fluxing mechanism initially. Nevertheless, certain points become apparent on analysis of kinetic data and FTIR data from spalled scales. When metal, like Ni, with  $\text{Na}_2\text{SO}_4$  deposits are reacted in oxygen or air (containing significant amounts of  $\text{SO}_3$ ), accelerated corrosion of Ni takes place only above the melting point of  $\text{Na}_2\text{SO}_4$  (above  $884^\circ\text{C}$ ) [45]. At lower temperature the salt deposit serves as a barrier to oxidation and may reduce the reaction rate compared to that of metal with no  $\text{Na}_2\text{SO}_4$  deposit [46]. This was observed for 3C alloy in the present study. The identification of  $\text{Fe}_2\text{O}_3$  in the spalled scales indicate that when the  $\text{Na}_2\text{SO}_4$  salt melts on the surface, non-protective conditions are established leading to oxidation of both Al and Fe. This must constitute the initiation stage of hot corrosion. Sustained, accelerated hot corrosion induced by  $\text{Na}_2\text{SO}_4$  appears to be associated with sulphide formation at or near the metal-scale interface. As for the reaction of the metal with  $\text{SO}_2$  or  $\text{SO}_2 + \text{O}_2$ , the sulphide phases in the scale provide a path for rapid outward diffusion of the metal. A notable feature of attack by this mechanism is the formation of pits.

An important aspect of hot corrosion appears to be the reduction in the partial pressure of oxygen with increasing depth of the scale. At the scale-metal interface location, the partial pressure of oxygen is very low (i.e. it is the dissociation pressure of oxygen with alumina at this temperature). Under such low partial pressures of oxygen, the sulphur activity is high. Under such high sulphur activity, it is envisaged that there would be formation of sulphides at the interface. It is likely that  $\text{FeS}$  can also form in addition to  $\text{Al}_2\text{S}_3$  in the locations near the metal-scale interface, whereas in locations deep

within the material along the grain boundaries, only the  $\text{Al}_2\text{S}_3$  sulphide forms as here the activity of S is very low and this would allow the precipitation of only the most stable sulphide, namely  $\text{Al}_2\text{S}_3$ . The oxidation of these sulphides at the metal-scale boundaries would lead to further penetration of the material by the sulphur which is liberated by the oxidation reaction and in this manner, the attack of the material is accelerated. It has, in fact, been found by cross sectional microscopy, that the attack of the material at the scale-metal boundary was indeed very significant (Figure 5.10a) and moreover, the diffusing S had penetrated deep into the material (Figure 5.10b). Therefore, in the propagation stage, the extensive sulphidation of especially Al, which is needed to form the protective oxide, will result in non-protective scale formation. The sulphur released after oxidation will further diffuse inside the material to cause further degradation.

The identification of  $\text{Fe}_2\text{O}_3$  in the scales after hot corrosion is very interesting. It is not possible for  $\text{Fe}_2\text{O}_3$  to form when Fe competes with Al to form the oxides, because the alloys contain sufficient Al to form a stable external scale in oxidizing environments and moreover, the free energy for formation of alumina is much lower than that for  $\text{Fe}_2\text{O}_3$  (Table 5.1). However, the free energies for formation of the sulphides  $\text{FeS}$  and  $\text{Al}_2\text{S}_3$  is not too different and therefore, it is likely that both the sulphides form in the material, especially at the metal-scale interface. The subsequent oxidation of  $\text{FeS}$  to  $\text{Fe}_2\text{O}_3$  would explain the identification of the  $\text{Fe}_2\text{O}_3$  phase in the remaining scales of the hot corroded samples. It is also interesting to note that the  $\text{Fe}_2\text{O}_3$  phase was not identified when the samples were hot corroded at the lower temperature, again indicating that the salt was not molten at this temperature. However, at the higher two temperatures, where the salt was molten, the phase  $\text{Fe}_2\text{O}_3$  was identified, thereby indicating that the oxide should have formed from the oxidation of  $\text{FeS}$ .

The hot corrosion rate was faster in the case of the NC alloy when compared to the 3C alloy. One possible reason for the same was explained above in that the carbides do not expose the matrix on the exposed surface areas. In light of the penetrating nature of S along grain boundaries and the subsequent degradation of the material (Figure 5.10b), it can be reasoned that the presence of carbide precipitates along the grain boundaries (as was observed in the microstructure, see Figure 3.1b) would hinder the diffusion of S deep into the material and therefore the degradation of the 3C material

would proceed at a lower rate compared to the NC alloy. The deeper penetration of S along grain boundaries in NC alloy (Figure 5.10a) is evident when compared to 3C alloy Figure 5.3b).

# **Chapter 6**

## **SUMMARY AND CONCLUSIONS**

The high temperature oxidation and hot corrosion behavior of a carbon-alloyed and binary iron aluminide in pure oxygen environment has been addressed in this thesis. The salient conclusions of the present study are presented in the first half of this chapter and the suggested work for future in the latter half.

### **6.1 Conclusions**

The following were the salient conclusions of the present study.

1. The oxidation of the NC and the 3C alloys was performed at temperatures of 1100K, 1225K and 1330K in pure oxygen. The weight gain versus time data were analyzed using parabolic law, with the NC alloy showing two distinct rates. The initial high rate has been correlated to the formation of the  $\theta\text{-Al}_2\text{O}_3$  and the final lower rate to the formation of  $\alpha\text{-Al}_2\text{O}_3$ . At the lowest temperature of 1100K mainly  $\theta\text{-Al}_2\text{O}_3$  was identified. At the next higher temperature of 1225K, both the aluminas ( $\theta\text{-Al}_2\text{O}_3$  and  $\alpha\text{-Al}_2\text{O}_3$ ) were present in about equal proportions. At the highest temperature of 1330K, only  $\alpha\text{-Al}_2\text{O}_3$  was identified. Topological observations in SEM confirmed the XRD characterization results. FTIR results also proved a second source of confirmation.
2. Slower oxidation kinetics was observed for the 3C alloy compared to NC alloy. The surface coverage of the oxide was less for the case of 3C alloy when compared to that for the NC alloy. This has been correlated to the carbide distribution on the surface of the 3C alloy, preventing the 3C alloy from being uniformly oxidized. Therefore, the carbide particles were relatively stable towards oxidation as they acted as barriers for the diffusion of ions during the oxidation process. The stable nature of the carbide was confirmed by cross-sectional analysis of the oxidized 3C alloy at the highest temperature of 1330K.

3. The NC and 3C alloys were subjected to hot corrosion experiments (coating with  $\text{Na}_2\text{SO}_4$  and exposing to the pure oxygen environment) at the same temperature as that of oxidation, i.e. 1100K, 1225K and 1330K. The raw data was fitted to the parabolic law. The kinetics of hot corrosion of the NC alloy was faster than that of 3C alloy.
4. Cross-sectional analysis of hot corroded NC and 3C alloy revealed several interesting features. Cross-sectional analysis revealed that the base metal was attacked in a characteristic manner, with pitting at the metal-scale interface (wave-like features) and enhanced attack along grain boundaries in the case of the NC alloy. Within these grooves and pits, corrosion products were identified by EPMA analysis. The external scales were mostly identified as  $\text{Fe}_2\text{O}_3$  and  $\text{Al}_2\text{O}_3$  and S was not present there. On the other hand, S was found deep within the oxide for both the alloys. EPMA analysis strongly pointed to the presence of S at the metal-scale boundaries, while confirming the presence of aluminium sulphide deep within the NC alloy along grain boundaries. The hot corrosion kinetics were faster compared to oxidation kinetics due to the formation of these sulphides at the metal-oxide interface, which enhance the rate of attack by enhancing the rate of diffusion.
5. The rate of hot corrosion was slow when the  $\text{Na}_2\text{SO}_4$  salt did not melt on the surface. The possible sequence of attack in hot corrosion has been proposed based on the microstructural and compositional analyses. For the initiation of hot corrosion, it is essential that the salt should melt. This melt fluxes  $\text{Al}_2\text{O}_3$ , although it is not known for sure if this occurs by the acidic or basic fluxing mechanism. The fluxing of alumina results in the oxidation of iron and thereby higher attack rates are observed. The sulphur from the melt diffuses further down to the metal-scale interface. As the partial pressure of oxygen is low at this location, sulphur activity at this location results in sulphide formation. The oxidation of sulphides produces the corresponding oxide and releases sulphur, which again diffuses inward into the base intermetallic to cause further sulphide formation and further attack. In this manner, rapid attack is could be realized during the propagation stage.

6. The presence of carbides along grain boundary in the 3C alloy results in a lower rate of hot corrosion, since the carbide particles would hinder the diffusion of sulphur deeper within the base intermetallic.

## 6.2 Suggestions for Future Work

Some of the additional works, which is needed to be undertaken in order to resolve some of the issues raised in this thesis, are:

1. Cross-sectional analysis of both the alloys should be done at all the temperatures for both types of experiment. This would help to understand the process better.
2. Analysing the scale cross-sections of the specimens as a function of time, by utilizing different specimens for different times at the same temperature would give us an insight into the detailed mechanism operating in the system at the initial stage.
3. Measuring the scale thickness as a function of time at the different temperatures would also help us to identify the corrosion rates (oxidation and hot corrosion) at the different temperatures.
4. Mapping of the elements (specially S and O) is needed to know in details about the depth of attack and hence the diffusion of the particular elements deep within the substrate material.
5. Quantitative analysis of certain phases needs to be performed, either by EDAX or by EPMA, to know perfectly what is the exact chemical composition of those products, specially the corrosion products in the pits.

## References

- [1] N.S.Stoloff, “Ordered alloys-physical metallurgy and structural applications”, *International Metal Review*, **29**, 123-135 (1984).
- [2] C.T.Liu, J.O.Stiegler and F.H.Froes, “Ordered Intermetallics”, *Metal Handbook 10 th ed., ASM, Materials Park, USA*, **2**, 913-942 (1990).
- [3] C.T.Liu and K.S.Kumar, “Ordered Intermetallic alloys, Part 1,Nickel and Iron aluminides”, *J.Metals.* **45**, 38-44 (1993).
- [4] R.G.Baligidad, U.Prakash, A.Radhakrishna, V.Ramakrishna Rao, P.K.Rao and N.B.Ballal, “Effect of carbides on embrittlement of Fe<sub>3</sub>Al based intermetallic alloys”, *Scripta Mater.*, **36**, 667-671 (1997).
- [5] R.G.Baligidad, U.Prakash, A.Radhakrishna, V.Ramakrishna Rao, P.K.Rao and N.B.Ballal, “Effect of carbon contents on high temperature tensile properties of Fe<sub>3</sub>Al based intermetallic alloy”, *Scripta Mater.*, **36**, 105-109 (1997).
- [6] P.Kofstad, *High Temperature Corrosion*, Elsevier Applied Science, London, 1988.
- [7] J.Klower, “High temperature Corrosion Behaviour of Iron Aluminides and Iron-Aluminium-Chromium alloys”, *Oxidation of Intermetallics*, Edited by H.J.Grabke and M.Schutze, Wiley-VCH, 203-220 (1997).
- [8] P.F.Tortorelli and J.H.DeVan, “High temperature aluminides and intermetallics”, S.H.Whang et al. (eds), Elsevier Applied Science, Essec, 573 (1992).
- [9] M.J.Marcinokowsky and M.E.Taylor, *Journal of Mat.Sci.* **10**, 406 (1995).
- [10] R.Prescott and M.J.Graham, “The Oxidation of Iron-Aluminium alloys”, *Oxidation of Metals*, **38**, 73-87 (1992).
- [11] C.S.Barrett and T.B.Massalski, *Structure of Metals*, 3<sup>rd</sup> ed., McGraw Hill, (1966).
- [12] O.Kubaschewski and B.E.Hopkins, *Oxidation of Metals and Alloys*, 2<sup>nd</sup> ed. Butterworths, London (1967).
- [13] T.K.Roy, “High Temperature Oxidation of Ti<sub>3</sub>Al-based Intermetallic Alloys”, Ph.D. thesis, I.I.T.Kanpur, India (1995).

[14] G.H.Meier, "Fundamentals of the Oxidation of High-Temperature Intermetallics", *Oxidation of High-Temperature Intermetallics*, Edited by T.Grobstein and J.Doychak, TMS, Warrendale, 1-16 (1988).

[15] G.H.Meier, "Research on Oxidation and Embrittlement of Intermetallic Compounds in the US", *Oxidation of Intermetallics*, Edited by H.J.Grabke and M.Schutze, Wiley-VCH Publ. 15-58 (1997).

[16] P.Tomaszewicz and G.R.Wallwork, "Observations of Nodule Growth during the Oxidation of pure binary Iron-Aluminium Alloys", *Oxidation of Metals*, **19**, Nos.5/6, 165-185 (1983).

[17] C.Sykes and J.W.Bampfylde, "Physical Properties of Iron-Aluminium Alloys", *J. Iron Steel Inst. Adv. Copy*, **12**, 22 (1934).

[18] P.F.Tortorelli and J.H.DeVan, "Compositional Influences on the High Temperature Corrosion Resistance of Iron-Aluminides", *Processing, Properties and Applications of Iron Aluminides*, Edited by J.H.Schneibel and M.A.Crimp, TMS, Warrendale, 257-270 (1994).

[19] W.H.Gitzen, "Alumina as a ceramic material", *Am. Ceram. Soc.* (1970).

[20] P.F.Tortorelli and J.H.DeVan, *Mater. Sci. Eng.*, **A153**, 573-577 (1992).

[21] L.N.Larikov, V.V.Geichenko and V.M.Fal'chenko, "Diffusion Processes in Ordered Alloys", published by Amerind Publishing Co. Pvt. Ltd., New Delhi, (1981).

[22] W.E.Boggs, "The Oxidation of Iron-Aluminium Alloys from 450° to 900°C ", *J. Electrochem. Soc.*, **118(6)**, 906-913 (1971).

[23] G.C.Rybicki and J.L.Smialek, "Effect of the  $\theta\text{-}\alpha$   $\text{Al}_2\text{O}_3$  transformation on the oxidation behavior of  $\beta\text{-NiAl} + \text{Zr}$ ", *Oxidation of Metals*, **31**, 275-304 (1989).

[24] W.D.Kingery, "Introduction to Ceramics", Wiley, (1975).

[25] N.Babu, "Room Temperature Aqueous Corrosion and High Temperature Oxidation of Iron-Aluminides", M.Tech. thesis, I.I.T.Kanpur, India (1998).

[26] P.Tomaszewicz and G.R.Wallwork, *Rev. High Temp. Materials*, **4**, 75-105 (1978).

[27] C.H.Kao and C.M.Wan, "Effect of carbon on the oxidation of Fe-5.5Al-0.55C alloy", *Jl. of Materials Science*, **22**, 3203-3208 (1987).

- [28] C.H.Kao and C.M.Wan, "Effect of temperature on the oxidation of Fe-7.5Al-0.65C alloy", *J of Materials Science*, **23**, 1943-1947 (1988).
- [29] N.Birks and G.H.Meier, *Introduction to High Temperature Oxidation of Metals*, Edward-Arnold (1982).
- [30] W.H.Lee and R.Y.Lin, *Proc. Fourth Annual Conf. Fossil Energy*, R.R.Judkins and D.N.Braski (comp.), ORNL/FMP-90/1, U.S.Department of Energy, 475-486 (1990).
- [31] F.Gesmundo, Y.Niu, F.Viani and O.Tassa, *J. de Phys.*, IV **C9**, 375-381 (1993).
- [32] M.A.E.Medina, M.Casales, A.M.Villafane, J.P.Calderon, L.Martinez and J.G.G.Rodriguez, "Hot Corrosion of atomized iron aluminides doped with boron and reinforced with alumina", *Mat. Sci. & Engg. A*, **A300**, 183-189 (2001).
- [33] P.Banerjee, "Hydrogen behaviour in chromium and titanium alloyed iron aluminide intermetallics", M.Tech Thesis, I.I.T Kanpur, India (1997).
- [34] J.L.Smialek, J.Doychak and D.J.Gaydosh, "Oxidation behavior of FeAl + Hf, Zr, B", *Oxidation of High Temperature Intermetallics*, Edited by T.Grobstein and J.Doychak, TMS, 83-95 (1988).
- [35] I.Rommerskirchen, B.Eltester and H.J.Grabke, "Oxidation of  $\beta$ -FeAl and FeAl alloys", *Materials and Corrosion*, **47**, 646-649 (1996).
- [36] S.Astha, "Electrochemical Behaviour of  $Fe_3Al$ -M (M=Ti,Zr, V ,Nb, Ta, Cr, Mo and W) Intermetallics", M.Tech Thesis, I.I.T Kanpur, India (1996).
- [37] R.G.Baligidad, U.Prakash, V.Ramakrishna Rao, P.K.Rao and N.B.Ballal, "Electroslag remelting of Fe-28at % Al intermetallic alloy", *Iron and Steel making*, **21**, 324-331 (1994).
- [38] M.Sen, "Environmental Degradation of Carbon-Alloyed  $Fe_3Al$ -based Intermetallics", M.Tech. thesis, I.I.T.Kanpur, India (2000).
- [39] K.L.Luthra and D.A.Shores, "Mechanism of  $Na_2SO_4$  induced corrosion at 600°-900°C ", *J. Electrochem.Soc*, 2202-2210 (1980).
- [40] R.Narayan and R.Arghode, "Aluminium-Nickel Composite Powders by Electroless Nickel Plating ", *Int. J. Powder Met. & Pow. Tech.*, **19**, 101-105 (1983).

- [41] JCPDS Powder Diffraction Files, *PCPDFWIN Software*, Joint Committee on Powder Diffraction Standards, International Centre for Diffraction Data, Swarthmore, USA (1996).
- [42] F.D.Richardson and J.H.E.Jeffes, *J. Iron and Steel Inst.*, **160**, 261 (1948).
- [43] R.A.Rapp, *Corrosion*, **42**, 568 (1986).
- [44] P.D.Jose, D.K.Gupta and R.A.Rapp, *J. Electrochem. Soc.*, **132**, 735, (1985).
- [45] J.A.Goebel and F.S.Pettit, *Metall. Trans.*, **1**, 1943 (1970).
- [46] K.P.Lillerud and P.Kofstad, *Oxid. Met.*, **21**, 233 (1984).
- [47] O.Kubaschewski and C.B.Alcock, Metallurgical Thermochemistry, 5<sup>th</sup> edition, Pergamon Press.

## **Appendix: A**

This Appendix gives the raw data of the weight gain per unit area ( $\Delta W/A$ ) versus ( $t$ ) for both the NC and 3C alloys for both oxidation and hot corrosion experiments at all the temperatures.

**Table : Oxidation datas for the alloy 3C**

1100K ( 3C-25)			1225K ( 3C-23)			1330K ( 3C- 27)		
Time (ks)	$(\Delta W/A)$ $(kgm^{-2})$ $\times 10^3$	$(\Delta W/A)^2$ $(kg^2m^{-4})$ $\times 10^6$	Time (ks)	$(\Delta W/A)$ $(kgm^{-2})$ $\times 10^3$	$(\Delta W/A)^2$ $(kg^2m^{-4})$ $\times 10^6$	Time (ks)	$(\Delta W/A)$ $(kgm^{-2})$ $\times 10^3$	$(\Delta W/A)^2$ $(kg^2m^{-4})$ $\times 10^6$
1.8	0.8710	0.7586	1.8	1.4986	2.2458	1.8	1.0652	1.1346
3.6	1.1614	1.3488	3.6	1.4986	2.2458	3.6	1.2427	1.5443
14.4	1.4517	2.1074	7.2	2.7474	7.5482	7.2	1.4203	2.0172
28.8	1.7421	3.0349	14.4	2.9971	8.9826	28.8	2.1304	4.5386
43.2	2.6131	6.8283	28.8	3.6215	13.1153	57.6	2.3080	5.3269
90.0	2.9034	8.4297	90	3.7464	14.0355	115.2	2.6630	7.0916
115.2	3.1938	10.2003	115.2	3.4966	12.2262	158.4	3.5507	12.6075
172.8	3.1938	10.2003	162	3.7464	14.0355	201.6	3.7283	13.9002
234.0	3.7745	14.2468	234.0	3.7464	14.0355	234.0	4.0478	16.3847

**Table : Oxidation datas for the alloy NC**

1100K ( NC-10)			1225K ( NC-13)			1330K ( NC-14)		
Time (ks)	$(\Delta W/A)$ $(kgm^{-2})$ $\times 10^3$	$(\Delta W/A)^2$ $(kg^2m^{-4})$ $\times 10^6$	Time (ks)	$(\Delta W/A)$ $(kgm^{-2})$ $\times 10^3$	$(\Delta W/A)^2$ $(kg^2m^{-4})$ $\times 10^6$	Time (ks)	$(\Delta W/A)$ $(kgm^{-2})$ $\times 10^3$	$(\Delta W/A)^2$ $(kg^2m^{-4})$ $\times 10^6$
1.8	0.9336	0.8716	1.8	3.6486	13.3123	1.8	3.1909	10.1818
3.6	1.4004	1.9611	3.6	4.1699	17.3881	3.6	4.9091	24.0993
7.2	1.6338	2.6693	7.2	4.4305	19.6293	7.2	5.0072	25.0720
14.4	1.6338	2.6693	14.4	4.6911	22.0064	14.4	5.1545	26.5689
28.8	1.7272	2.9832	28.8	4.7953	22.9949	57.6	5.2036	27.0774
57.6	1.7739	3.1467	86.4	4.8996	24.0061	86.4	5.3018	28.1091
100.8	1.8672	3.4864	115.2	5.1081	26.0927	129.6	5.3509	28.6321
144.0	1.8672	3.4864	151.2	5.1602	26.6277	172.8	5.40	29.16
187.2	1.8672	3.4864	201.6	5.2123	27.1681	234.0	5.4491	29.6927
234.0	1.8672	3.4864	234.0	5.3166	28.2662			

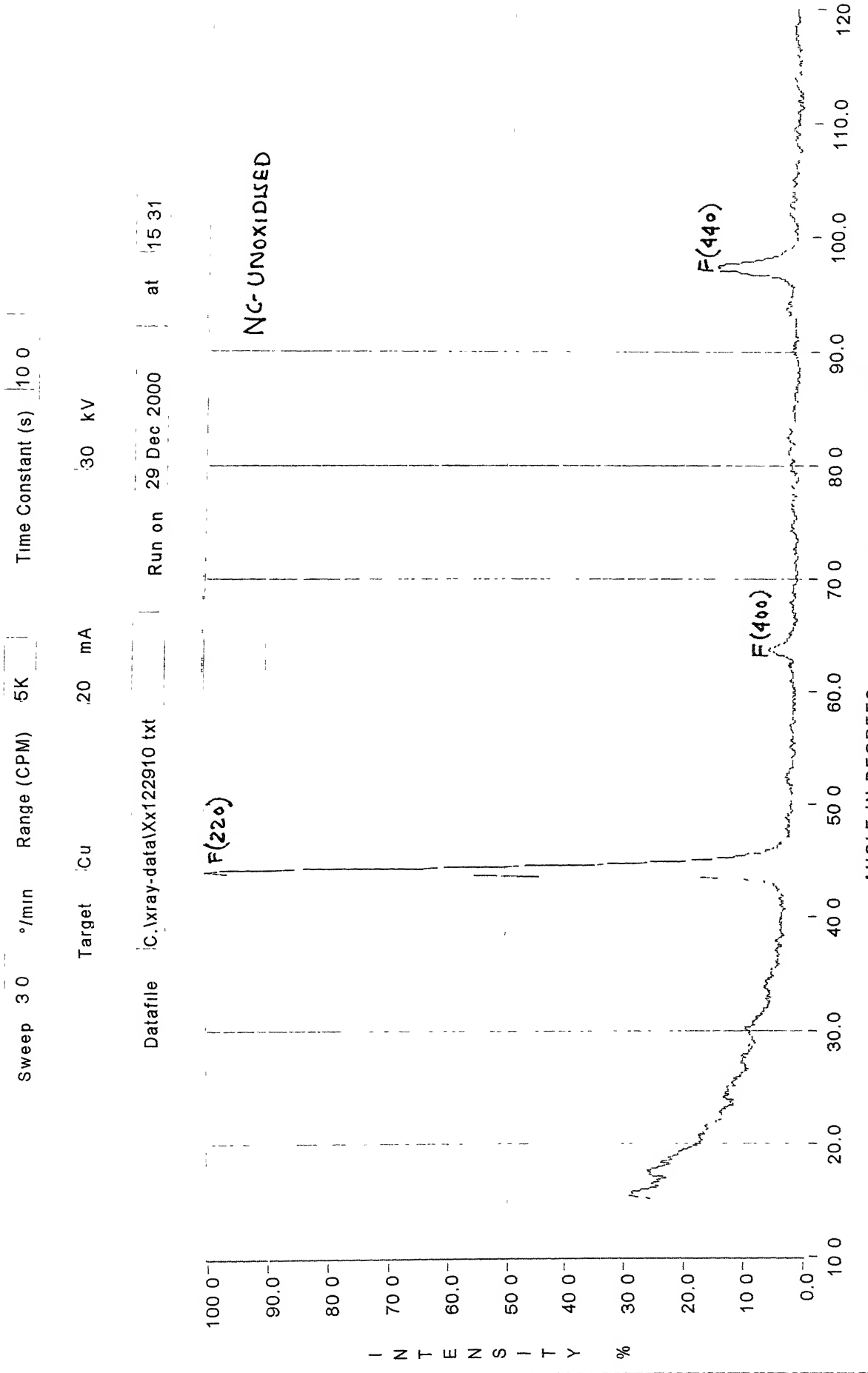
## **Appendix: B**

This Appendix gives the XRD plots for all the experiments conducted for both the alloys at all the temperatures. The peaks for all the phases obtained have been marked on the plot itself for the facility of the analysis. The following symbols and letters were used denote the particular phases which are shown below in the Table. Alongside, is also given the JCPDS file number with which the particular phase have been matched. It is to be noted that all throughout a particular phase was matched with a single JCPDS file. For convenience, the particular JCPDS file is also attached at the end.

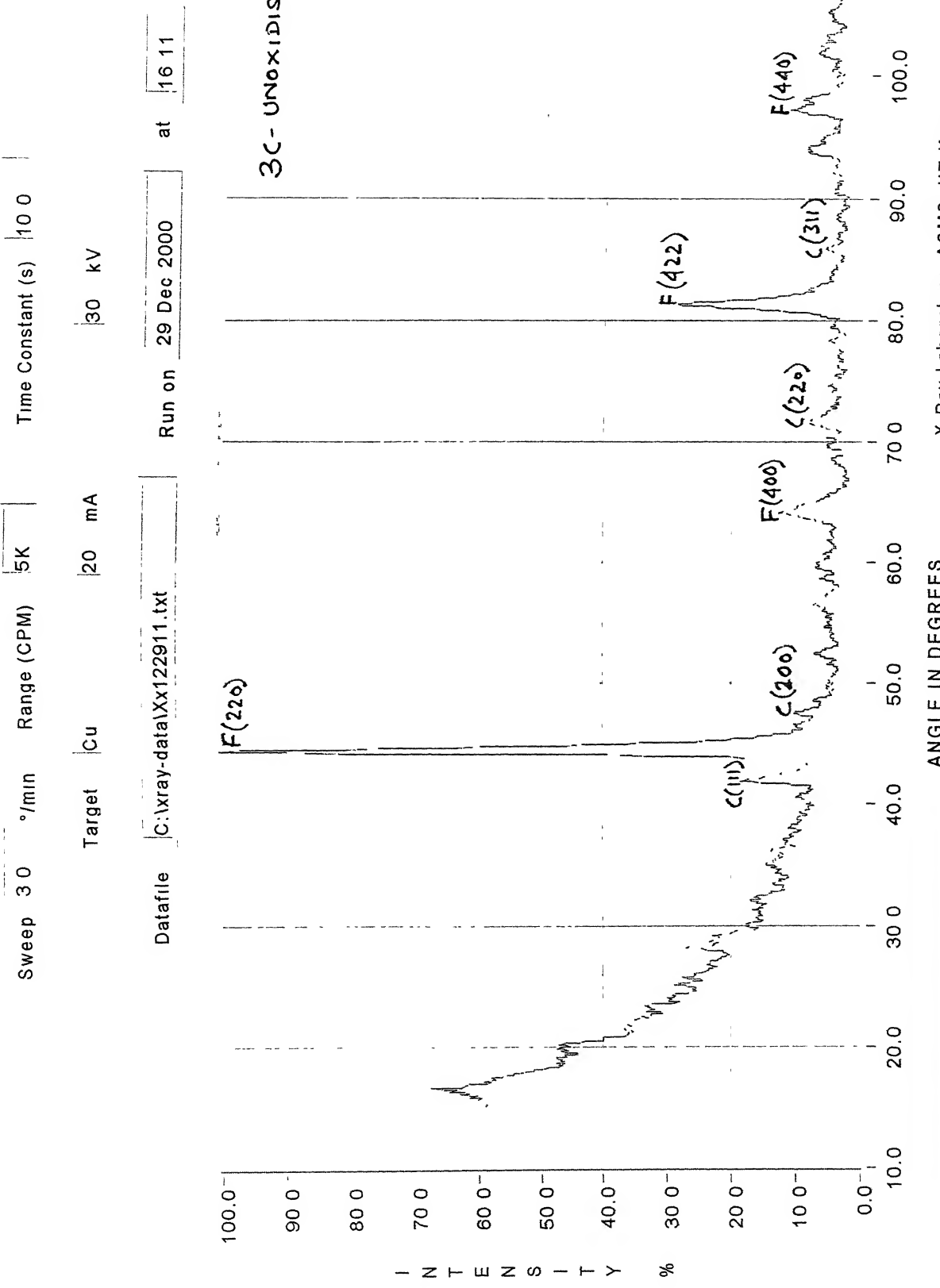
**Table of symbols used to denote the phases in the XRD plots**

<b>Symbol</b>	<b>Compound</b>	<b>JCPDS File No.</b>
F	Fe <sub>3</sub> Al	45-1203
C	Fe <sub>3</sub> AlC <sub>0.5</sub>	29-0044
Fe	α-Fe <sub>2</sub> O <sub>3</sub>	03-0800
α	α-Al <sub>2</sub> O <sub>3</sub>	46-1212
θ	θ-Al <sub>2</sub> O <sub>3</sub>	35-0121

## XRD NC-Unoxidised

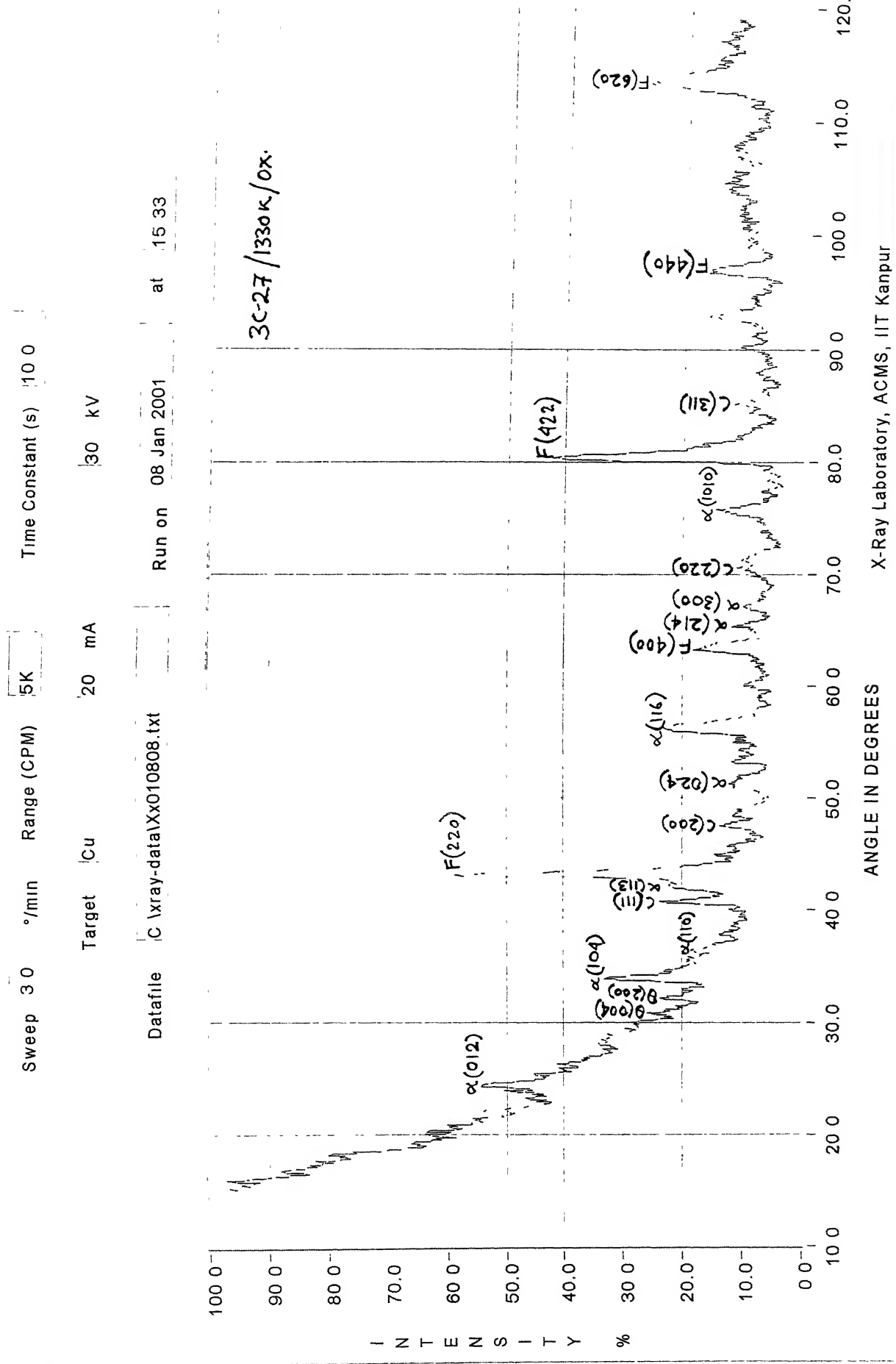


# XRD 3C-Unoxidised

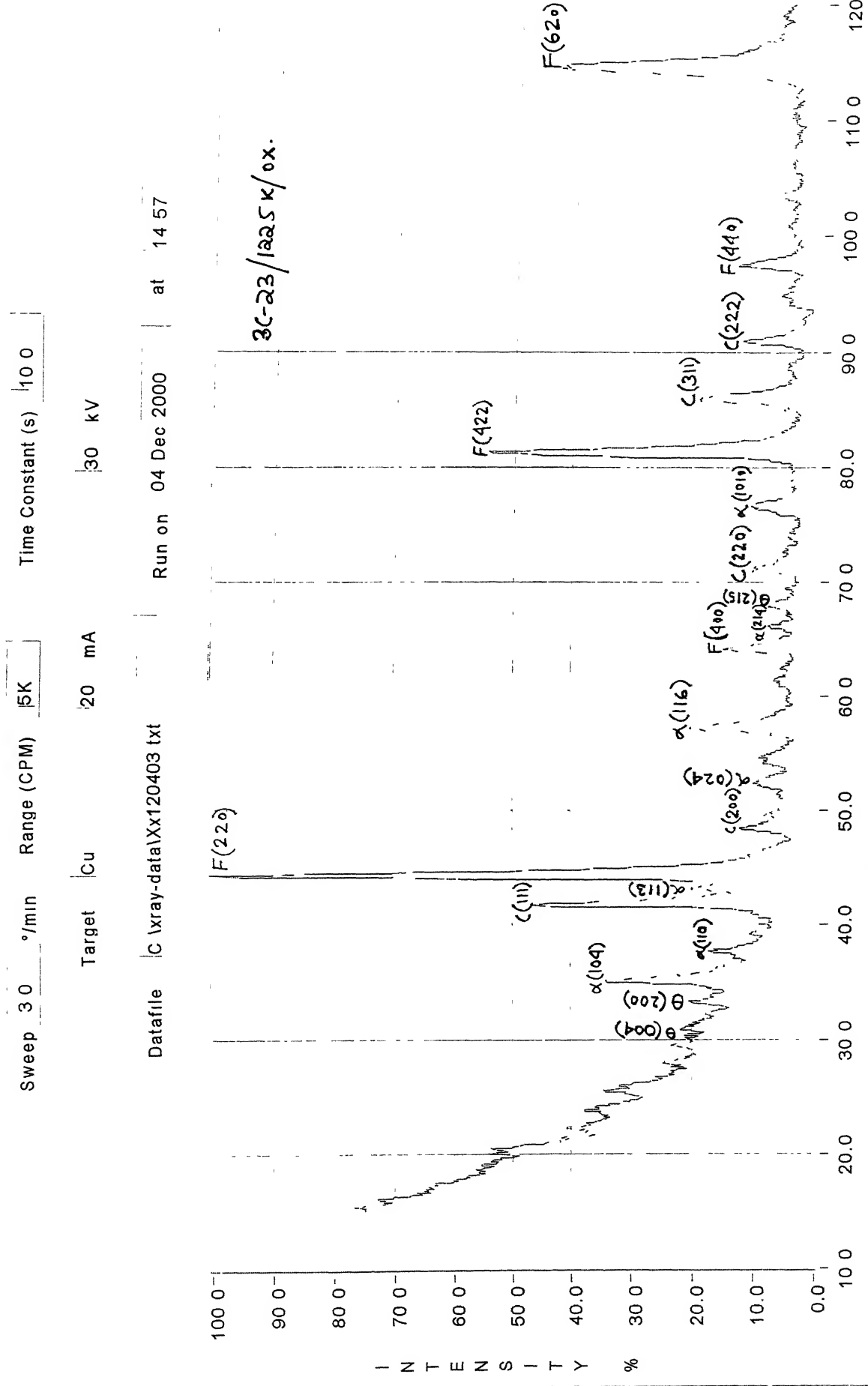


X-Ray Laboratory, ACMS, IIT Kanpur

# XRD 3C-27/1330/65hrs-cont.

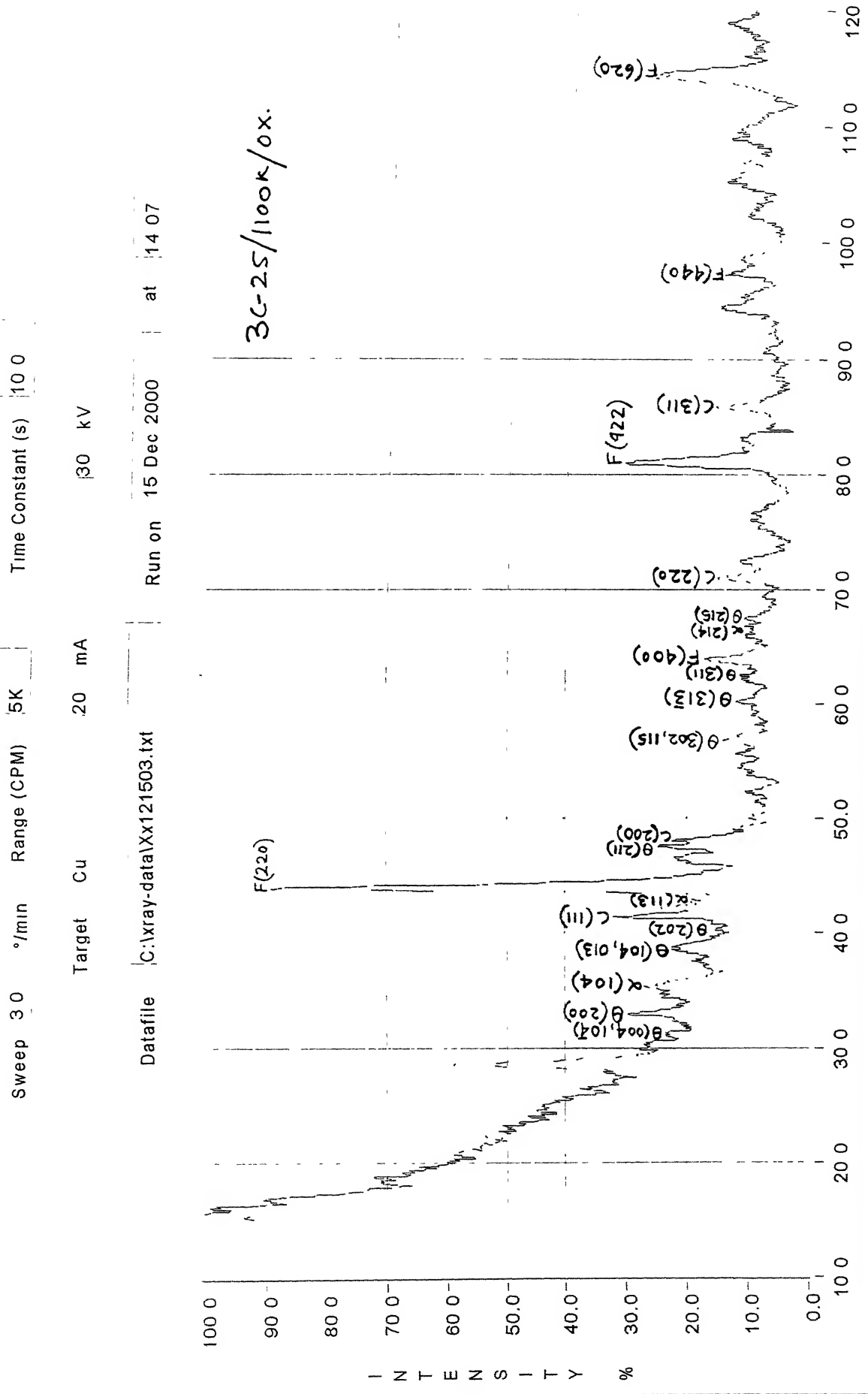


# XRD 3C-23/1225/65hrs-cont.

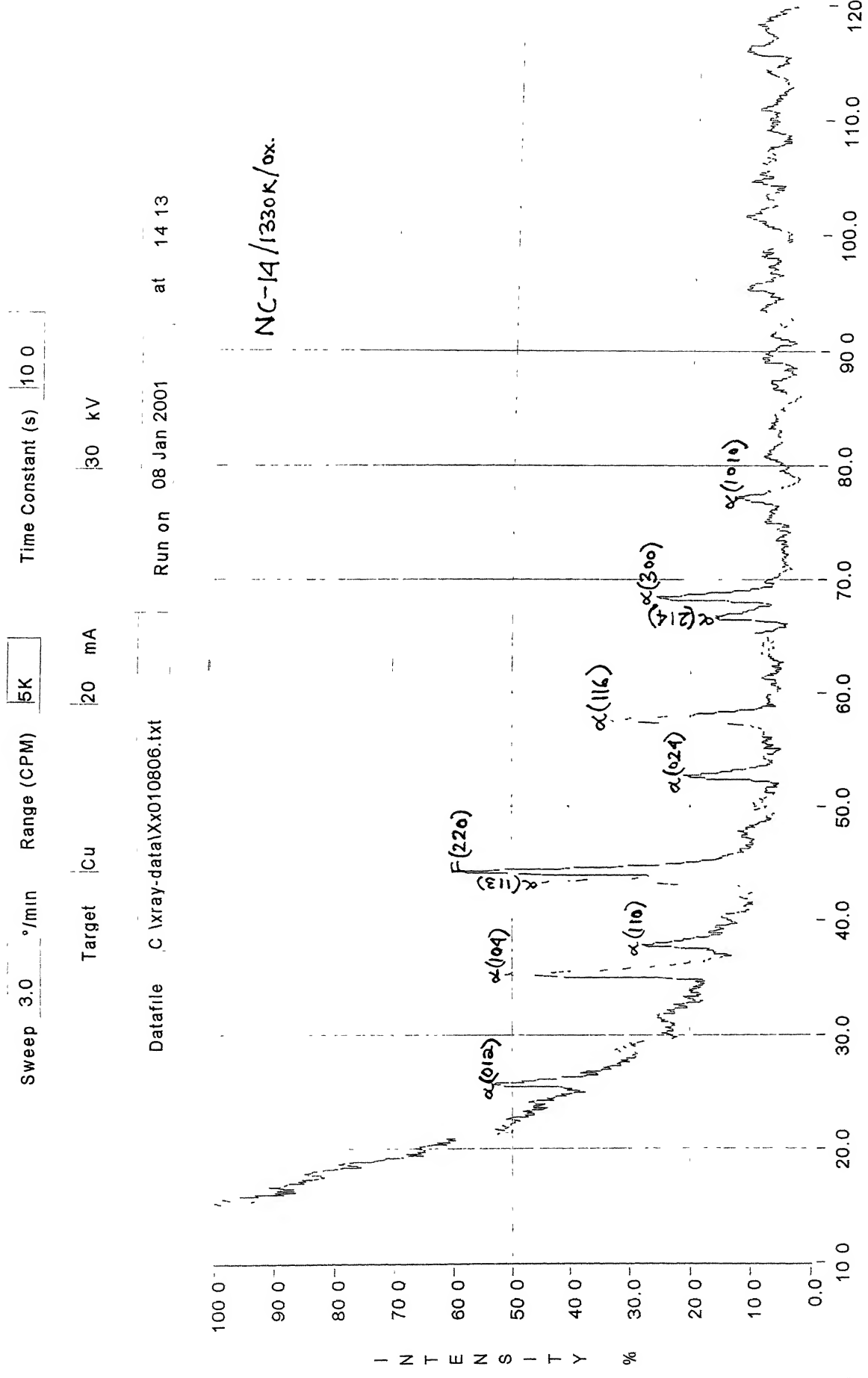


X-Ray Laboratory, ACMS, IIT Kanpur

# XRD 3C-25/1100/65hrs-cont.

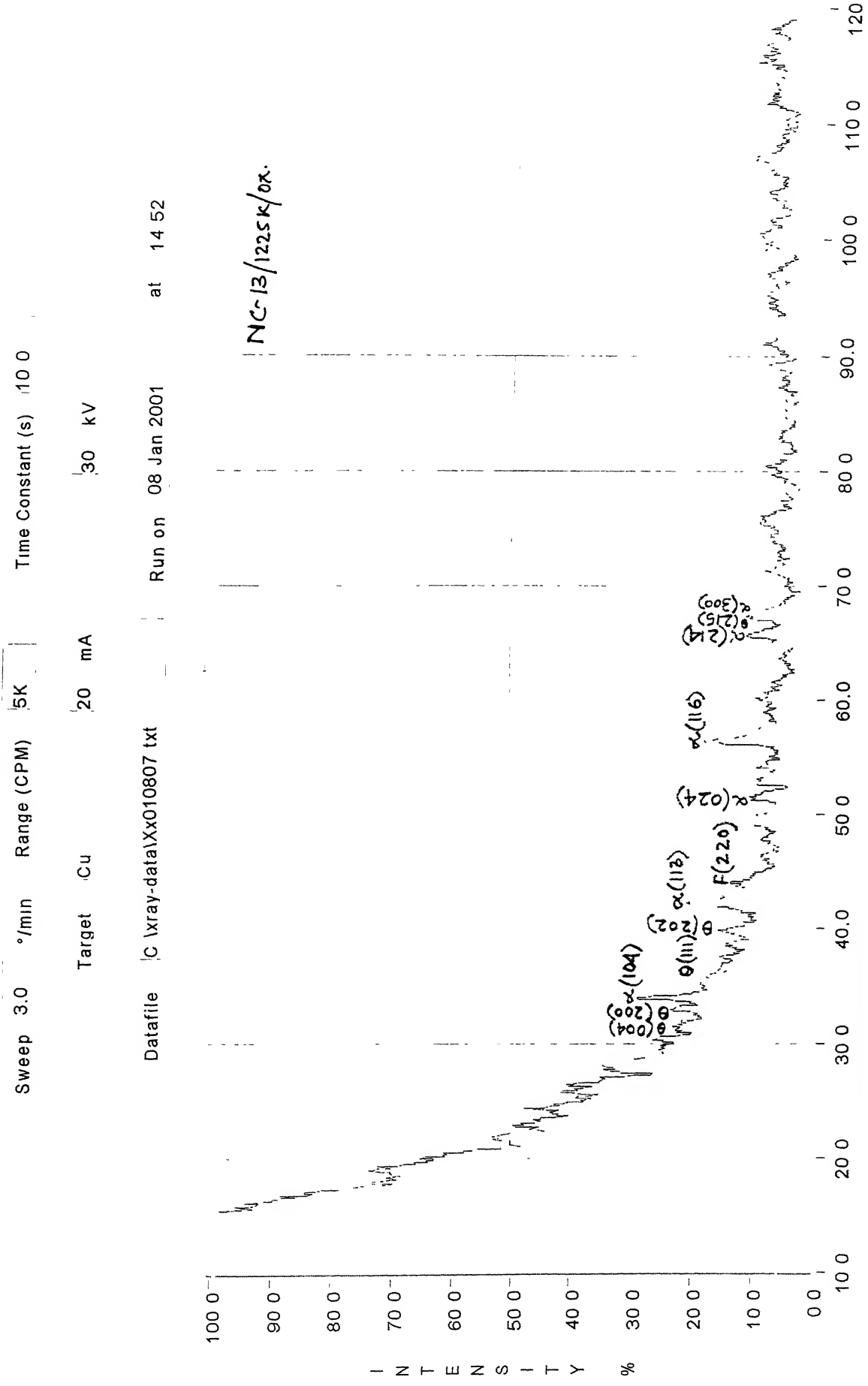


# XRD NC-14/1330/65hrs-cont.



X-Ray Laboratory, ACMS, IIT Kanpur

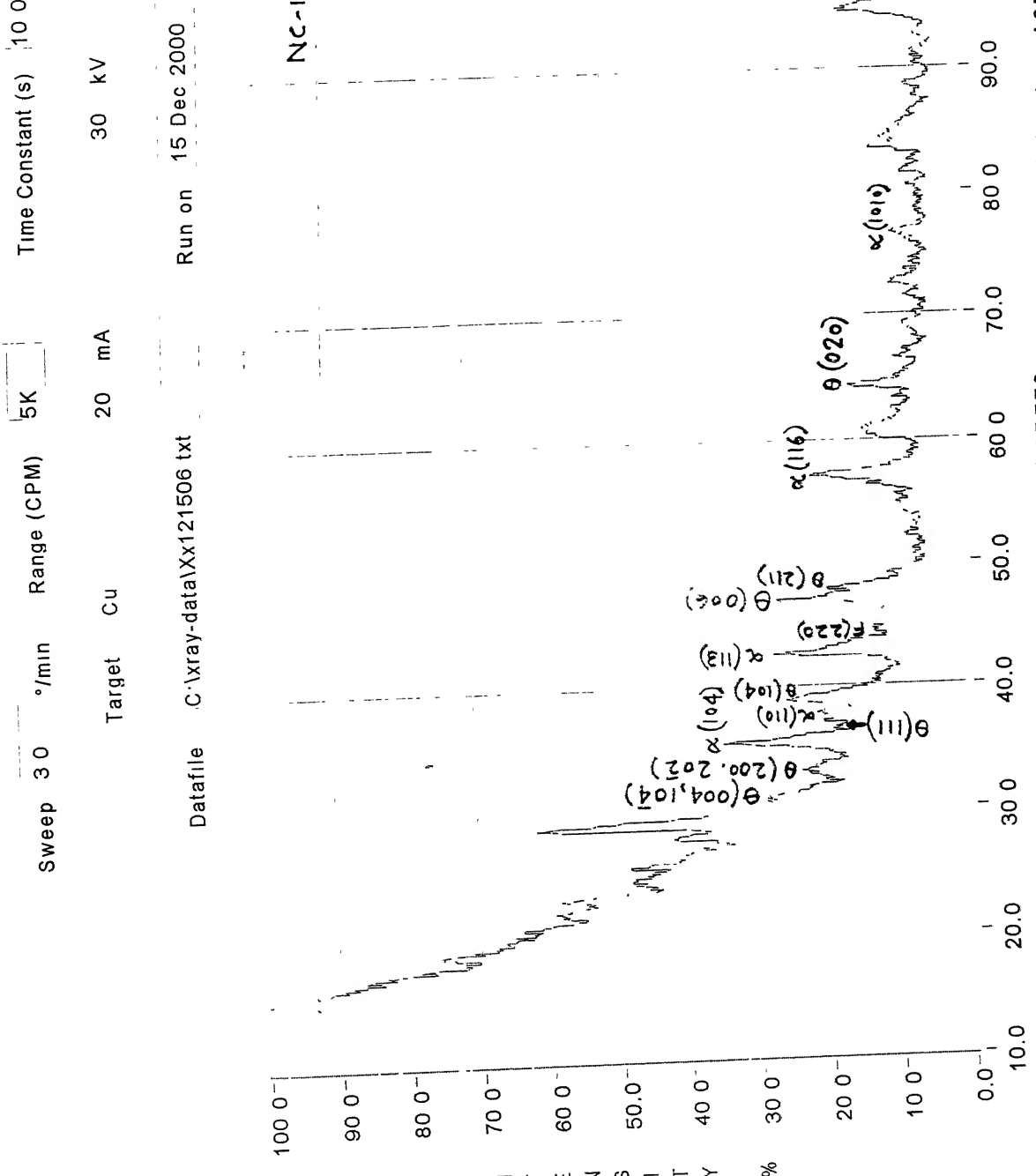
# XRD NC-13/1225/65hrs-cont.



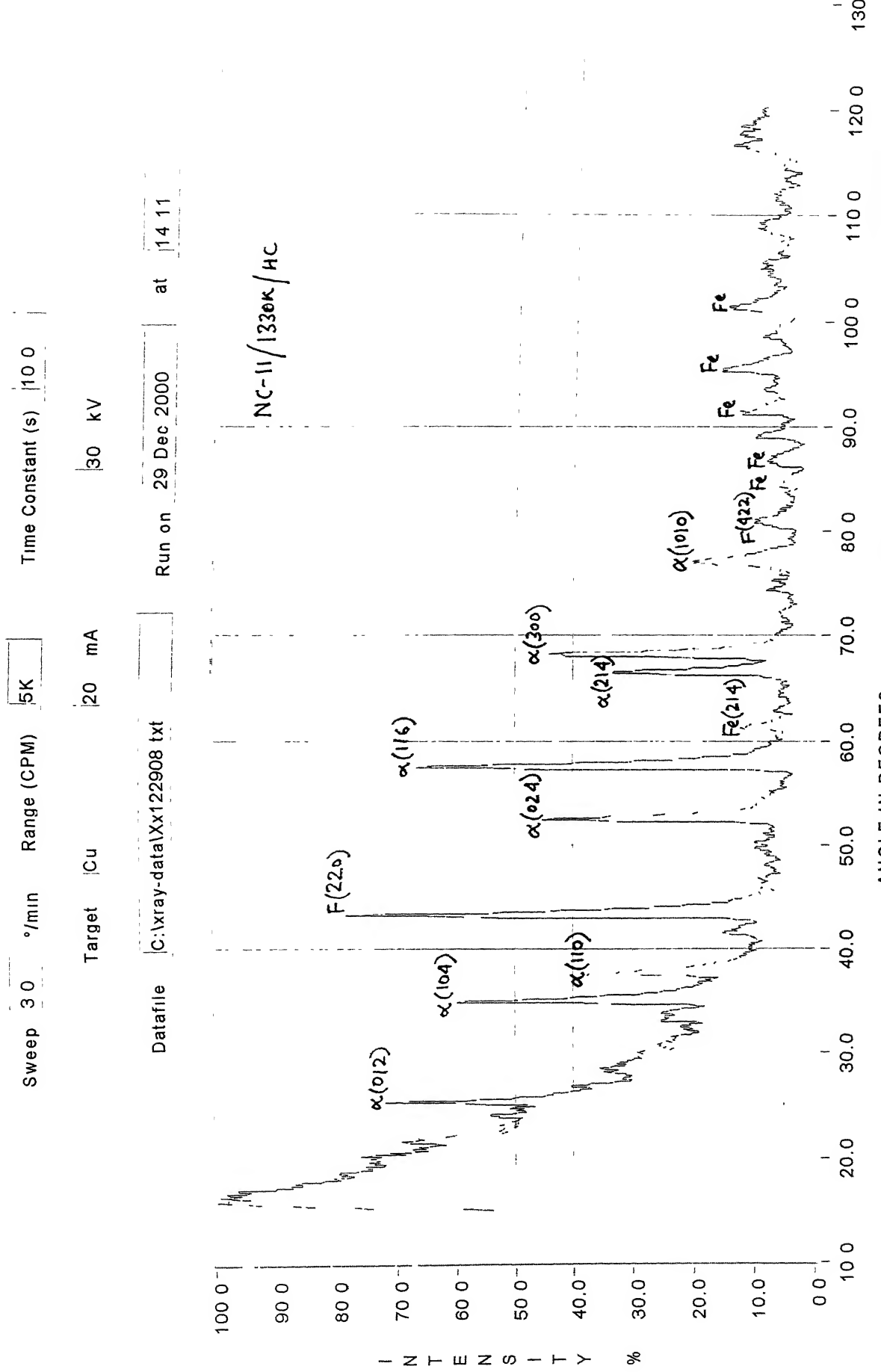
ANGLE IN DEGREES

X-Ray Laboratory, ACMS, IIT Kanpur

## XRD NC-10/1100/65hrs-cont.



# XRD NC-11/1330/65hrs-cont./Hot-Corr.

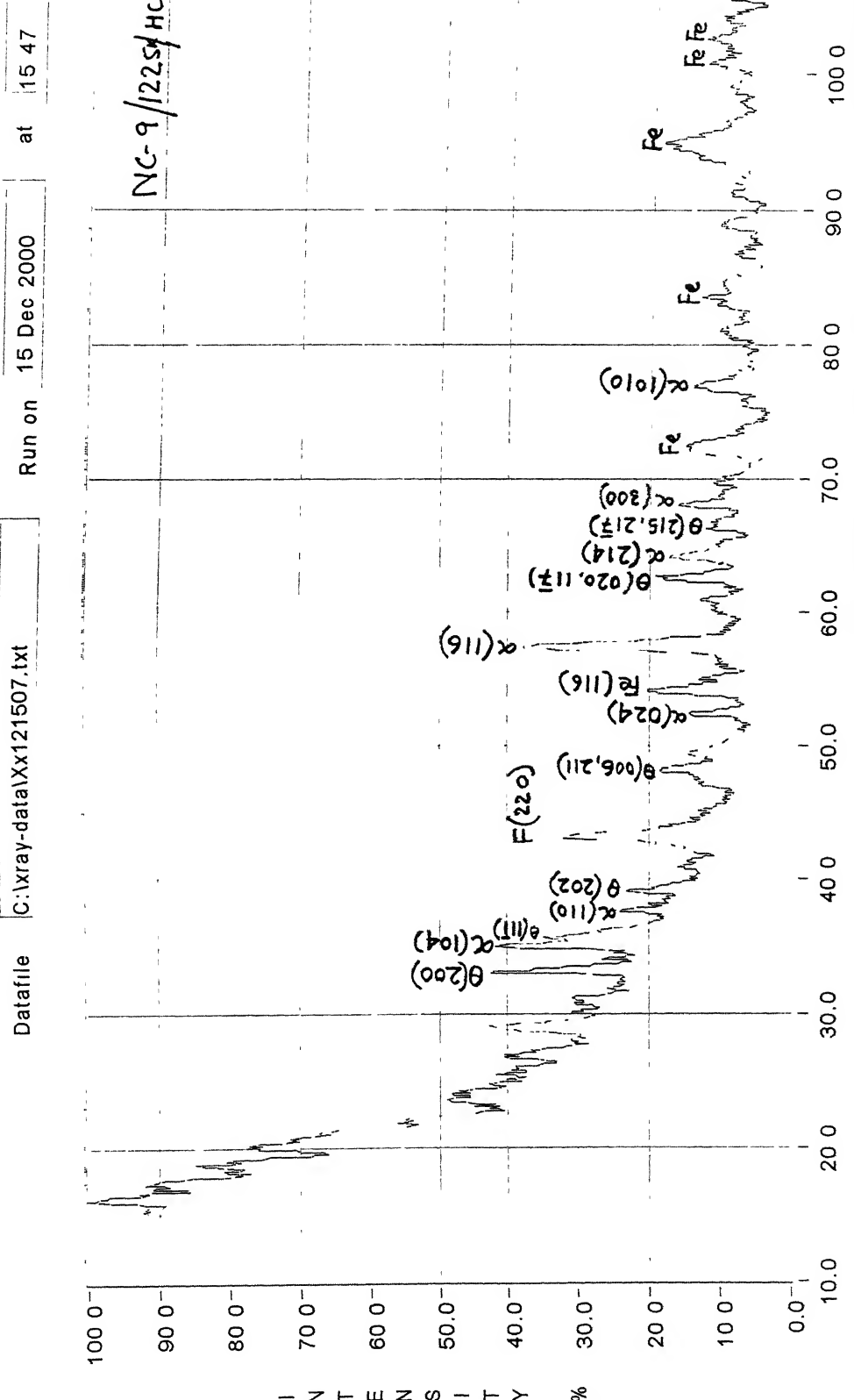


X-Ray Laboratory, ACMS, IIT Kanpur

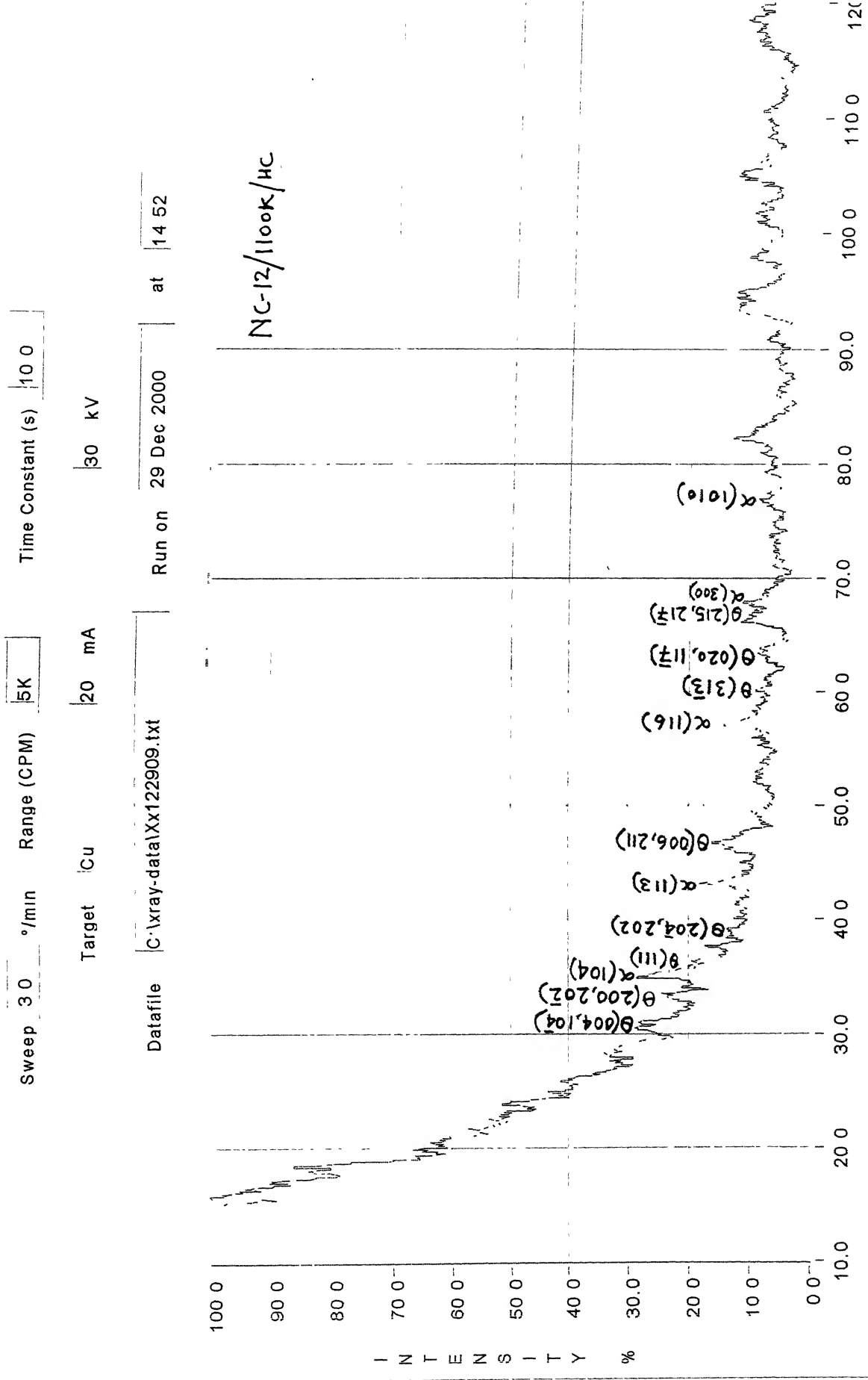
# XRD NC-9/1225/65hrs-cont/Hot-Corr.

Sweep 3 0 °/min Range (CPM) 5K Time Constant (s) 10 0

Target Cu 20 mA 30 kV



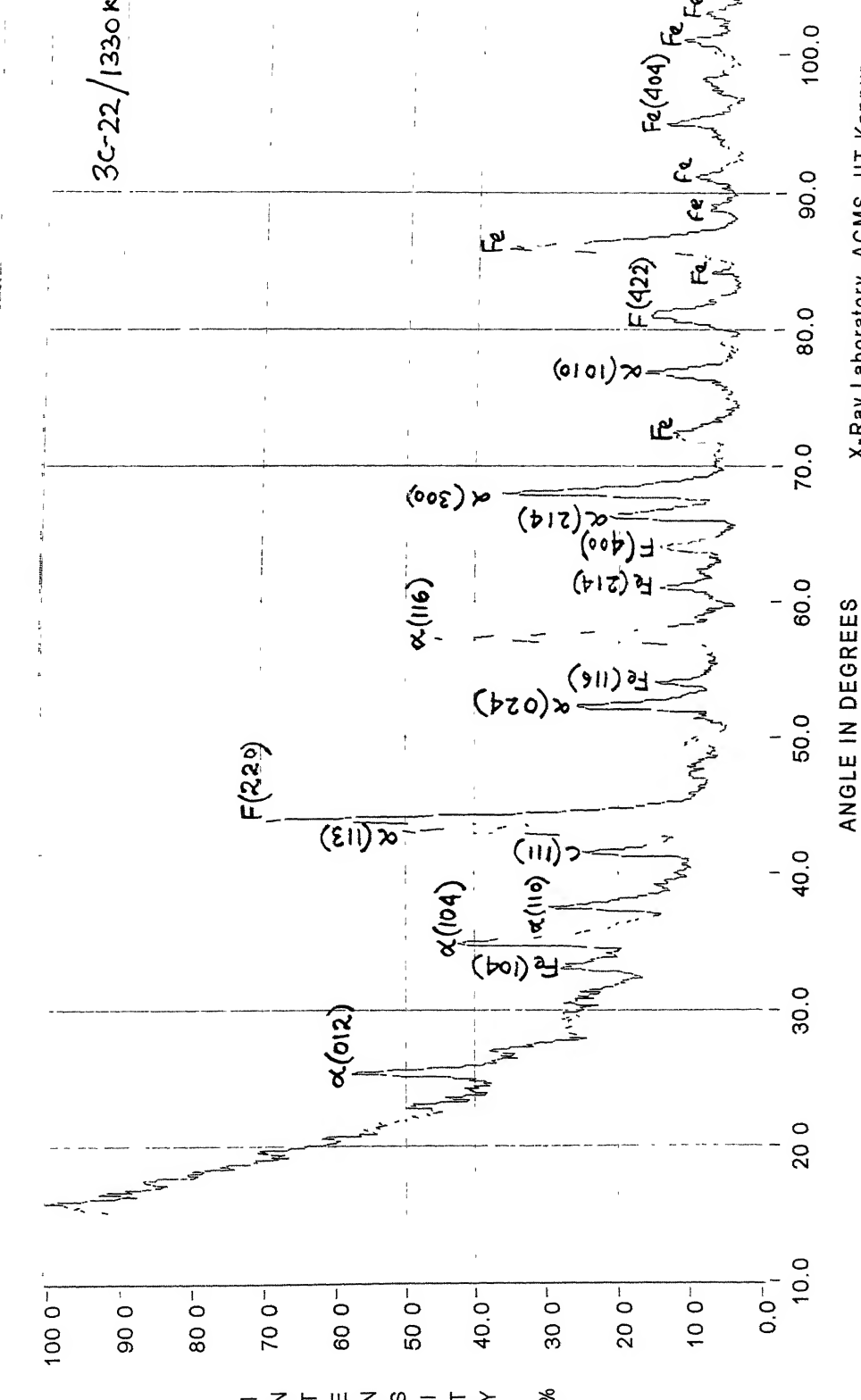
# XRD NC-12/1100/65hrs-cont./Hot-Corr.



# XRD 3C-22/1330/65hrs-cont./Hot-Corr.

Sweep	3 0	°/min	Range (CPM)	5K	Time Constant (s)	100
Target	Cu		20 mA			

Datafile C:\xray-data\Xx010200.txt



XRD 3C-28/1225/65hrs-cont./Hot-Corr.

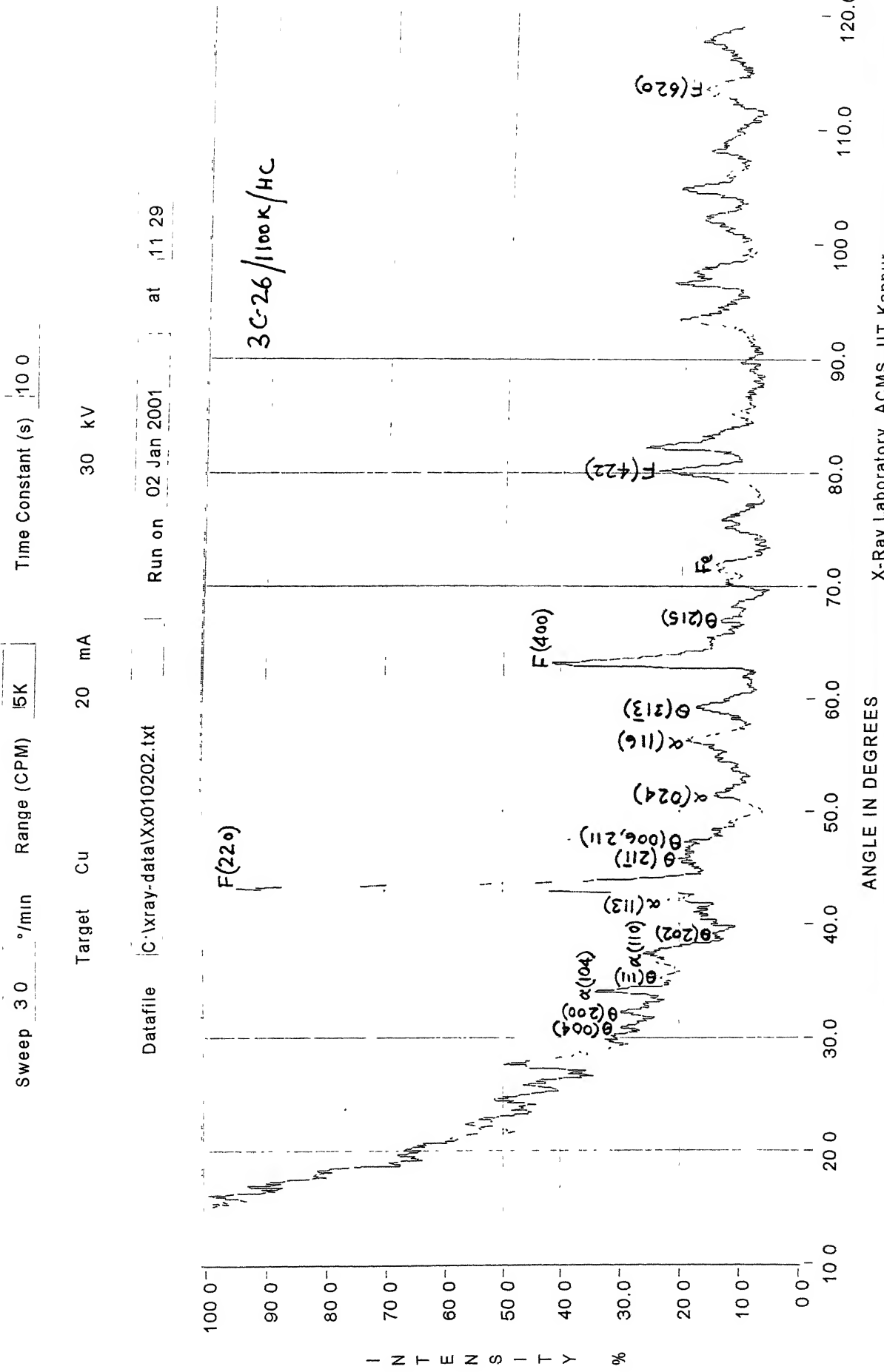
The figure displays an X-ray diffraction (XRD) pattern with the following parameters:

- Sweep**: 30 °/min
- Target**: Cu
- Range (CPM)**: 5K
- Time Constant (s)**: 10.0
- Datafile**: C:\xray-data\Xx010201.txt
- Run on**: 02 Jan 2001
- at**: 10 50

The pattern shows several distinct peaks corresponding to different crystallographic planes of the materials present. The labeled peaks include:

- $\alpha(012)$
- $\theta(004, 104)$
- $\theta(200)$
- $\theta(110)$
- $\theta(202, 207)$
- $\theta(113)$
- $C(111)$
- $\alpha(200, 006)$
- $\alpha(024)$
- $\alpha(116)$
- $F(220)$
- $F(400)$
- $F(422)$
- $\alpha(214)$
- $\alpha(300)$
- $\alpha(104)$
- $Fe(214)$
- $Fe(404)$
- $Fe(620)$

# XRD 3C-26/1100/65hrs-cont./Hot-Corr.



X-Ray Laboratory, ACMS, IIT Kanpur

45-1203

Wavelength = 154184

AlFe3

Aluminum Iron

Rad CuKa1  $\lambda$  15405 Filter d-sp Calculated

Cut off Int Calculated I/Icor

Ref Hubbard, C., Oak Ridge National Laboratory, High Temp  
Mat Lab, Oak Ridge, TN, USA, Private Communication, (1993)Sys Cubic S G Fm3m (225)  
a 57934 b c A C  
 $\alpha$   $\beta$   $\gamma$  Z 4 mp

Ref. Ccwdery, S., Kayser, F., Mater Res. Bull., 14, 91 (1979)

Dx. 6.645 Dm. SS/FOM.  $F_{12}=285(0.0025, 17)$ 

Bi F3 type PSC cF16 Mwt 194.52 Volume[CD] 194.45

©1996 JCPDS—International Centre for Diffraction Data All rights reserved

29-0044

Wavelength= 1.54184

AlFe3C0.5

Aluminum Iron Carbide

Rad CuK $\alpha$   $\lambda$  1.5405 Filter d-sp Calculated

Cut off Int Calculated I/Icor

Ref Smith D et al., Penn State University, University Park,  
Pennsylvania, USA, ICDD Grant-in-Aid, (1976)

$2\theta$	Int	$\alpha$	$\beta$	$\gamma$
23 599*	18	1	0	0
33 616*	6	1	1	0
41 479*	100	1	1	1
48 281*	47	2	0	0
54 419*	3	2	1	0
70.673*	18	2	2	0
85 408*	13	3	1	1
90 205*	4	2	2	2
126 084	3	3	3	1
132 269	3	4	2	0

Sys Cubic S G Pm3m (221)

a 3.770 b c A C  
 $\alpha$   $\beta$   $\gamma$  Z 1 mp

Ref Palatinik, Kristallografiya, 9, 163 (1964)

Dx 6.214 Dm SS/FOM F<sub>10</sub>=425(0013, 18)Peak height intensity Perovskite, Ca O3 Ti type PSC cP4 50  
Mwt 200.53. Volume[CD]. 53.58

©1996 JCPDS—International Centre for Diffraction Data All rights reserved

05-0712

Wavelength = 1 54184

 $\alpha$ -Al<sub>2</sub>O<sub>3</sub>

Aluminum Oxide

Corundum

Rad CuKa1  $\lambda$  1 5405 Filter d-sp

Cut off Int I/Icor

Ref: Swanson, Fuyat, Naul Bur Stand (U.S.). Circ 539, 11.  
20 (1953)Sys Rhombohedral S G R $\bar{3}$ c (167)

a 4 758 b c 12 991 A C 2 7303

 $\alpha$   $\beta$   $\gamma$  Z 6 mp

Ref Ibid

Dx 3 989 Dm SS/FOM F<sub>30</sub>=49(0147, 42)Pattern taken at 26 C Sample from Mallinckrodt Chem Works  
PSC. hR10 Deleted by NBS card Set 10. Mwt 101 96  
Volume[CD] 254 70

©1996 JCPDS—International Centre for Diffraction Data All rights reserved

36-0121

Wavelength = 1 54184

 $\theta$ -Al<sub>2</sub>O<sub>3</sub>

Aluminum Oxide

Rad CuKa  $\lambda$  1 5418 Filter d-sp Diffractometer

Cut off Int Diffract I/Icor

Ref Wilson, S., McConnel, J. Solid State Chem., 34, 315 (1980)

Sys Monoclinic SG A2/m (12)

a 5 620(2) b 2 906(1) c. 11 790(5) A 1 9339 C 4 0571

 $\alpha$   $\beta$  103 79(1)  $\gamma$  Z mp

Ref Ibid

Dx Dm SS/FOM. F<sub>21</sub>=8( 051, 52)Made by heating  $\gamma$ -Al<sub>2</sub>O<sub>3</sub> CD Cell a=11 790, b=2 906,  
c=5 620,  $\beta$ =103 79, a/b=4 0571, c/b=1 9339, SG =I2/m(12)  
PSC mC<sup>2</sup>. Mwt 101 96 Volume[CD] 187 00

$2\theta$	Int	$n$	$k$	$l$	$2\theta$	Int	$n$
16 264*	6	1	0	0	62 455*	15	3
19 553*	10	1	0	2	64 088*	30	1
31 501*	60	0	0	4	64 088*	30	0
31 501*	60	1	0	4	65 451*	7	0
32 806*	100	2	0	2	67 479*	75	2
32 806*	100	2	0	0	67 479*	75	2
35 024*	25	1	1	1			
36 712*	60	1	1	1			
38 956*	45	1	0	4			
38 956*	45	0	1	3			
39 890*	35	2	0	4			
39 890*	35	2	0	2			
44 871*	55	2	1	1			
47 663*	35	0	0	6			
47 663*	35	2	1	1			
50 748*	15	0	1	5			
51 453*	6	2	0	6			
51 453*	6	2	0	4			
52 794*	5	3	0	4			
56 795*	8	3	0	2			
56 795*	8	1	1	5			
58 776*	6	3	1	1			
59 950*	25	3	1	3			
61 490*	8	3	0	6			

©1996 JCPDS-International Centre for Diffraction Data All rights reserved

03-0800

Wavelength = 1.54184

 $\alpha$ -Fe2O3

Iron Oxide

Hematite

Rad FeK $\alpha$   $\lambda$  1936 Filter d-sp

Cut off Int Estimation I/Icor

Ref. E. Hahn, G. Ganter, Z. Kristallogr., Kristallgeom., Kristalphys., Kristallchem. 69, 18 (1928)

Sys Rhombohedral SG R $\bar{3}$ c (167)

a 5.055 b c 13.726 A t 27261

 $\alpha$   $\beta$   $\gamma$  Z 2 mp 1360

Ref. Ibid

Dx 1760 Dm 5.260 SS/TOM F<sub>16</sub>=2( .249, 33) $\epsilon\alpha$ : 2.94  $\eta\omega\beta$ : 3.22  $\epsilon\gamma$ : Sign - 2V

Ref. Ibid

PSC hR3 33 Delete similar to 1-1053, Rinn, August 17, 1953

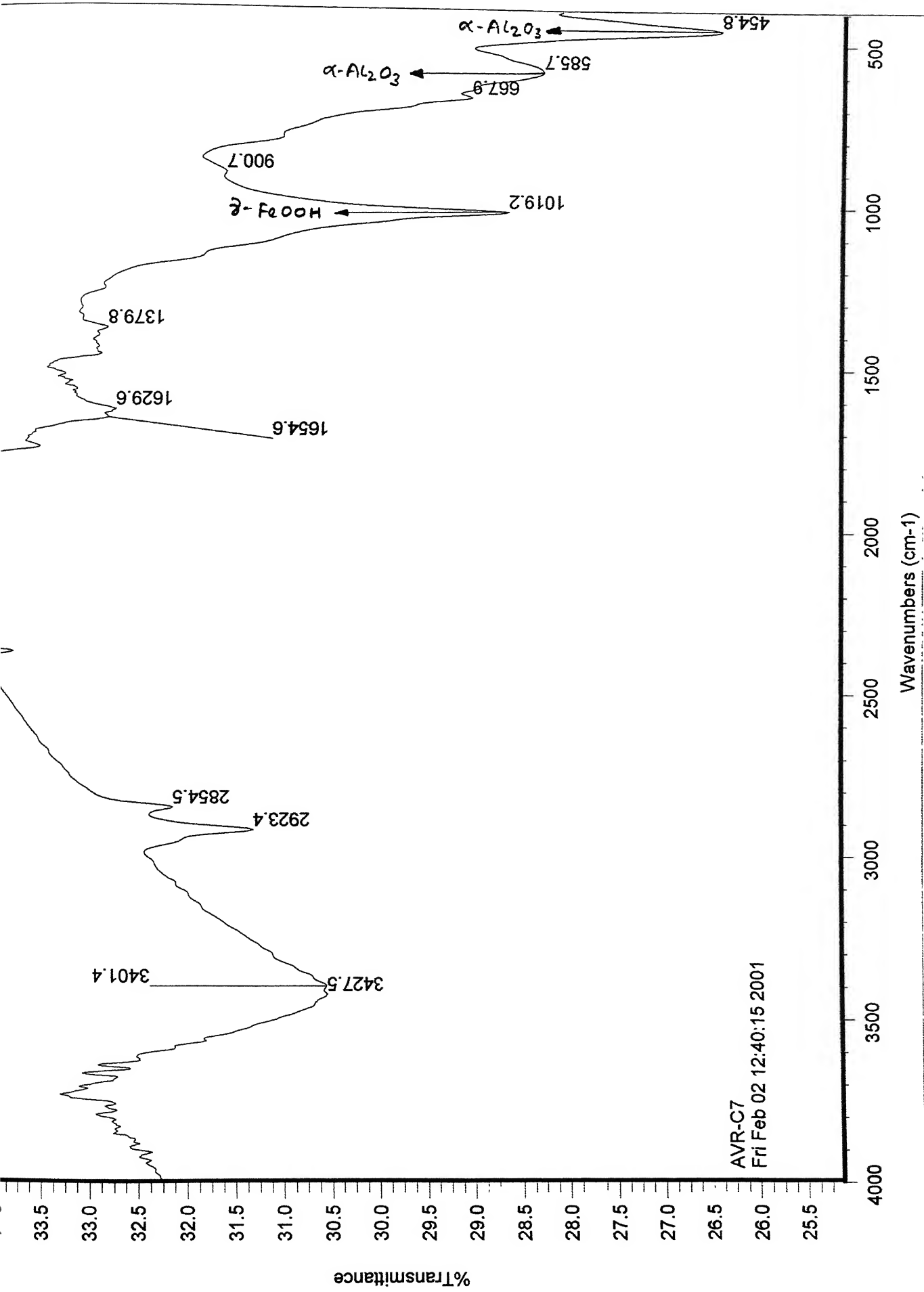
Mwt 159.69 Volume[CD] 301.35

	2 $\theta$	Int	$\frac{c}{\lambda}$	$\frac{h}{\lambda}$	$\frac{l}{\lambda}$
	24.052*	50	3	1	2
	33.055*	100	1	0	4
	35.482*	70	1	1	0
	38.301*	10			
	40.882*	50	1	1	2
	43.510*	10	2	0	2
	49.255*	80	0	2	4
	53.935*	100	.1	.1	6
	57.218*	50	.1	2	2
	62.316*	80	.2	.1	1
	63.745*	80	3	0	0
	65.763*	10			
	69.062*	30			
	71.469*	70			
	74.749*	70			
	77.624*	30	3	0	6
	78.581*	30			
	80.757*	30	3	1	2
	83.301*	30	0	2	10
	85.102*	70	1	3	4
	87.978*	70			
	91.092*	10			
	93.318*	80			
	95.679*	30	4	0	4
	96.915*	10	1	3	7
	101.856	50			
	102.141	50			

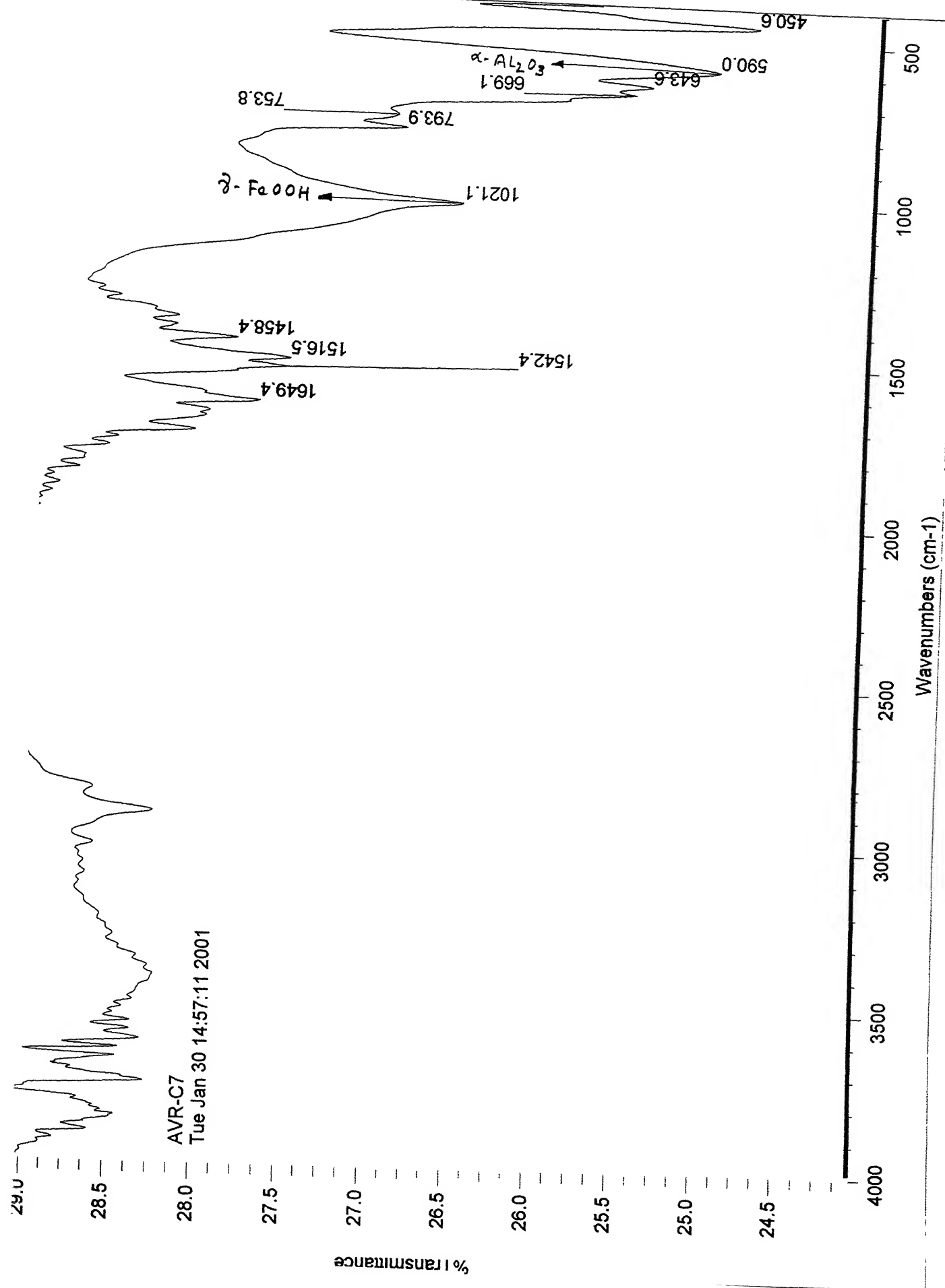
## **Appendix: C**

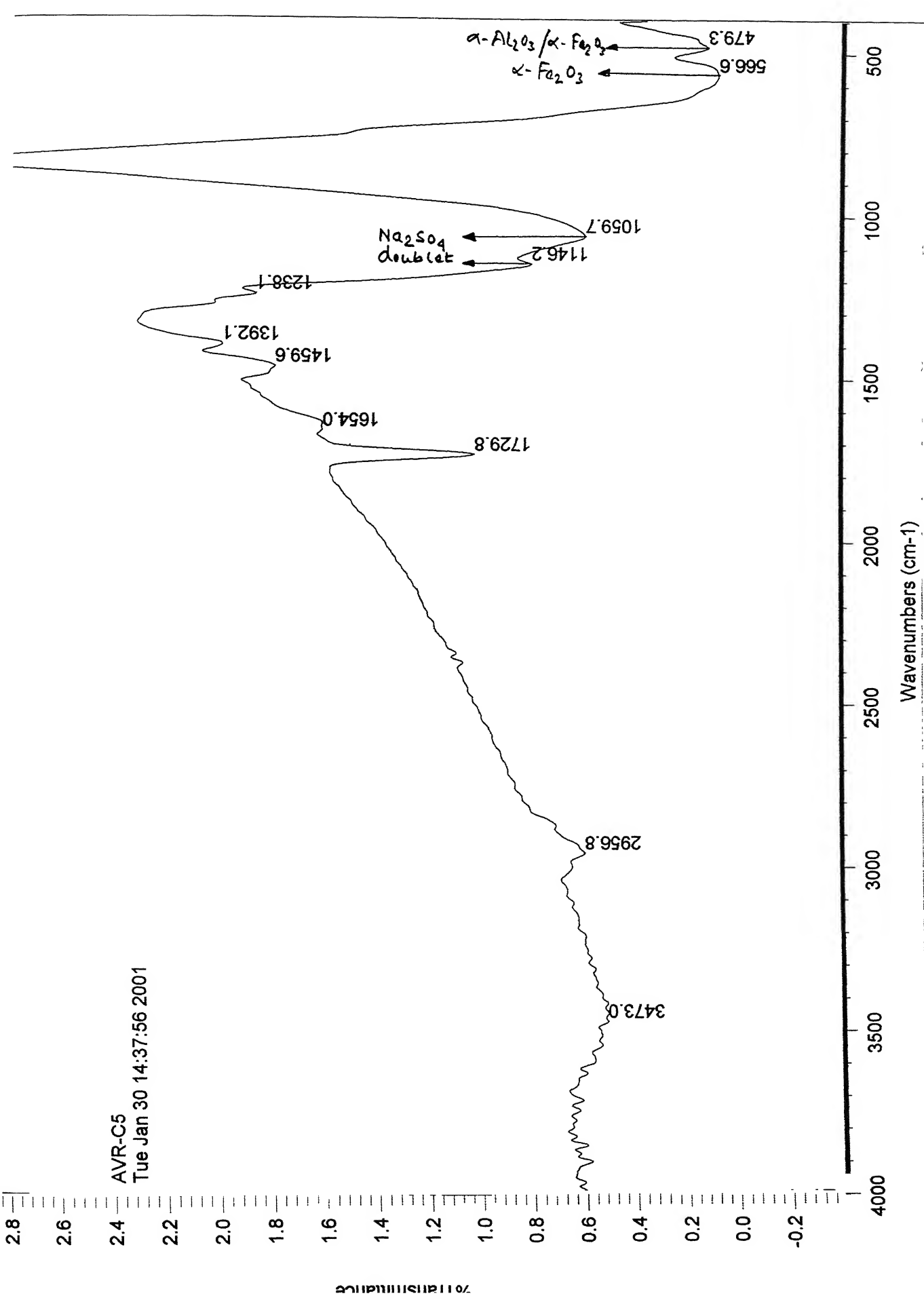
This Appendix gives the FTIR plots for some experiments for both the alloys. The compounds found by FTIR analysis are marked alongside the peaks.

NC/1330K/X.

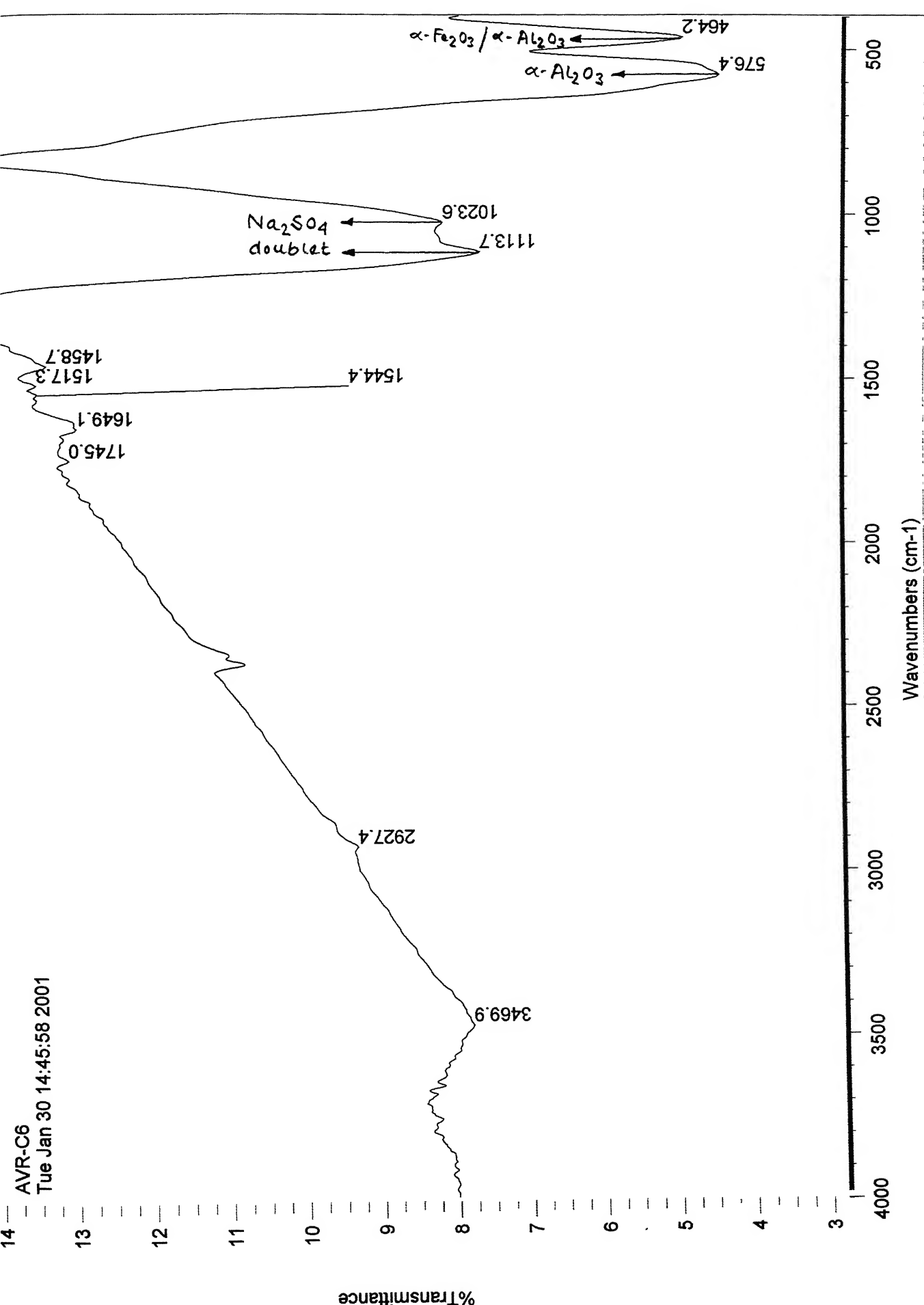


3C/1330k/0x.

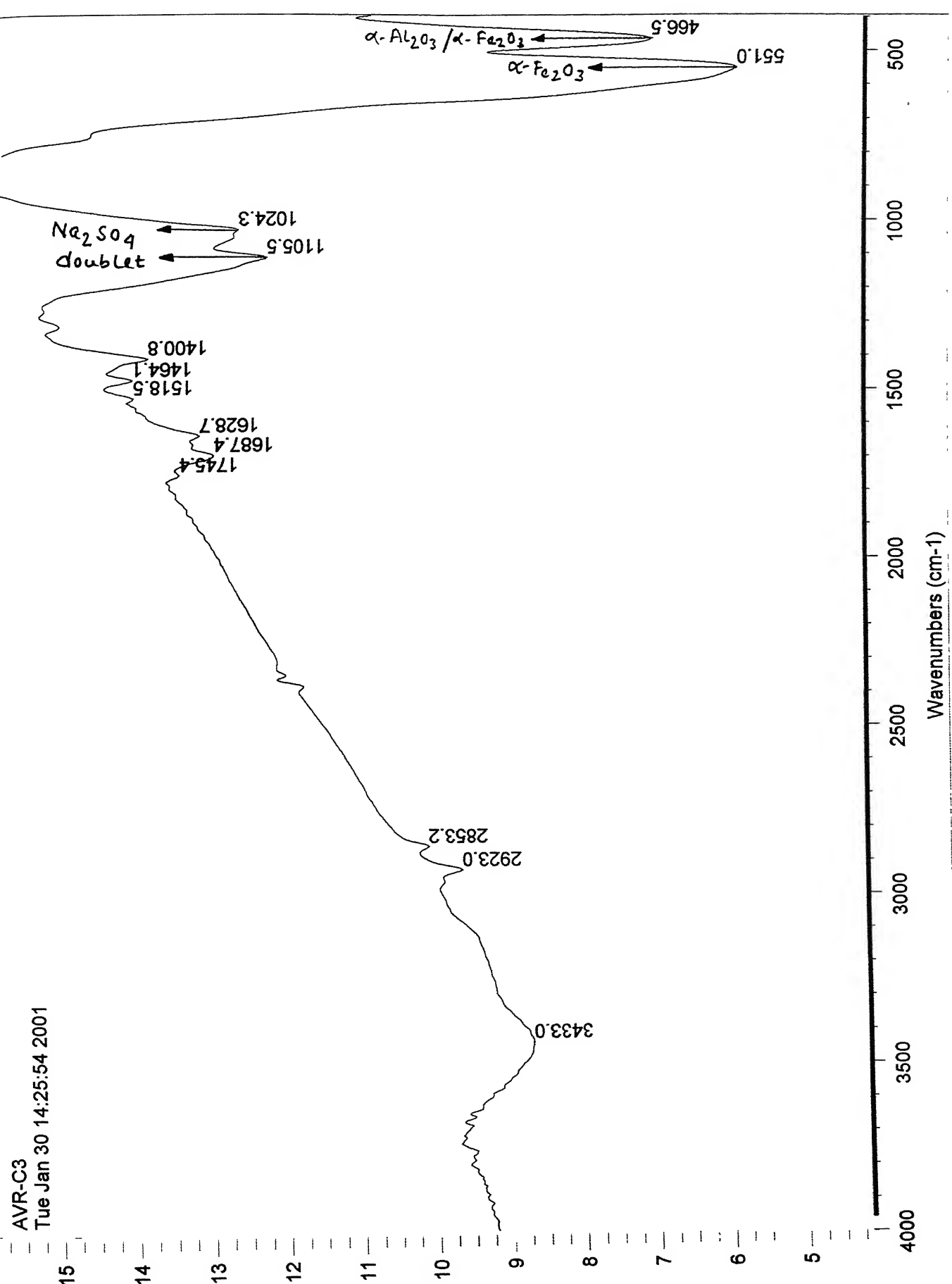




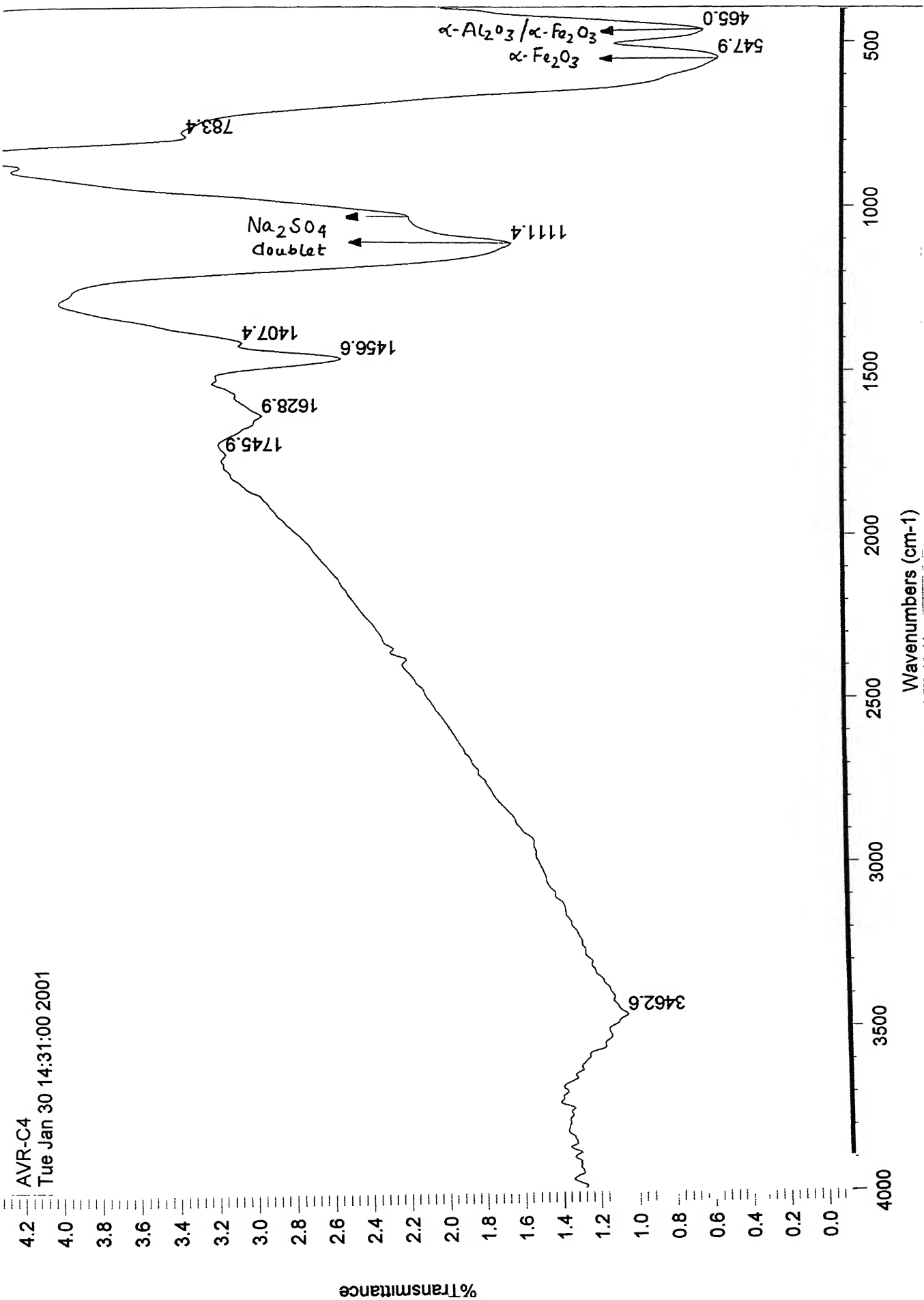
3C/1330K/HC/scales



NC/1225/H C/Scales.



$3C\text{f}2\bar{2}5/\text{HC}/\text{Scales}$



133723

133723

Date Slip

This book is to be returned on  
the date last stamped.

---

---

---

---

---

---

---

---

---

---

---

---

---

---

---

---

---

---

---

---

---



A133723